TECHNISCHE
UNIVERSITÄT
WIEN
Vienna University of Technology

Diplomarbeit

Synthesis and control of nanostructured mixed metal oxide photocatalysts

ausgeführt zum Zwecke der Erlangung des akademischen Grades eines
Diplom-Ingenieurs
eingereicht an der Technischen Universität Wien, Fakultät für Technische Chemie

von

Vivien Madi, BSc

Matr.Nr.:01406096

unter der Anleitung von

Univ.Ass Dr.rer.nat. Alexey Cherevan

Univ.Prof. Mag.rer.nat. Dr.rer.nat. Dominik Eder

Institut für Materialchemie
Forschungsbereich Molekulare Materialchemie
Technische Universität Wien
Getreidemarkt 9, 1060 Wien, Österreich

Wien im September, 2021

Contents

Abbreviations

CB conduction band

CTAB cetyl trimethyl ammonium bromide

DRS UV-vis diffuse reflectance microscopy

FT-IR fourier-transform infrared spectroscopy

HER hydrogen evolution reaction

NPs nanoparticles

OER oxygen evolution reaction

PEC photoelectrochemical

QY quantum yield

UV Ultraviolet

SDBS sodium dodecylbenzenesulfonate

SEM scanning electron microscopy

TEM transmission electron microscopy

VB valence band

XRD X-ray powder diffraction diffraction

Abstract

Die photokatalytische Wasserspaltung ist ein vielversprechender Weg zur Erzeugung von Wasserstoff, welche eine umweltfreundliche Möglichkeit zur Speicherung von Sonnenenergie zur verfügung stellt, und gleichzeitig die Abhängigkeit von konventionellen fossilen Brennstoffen zur Stromerzeugung signifikant reduziert. Vielversprechende, im sichtbaren Licht aktive Photokatalysatoren sind einige Halbleiter, deren optoelektronische und katalytische Eigenschaften geeignet sind, Wasserstoff und Sauerstoff aus Wasser zu erzeugen. In der engeren Auswahl der Materialien spielen die Umweltfreundlichkeit und der Preis des Materials eine wichtige Rolle. $BiVO_4$ hat eine geeignete Bandlücke um Wasser zu oxidieren, ausserdem ist die Herstellung billig und zeiteffizient, das resultierende material ist nicht giftig. $NiFe_2O_4$ ist geeignet aus Wasser, Wasserstoff zu entwickeln. In der vorliegenden Arbeit wurde untersucht, wie sich die Änderungen des pH-Werts der Lösung, der Mikrowellenbestrahlungszeit, der Art des Lösungsmittels und des Tensids während der mikrowellenunterstützten Synthese von $BiVO_4$ auf die Morphologie, die Phasenreinheit, die Bandlücke und die Leistung bei der Sauerstoffentwicklungsreaktion auswirken. Des Weiteren wurde die mikrowellenunterstützte Synthese, die bereits für $NiFe_2O_4$ berichtet wurde, optimiert. Bei der pH abhängigen Synthese wurde erwartet, dass monoklines $BiVO_4$ ensteht, welches eine oktahedrische Morphologie aufweist. Dies war nur bei dem pH Bereich 0.08 bis 0.88 gegeben. Die Zeit abhängige Synthese wurde durchgeführt um den Bildungsmechanismus des $BiVO_4$ zu verfolgen und zu verstehen. Bereits eine Mikrowellenbestrahlung von 2 minuten während der Synthese führte zu einphasigem monoklinen $BiVO_4$ mit einer gut definierten oktaedrischen Struktur, die eine ausgezeichnete Sauerstoffentwicklungsaktivität aufwies. Zusätzlich waren 10 sekunden von mikrowellenbestrahlung genug um polyhedron förmige partikel zu synthetisieren. Die Lösungsmittelabhängige synthese wurde durchgeführt um den Kristallfacettenwachstum zu kontrollieren, allerdings resultierten die so erhaltenen halbleiter in der scheelite tetragonalen Phase. Bei der allgemeinen Untersuchung der Sauerstoffentwicklungsaktivität wurde festgestellt, dass die monokline Phase im Vergleich zum Komposit aus monoklinem und tetragonalem $BiVO_4$ und im Vergleich zur tetragonalen Phase eine viel bessere Sauerstoffentwicklungsaktivität aufweist. Gegenüber anderen Morphologien der monoklinen Phase wies die oktaedrische Morphologie bessere Sauerstoffentwicklungsaktivitäten auf, wobei die photokatalytische aktivität linear mit der exposition der 010 facetten anstieg. Bei der Ermittlung der Sauerstoffentwicklungsaktivität als Funktion des Bandlückenwertes und der Kristallitgröße wurde festgestellt, dass die Sauerstoffentwicklungsaktivität mit zunehmender Kristallitgröße und Bandlücke ansteigt.

Photocatalytic water splitting is a promising way to generate hydrogen, which provides an environmentally friendly way to store solar energy while significantly reducing dependence on conventional fossil fuels for power generation. Promising visible-light active photocatalysts are semiconductors whose optoelectronic and catalytic properties are suitable for generating hydrogen and oxygen from water. In the shortlist of materials, the environmental friendliness and the price of the material play an important role. $BiVO_4$ has a suitable band gap to oxidize water. In addition, the production is cheap and time-efficient, the resulting material is non-toxic. $NiFe_2O_4$ is suitable to evolve hydrogen from water. In the present work, it was investigated, how the changes of the solution pH, microwave irradiation time, type of solvent and surfactant have an effect during microwave assisted synthesis of $BiVO_4$ on the morphology, phase purity, band gap and performance in oxygen evolution reaction (OER) activity. Furthermore, the microwave assisted synthesis, which was reported earlier for $NiFe_2O_4$ was optimized. In the pH-dependent synthesis, it was expected that monoclinic $BiVO_4$ would be formed, which has an octahedral morphology. This was only the case for the pH range 0.08 to 0.88. Time-dependent synthesis was performed to follow and understand the formation mechanism of $BiVO_4$. Microwave irradiation for as little as 2 min during the synthesis resulted in pure phase monoclinic $BiVO_4$ with a well-defined octahedral structure that exhibited excellent oxygen evolution activity. In addition, 10 seconds of microwave irradiation was enough to synthesize polyhedron shaped particles. The solvent-dependent synthesis was performed to control crystal facet growth, however, the products obtained resulted in the scheelite tetragonal phase.

In the general investigation of oxygen evolution activity, the monoclinic phase was found to have much better oxygen evolution activity compared to the composite of monoclinic and tetragonal $BiVO_4$ and compared to the tetragonal phase. Compared to other morphologies of the monoclinic phase, the octahedral morphology exhibited better oxygen evolution activities, with the photocatalytic activity increasing linearly with the exposure of the 010 facets. When investigating the oxygen evolution activity as a function of the band gap value and crystallite size, the oxygen evolution activity was found to increase with increasing crystallite size and band gap.

Acknowledgements

First and foremost, i would like to thank Prof. Dominik Eder for the opportunity of conducting my master internship in his research group. The Eder research group provided a welcoming and inspiring atmosphere during my time there. I would also like to express my gratitude to my supervisor, Dr. Alexey Cherevan, who introduced me to his intriguing field of research and guided me through the months until this thesis finally took shape. In this time, he patiently explained everything and taught me plenty of new skills. I am thankful to Prof. Peter Blaha and Leila Kalantari MSc for the introduction to WIEN2k and for their useful tips and patience. Special thanks to my friends Dóra, Peter and Stefan for the countless advises, abundant kindness and of course for encouraging me to pursue science during my Chemistry and Materials Technology Master. Without them I would most certainly not be as much successful in my studies as I was in the past.

1 Introduction

1.1 Current energy problem and the utilization of sunlight

At the present, global energy consumption rate is approaching 14 TW, with the US and the enlarged EU each contributing about 25% to the consumption.[1] According to predictions based on the energy consumption rate it is predicted, that the energy usage will increase swiftly in upcoming decades due to future industrialisation of underdeveloped countries and the rising energy-request from developing countries combined with increasing world population.[2,3] The majority of our current energy supply comes from fossil fuels, which are limited resources and non-renewable in nature. In addition, the use of fossil fuels is questionable because large amounts of greenhouse gases and organic pollutants are released into the atmosphere while combustion.[4] As a result of the reduction of presently available energy resources and the aggravation of the environment, solar energy is receiving elevated attention as promising alternative to fossil-based energy sources.[5] Solar energy is a natural resource, which is renewable, inexhaustible and clean. The energy that could be acquired by irradiating the earth's surface with one hour of sunlight exceeds the annual global consumption of mankind.[2,5] However, to create a widespread and efficient primary energy source for humanity, solar energy must be collected, converted, and accumulated in a cost-effective and environmentally friendly way.[6]

Due to its high energy-density and transportability, hydrogen has been identified as a promising way to store untapped solar energy via chemical bonding, hence solve the energy and environmental crisis by meeting the demand for clean energy.[7–9] Hydrogen can be used to produce mechanical energy in engines or electrical energy in fuel cells by reacting it with oxygen. Since water occurs as the only by-product it can be considered as green-energy.[5,10–12] During the catalytic water splitting of pure water to H_2 and O_2, the photon energy is converted into chemical energy and as a result the Gibbs free energy increases greatly (ΔG°=238 $\frac{kJ}{mol}$).[11,13–15]

$$H_2O + h\nu \rightarrow H_2 + \frac{1}{2}O_2 \tag{1}$$

This process is inspired by natural photosynthesis. Thus water splitting with the utilization of man-made materials can be considered as artificial photosynthesis and can be used for the controlled solar-to-chemical energy-conversion.[13,16] The research of artificial photosynthesis systems was introduced by Fujishima and Honda in 1972, as they were the first to make the discovery of generating hydrogen in a photoelectrochemical (PEC) process from an aqueous solution using a TiO_2 photoanode and Pt photocathode.[17] Since their discovery, numerous research groups have exhaustively studied photocatalytic and PEC water splitting.[9,13,18–20] From the perspective of large-scale hydrogen production, heterogeneous photocatalyst systems with the utilization of particulate semiconductors have a broader range of applications compared to PEC cells, because of their simplicity and lower cost.[13,14,19] In general, the water-splitting process consist mainly of three part-reactions: light-harvesting, charge generation combined with charge separation and the final catalytic reaction process, whereat the balance of thermodynamics and kinetics of these processes determines the overall efficiency.[9,16] The key for effective photocatalytic water splitting is the development of photocatalysts capable of efficiently absorbing sunlight in order to split water.[9,21] Numerous photocatalytic systems based on metal oxides have been reported to be active for overall water splitting. However, due to the large band gap of semiconductor materials, most of them require ultraviolet (UV) light ($<$400 nm), and therefore cannot take advantage of visible light, which accounts for 45% of the light incident on the Earth's surface.[8,9,22,23] Hence, it is essential to use visible light efficiently to realize H_2 production on a large scale by photocatalytic water splitting.[13,24]

The structural, electronic and optical properties of the material are pivotal for succesful water splitting. It is necessary to have a suitable band gap and band position with adequate driving potential. Furthermore, high crystallinity has a favorable influence on the catalytic activity, since the defect concentration decreases as a result of the increase in crystallinity. Small particles promote a reduction in the recombination probability, since the photogenerated charge carriers can easily migrate to the reaction sites on the surface and can realize surface catalytic proton reduction and water oxidation.[11] The most important kinetic constraint for water splitting is the one involving a multi-electron process, namely the water oxidation reaction.[25,26] In the following chapters, the theoretical background of photocatalytic water splitting as well as possibilities for optimising the catalytic activity are presented. Acquiring this knowledge and putting it into practice is the key to preparing a photocatalyst with high catalytic activity.

1.2 Fundamentals of photocatalytic water splitting

When light is irradiated with an energy equivalent, which is equal to or greater than the band gap of the semiconductor photocatalysts, the electrons in the valence band are excited into the conduction band, with the purpose of forming free charge carriers: holes (h^+) and electrons (e^-).[27] The photoelectrons and holes oxidize (1) and reduce (2) water, respectively, to produce the 2:1 mixture of H_2 and O_2 (3) by the following reactions:

$$H_2O + 2h^+ \rightarrow 2H^+ + \frac{1}{2}O_2 \tag{2}$$

$$2H^+ + 2e^- \rightarrow H_2 \tag{3}$$

$$H_2O \rightarrow H_2 + \frac{1}{2}O_2 \tag{4}$$

The overall reaction involves four-electron transfer (per O_2 molecule) and is usually promoted by metal or metal oxide co-catalysts deposited on the semiconductor surfaces.[28] In order to realize overall water splitting, the bottom of the conduction band must be positioned below the reduction potential of H^+, while the top of the valence band must be located more positively than the oxidation potential of H_2O.[27] The process of water splitting into H_2 and O_2 are illustrated in Figure 1, and can be divided into three basic steps: 1) light harvesting ad photoexcitation of charge carriers; 2) charge carrier separation and diffusion; and 3) oxidation and reduction reaction on the catalyst surface.[29]

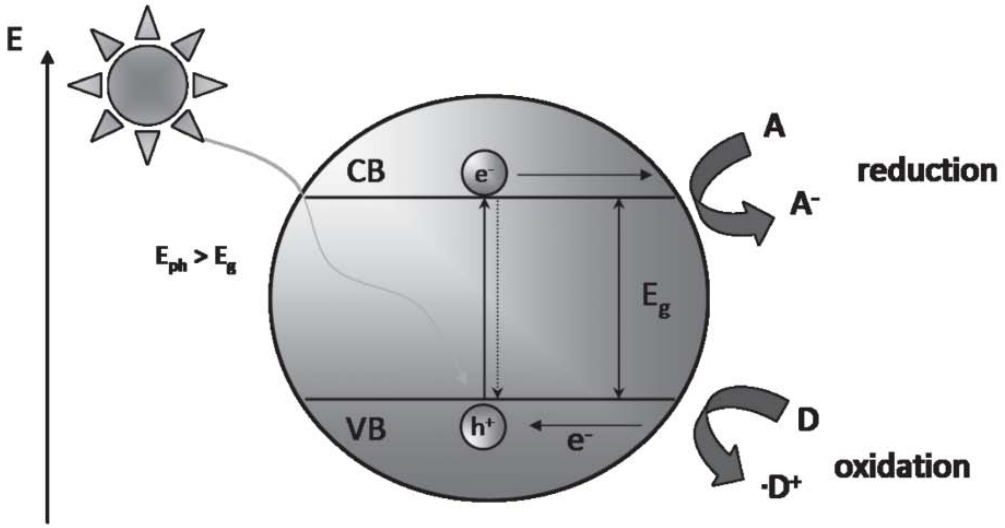

Figure 1: Process of charge carrier generation upon light irradiation of a semiconductor particle; E_{ph}: energy of irradiated photon, E_g: difference of the energetic positions of the conduction band and valence band, A: electron acceptor, D: electron donor.[29]

During the water splitting process, electrons and holes can also recombine with each other without participating in any chemical reactions. The recombination processes have a significant impact on the efficiency of the photon-to-H_2 energy conversion. Efficient charge separation and fast charge carrier transport, avoiding any bulk/surface charge recombination and the backward reaction of H_2 and O_2

to produce water, are thus fundamentally important for photocatalytic H_2 generation through water splitting.[4] Tailoring of semiconductor properties by fabricating designed nanostructures is the key to the performance improvement of various optoelectronic, photoelectrochemical and photocatalytic devices.[30] Some semiconductor properties such as specific surface area, particle size, crystallinity, crystalline phase, and morphology have been shown to have a significant effect on photocatalytic activity.[9] A reliable, reproducible particulate photocatalyst functional under visible light must satisfy several principal requirements. These include a suitable band gap for harvesting light, nanostructured materials with high crystallinity for facile transport and separation of charge carriers, and proper positions of conduction band (CB) and valence band (VB) for redox reactions.[5,31] Overall water splitting using particulate photocatalysts has been considered as a low-cost technology with the potential to enable large-scale solar hydrogen production, given the ease of synthesis of the corresponding photocatalysts as well as the simple reactor designs.[32–34]

1.2.1 Photocatalytic activity

The goal of a photocatalytic hydrogen generation system is to decompose water directly into hydrogen and oxygen under irradiation with visible light.[35] In this process, a semiconductor with suitable band gap positions can absorb photon energy and evolve hydrogen and oxygen simultaneously. In order to perform photocatalytic water splitting, a Gibbs free energy of 237 $kJmol^{-1}$ is needed. In addition, semiconductors can not produce hydrogen and oxygen in a stoichiometric ratio due to the accumulation of charge carriers on the surface of the photocatalyst.[35] Thus, overall water splitting under visible light illumination has become one of the greatest challenges for researchers in this field.[9] In order to report the photocatalytic activity, few reasonable measurement values are introduced, which provides comparability between different research groups. Theese are: photocatalytic activity, quantum yield and the apparent quantum yield. The light source (Xe or Hg lamps), light intensity, different irradiation directions (top, inside or side), the reaction media and the amount of photocatalyst in the reaction cell are all factors that determine the photocatalytic activity. Usually the activity is specified by the amount of evolved gas in a specific period of time in $\mu mol\,h^{-1}$ or $\mu mol\,h^{-1}\,g^{-1}$.[36,37]

The quantum yield (QY) is another approach to report the photocatalytic activity of a semiconductor. The QY is independent of the factors mentioned above, and is defined in equation 5.

$$\mathrm{QY}\,(\%) = \frac{\text{number of reacted electrons}}{\text{number of absorbed photons}} \times 100 \tag{5}$$

Because the measurement of absorbed photons is really challenging, the apparent quantum yield (APY) needs to be used in order to accurately specify the photocatalytic activity. The AQY is defined in equation 6.[38]

$$\mathrm{AQY}\,(\%) = \frac{2 \times \text{number of evolved } H_2}{\text{number of incident photons}} \times 100 = \frac{4 \times \text{number of evolved } O_2}{\text{number of incident photons}} \times 100 \tag{6}$$

Solar energy conversion efficiency is a method to calculate solar cell efficiency. It can also be used to report the photocatalytic activity of a semiconductor.

$$\text{Solar energy conversion efficiency}\,(\%) = \frac{2 \times \text{output energy of } H_2 \text{ evolved}}{\text{energy of incident solar light}} \times 100 \tag{7}$$

In this work, all photocatalysis have been investigated under identical illumination conditions. Considering this, comparison of their absolute activities (H_2/O_2 evolution rates) is sufficient for an adequate benchmarking. Calculation of QYs would however be of importance if a comparison to other works across the literature is of interest.

1.3 Strategies for improving the photocatalytic activity

1.3.1 Cocatalyst and sacrificial reagent system

As discussed earlier, a certain type of semiconductor with suitable band edge positions is required for water splitting. However, the use of semiconductors offers the disadvantage of low solar energy conversion values. For the industrial application of water splitting by sunlight, the efficiency of photocatalysts should be significantly improved.[22]

A cocatalyst or a sacrificial reagent system is commonly used in order to realise and improve the overall water splitting reaction. A cocatalyst is a compound that is deposited onto the photocatalyst semiconductor surface to improve their activity. Cocatalysts can be used in photocatalytic water splitting to enhance either the water oxidation or water reduction reactions. The co-catalysts for water reduction are usually small metal nanoparticles (NPs), which can enhance the charge separation of the free charge carriers in a photocatalyst or photoelectrochemical cell by forming a Schottky junction with the semiconductor.[39,40] The contact between semiconductor and cocatalyst generates an electric field when the work function of the metal matches the conduction band edge of the semiconductor, and thus excited electrons and holes can be separated more easily. Furthermore, the cocatalyst offers additional active sites for hydrogen reduction. The reason for this is its relatively low overpotential for water reduction. The cocatalyst's concentration on the semiconductor surface should be optimized by finding a compromise between the number of active sites and the absorptivity of the photocatalyst to achieve the maximum activity for water splitting under visible light.[41,42] In the past, various types of co-catalysts including transition metals, metal oxides, and noble metals have been used for each water splitting half-reaction. The most commonly used co-catalysts for hydrogen evolution are Pt, Rh, Au, NiO and RuO_2.[43–45]

Some semiconductors can perform one of the half-reactions of water splitting, such as water reduction or oxidation, in the presence of suitable sacrificial reagents (electron donors or acceptors). Usually the sacrificial reagents react with the charge carrier formed during photoabsorption, while the other charge carrier reacts with water, thus enable the water splitting reaction. Electron donors, which consume excited holes on the surface of the semiconductor, are used for the water reduction half reaction and electron acceptors (electron scavengers) are usually needed for water oxidation.[9] The mostly used electron donors are methanol, ethanol, triethanolamine (TEA) and an aqueous solution of Na_2S–Na_2SO_3, whereas metal cations such as Ag^+ and Fe^{3+} are usually utilized as electron acceptors.[8,35,46,47] In the case of using methanol as the electron donor, hydrogen is also produced from water as a result of methanol conversion, as shown in equation 4.[48,49]

$$CH_3OH + H_2O \rightarrow CO_2 + H_2 \tag{8}$$

In addition some semiconductors are capable of decomposing water into H_2 eith the help of biomass-derived sacrificial reagents.[50,51]

1.3.2 Band gap engineering

The physical and chemical properties of a semiconductor play an essential role in the absorption of light and in the determination of redox potentials. Among others, the energy band configuration is one of the most important factors determining the photocatalytic activity. Energy band engineering represents an effective approach for the research and development of visible light active photocatalysts, in order to improve solar energy utilization.[52]

1.3.3 Doping with metals and non-metals

In most oxide semiconductors, the CB minima are slightly negative than reduction potential of H_2O (versus NHE), while the VB maxima are significantly positive with respect to the oxidization of H_2O (versus NHE). Doping is the introduction of a foreign element into the crystal structure of a metal oxide. Doping generates an energy level above the valence band (donor level) or an energy level below the conduction band (acceptor level) of a semiconductor.[11] In the past decades, three approaches have been found to be most effective in adjusting the level of VB, namely doping with 3d-transition elements, cations with d^{10} or $d^{10}s^2$ configurations, and non-metal elements.[52] Theoretical investigations based on ab initio band structure calculations have shown, that as the order number of the dopants increases, the localized 3d levels of the photocatalyst shifts to lower energies.[53] In some cases new band gap levels can be inserted into the original band gap if the 3d states mix with the CB or the VB.[54] However, doping with 3d-transition elements can have two critical disadvantages, restricting its applicability. Firstly, foreign elements with different chemical valence introduce considerable bulk defects and thus increase the recombination probability of photogenerated electron-hole pairs. Secondly, the localized d-states in the electronic structure suppress the migration of carriers.[52] Occupied d or s-states can be introduced into the VB of multi-metal oxides, such as Ag^+, Bi^{3+} and Pb^{2+}, by doping them with elements with d^{10} or $d^{10}s^2$ configuration. Hybridization of d/s states with O 2p states contributes to an up-shift of the top of the VB and therefore to a narrowing of the band gap.[55–60] Although the modulation of the VB is generally of high priority, the level of the CB is closely related to the capability of reducing H_2O and O_2 and should therefore also receive attention. The energy level of the CB plays a significant role in determining whether the photo-generated electrons in the CB reduce H^+ to produce H_2. It should also be noted that the level of CB also determines whether these reactions can take place and how efficient these processes are.[52] The substitution of alkali metal or alkaline earth metal elements by elements lower in the periodic table is known to be effective in lowering the minimum of the CB.[61–63]

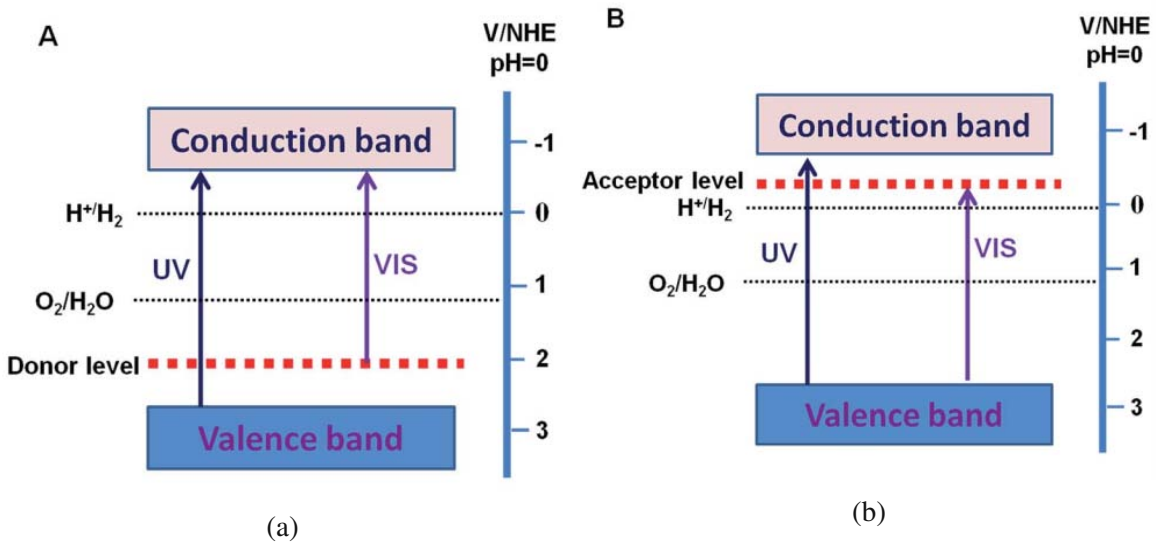

(a) (b)

Figure 2: Donor level (A) and acceptor level (B) induced by metal ion doping[27]

Often, the introduction of metals into the host crystal structure reduces the overall photocatalytic efficiency because recombination centers can be generated as a consequence. Therefore, it has been

observed in many cases that doping with suitable nonmetals is more effective than with metals.[11] In order to raise the VB maximum different anions on the O sites can be introduced. For example, TiO_2 has been doped with N, C, B, and S and the photocatalytic properties of these materials have been extensively investigated.[64–67] For some simple oxides and multi-metal oxides, the crystal structure is destroyed when the proportion of substituted anions exceeds its tolerance; transformation to oxynitrides, oxysulfides, or oxyhalides then takes place, and also, since a new compound with a new crystal structure is formed, this strategy avoids introduction of detrimental defects, hence induce a significant increase in visible light absorption.[68–71]

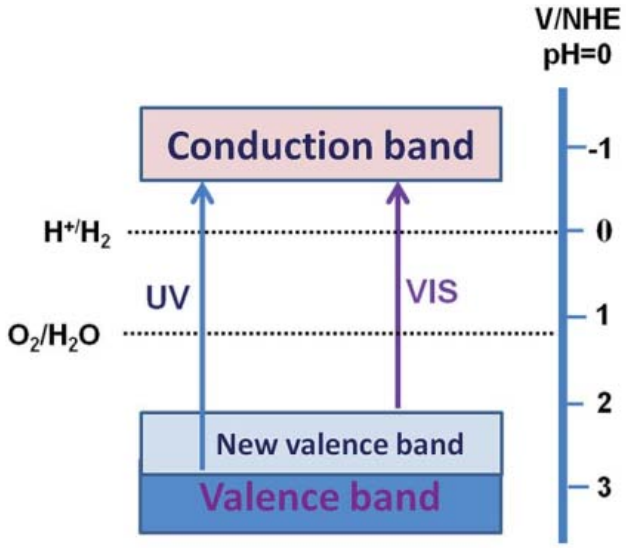

Figure 3: New valance band formation by doping of non-metal ions[27]

1.3.4 Single phase materials and solid solutions

Doping creates defects on materials, which then serve as recombination centers for the free charge carriers generated during photoexcitation. Thus, single-phase oxide materials are more stable and have become increasingly important in recent times.[27,72–76]

Another approach in order to obtain semiconductors with proper band gap position for the water splitting reaction is the fabrication of solid solutions. In the case of a solid solution based material, two different types of photocatalysts with similar crystal structure are mixed together and are chemically reacted with each other. The newly formed material does not exhibit the individual properties of the starting materials. The developed material shows improved photocatalytic property compared to the starting materials.[27]

1.3.5 Composite photocatalysts

Presently, successful photocatalytic systems for the decomposition of H_2O into H_2 and O_2 are based on one of two approaches. One method involves the fabrication of heterojunction photocatalyst out of at least two semiconductors.[29] An alternative approach is the coupling of two individual photocatalysts with an electron transfer mediator to obtain two-step excitation, known as a Z-scheme process.[13]

1.3.6 Heterojunction

By carefully tuning the band alignment and interfacial contact, semiconductors with a heterojunction structure can promote the efficiency of total water splitting by generating long-lived electron-hole pairs. The principle of heterostructures is based on photosystem II, and thus it can be considered as artificial photosynthesis.[28,77,78] When a suitable band alignment is formed, electrons flow from the semiconductor with the higher Fermi energy level (semiconductor A) to the semiconductor with the lower Fermi energy level (semiconductor B), resulting in an electron depletion region in semiconductor A and an electron accumulation region in semiconductor B. Thus, a built-in electric field is created at the interfaces with a potential difference between the two materials.[79] Depending on the band gap and relative energy level of the CB and VB, the semiconductor heterojunctions can be divided into three categories, illustrated in Figure 4.

In a type I heterojunction, the level of CB of semiconductor B is higher than that of semiconductor A, and the level of VB of material B is lower than that of material A, thus holes and electrons are transferred and accumulate on semiconductor A. In a type II heterojunction, photoexcited electrons are transferred from semiconductor B to semiconductor A because the CB position of semiconductor B is lower. Holes can migrate in the opposite direction from the more positive VB from A to B, resulting in all-around efficient charge separation and improved photocatalytic activity. The CB and VB arrangement of the heterojunction of type III is similar with type II, except for the much more significant difference in the energy differences, resulting in a higher driving force for charge transfer.[78]

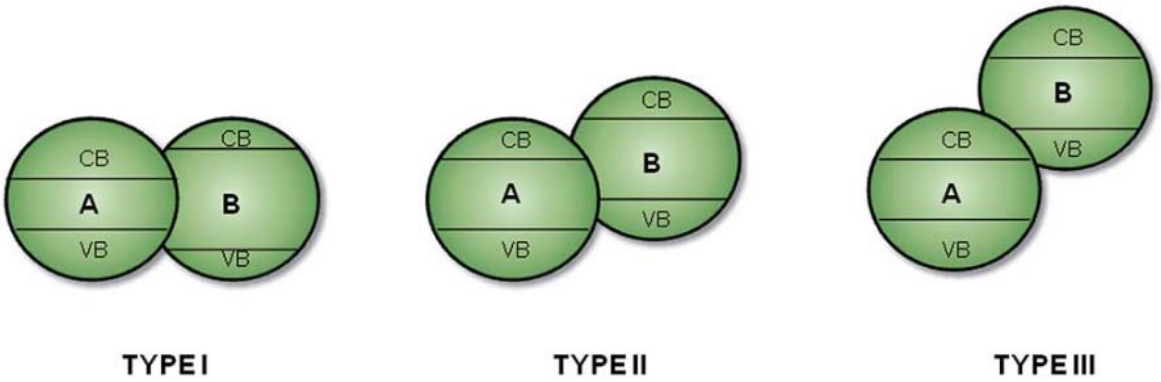

Figure 4: Band alignment in Type I, II, and III heterojunctions

Furthermore heterojunction photocatalysts can be classified based on material morphology, such as partial contact photocatalysts and core-shell photocatalysts.[80] An important factor to consider in the heterojunction design for efficient photocatalytic activity is the band edge alignment. In general, this is a common phenomenon affecting all heterojunctions and it has been extensively studied in various electronic and optoelectronic semiconductor devices.[81] The band alignment and band bending in nanosized heterojunction semiconductors can be strongly dependent on the particle sizes and their arrangement on each other.[82] Depending on the morphology of two semiconductors, partial contact photocatalysts can have point contact where one of the photocatalysts is a nanoparticle, line contact for nanowire or nanoribbon/nanosheet catalysts, and face contact when both photocatalysts are two dimensional.[83]

1.3.7 Z-scheme system

The function of the Z-scheme system is to solubilize charge carriers with two different electron mediators, which should return to their original chemical state after participation. This system is also called electron mediator system or dual photocatalyst system.[84] This procedure for overall water splitting is entirely different to the two previous methods. For the electron mediator system, two different photocatalysts are needed, one semiconductor that enables the half-reaction to H_2 evolution by providing photoexcited electrons, and another that provides photogenerated holes to participate in the half-reaction of water oxidation. The two semiconductors can be excited simultaneously and one half of the charge carrier recombines by bringing the electron mediators to their original states. The most used electron mediators are Fe^{3+}/Fe^{2+}, IO^{3-}/I^- and Ce^{4+}/Ce^{3+}.[9] Different approaches and applications how to mimic natural photosynthesis with electron mediator systems are discussed in some reviews.[84,85] The Z-scheme system is more complicated and therefore it has some disadvantages compared to the one-step system. For the electron mediator system, several photons are needed to produce the same amount of hydrogen, since half of the free charge carriers are used to bring the excited mediator back to its ground state for further reactions.[86]

1.4 Choice of photocatalyst

1.4.1 $BiVO_4$

Bismuth vanadate ($BiVO_4$) is now considered as one of the most promising material for the water-splitting process operating in the visible light range, because of its high O_2 evolution activity, narrow band gap, high stability and low toxicity.[25,87–90] There are three polymorphs of $BiVO_4$: monoclinic scheelite (m$BiVO_4$), tetragonal scheelite (t-s $BiVO_4$) and tetragonal zircon structures (t-z $BiVO_4$).[91] Of these three structures, monoclinic form has found to be the most photocatalytically active.[92] The sheelite and also the zircon structures consists of isolated $[VO_4]^{3-}$ tetrahedra connected by $[BiO_8]^{5-}$ antiprisms, but the way how they are connected is different. Das et al. has demonstrated the phase transition between the zircon and sheelite structure based on a first order reconstruction with a bond exchange mechanism.[89,93] With the monoclinic phase as a starting point, three changes were observed to reach the zircon phase: (1) a rotation of the $[VO_4]^{3-}$ tetrahedral units; (2) an expansion along the a and b-axes of the monoclinic cell; (3) a strong compression along the c-axis.[89] The crystal structure of the monoclinic and tetragonal phase is shown in figure 5.

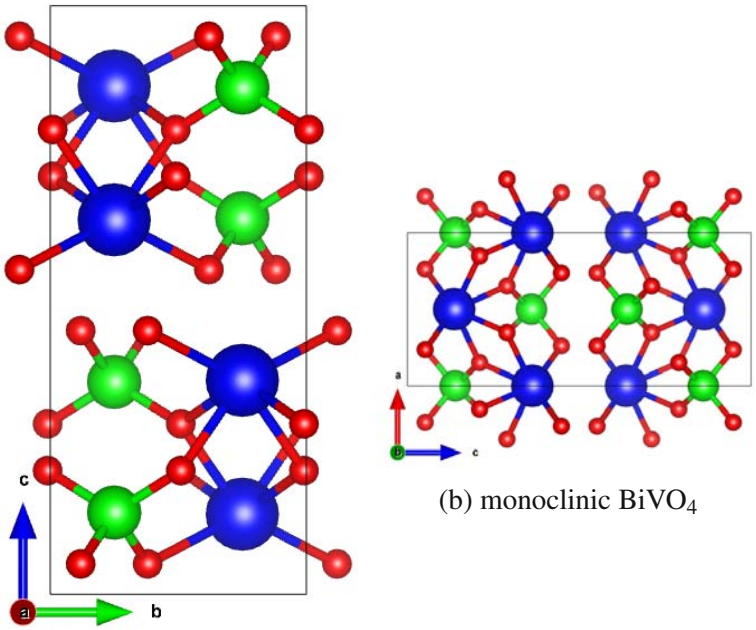

(a) monoclinic $BiVO_4$

(b) monoclinic $BiVO_4$

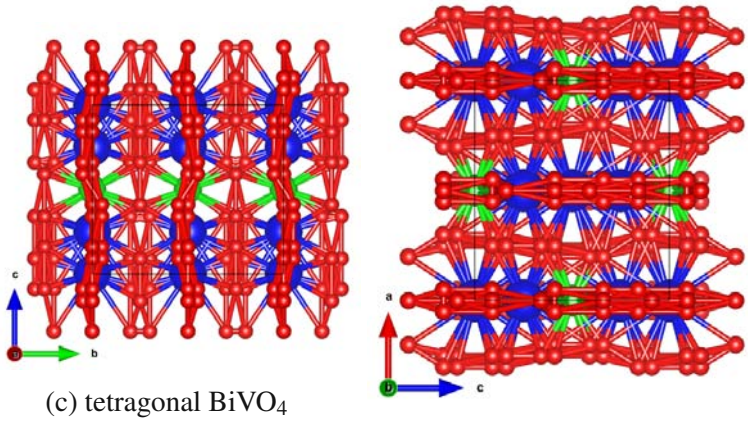

(c) tetragonal $BiVO_4$

(d) tetragonal $BiVO_4$

Figure 5: VESTA visualisation of monoclinc and tetragonal $BiVO_4$

The CB and VB positions of the $mBiVO_4$ and $tBiVO_4$ are similar, hence the thermodynamic limitations for the catalytic structures are similar as well. However $mBiVO_4$ shows higher photocatalytic performance than $tBiVO_4$, because the Bi–O polyhedron in $mBiVO_4$ are more distorted by a $6s^2$ lone pair of Bi^{3+} than those in $tBiVO_4$.[59,94] It is described that this structural distortion can enhance the lone–pair impact of the Bi 6s states, while the VO_4 tetrahedron distortion induces an internal electric field, both beneficial for the electron–hole separation process and giving its anisotropic optical properties.[95] The magnitude of the dipole moment on the surface correlates with the oxygen evolution activity, which is dependent on the geometrical structure of $BiVO_4$. Thus, it was found that the distortion of the VO_4^{3-} tetrahedron in the $mBiVO_4$ compared to the regular tetrahedron in the $tBiVO_4$ has a significant effect on the dipole moment, leading to higher oxygen evolution.[96,97]

Electronic structure predictions based on density functional theory (DFT) calculations shows that the edge of the VB of $mBiVO_4$ is chiefly consisted of O 2p and Bi 6s orbitals, while the CB edge is majorly dominated by V 3d orbitals.[95] Hence it can be assumed, that the visible light induced excit-

ation of electrons happens from O 2p orbitals to the V 3d orbitals, leaving holes in the O 2p orbitals in the case of tetragonal $BiVO_4$. However, for monoclinic $BiVO_4$ the excitation happens from a hybrid orbital, consisiting of O 2p and Bi 6s orbitals on the top of the valence band to the vanadium 3d conduction band.[97] Payne et al. described a model, which describes the electronic assymetry around Bi arising predominantly from interaction between the Bi 6p state, in the middle of the valence band and antibonding Bi 6s and O 2p states at the valence band maximum, which creates a Bi lone pair.[98] Consequently, the described interaction reduces the level of antibonding destabilisation, resulting in the monoclinic phase, which is stable at room temperature.[99] The Bi 6s/O 2p valence band maximum causes the relatively large hole diffusion lengths in $BiVO_4$, which are about 100-200 nm, compared to TiO_2 for example, which is 10-20 nm.[100–102] A comprehensive approach carried out by Cooper et al., in which they applied a variety of X-ray spectroscopy techniques and DFT calculations, led to further understanding of the electronic structure of $BiVO_4$. Their DFT results indicate, that the valence band is primarily O 2p character, with the valence band maximum comprised of non bonding O $2p_\pi$ states and a contribution from Bi 6s. The conduction band maximum is composed of V 3d states, possessing primarily $d_{x^2-y^2}$ and d_{z^2} character.[99] Inequivalent pairs of oxygen atoms surrounding V atoms reduce the symmetry to C_2, which consequently splits the d-orbitals into triplet bands. Based on these findings an energy level diagram was constructed and is shown in figure 6.

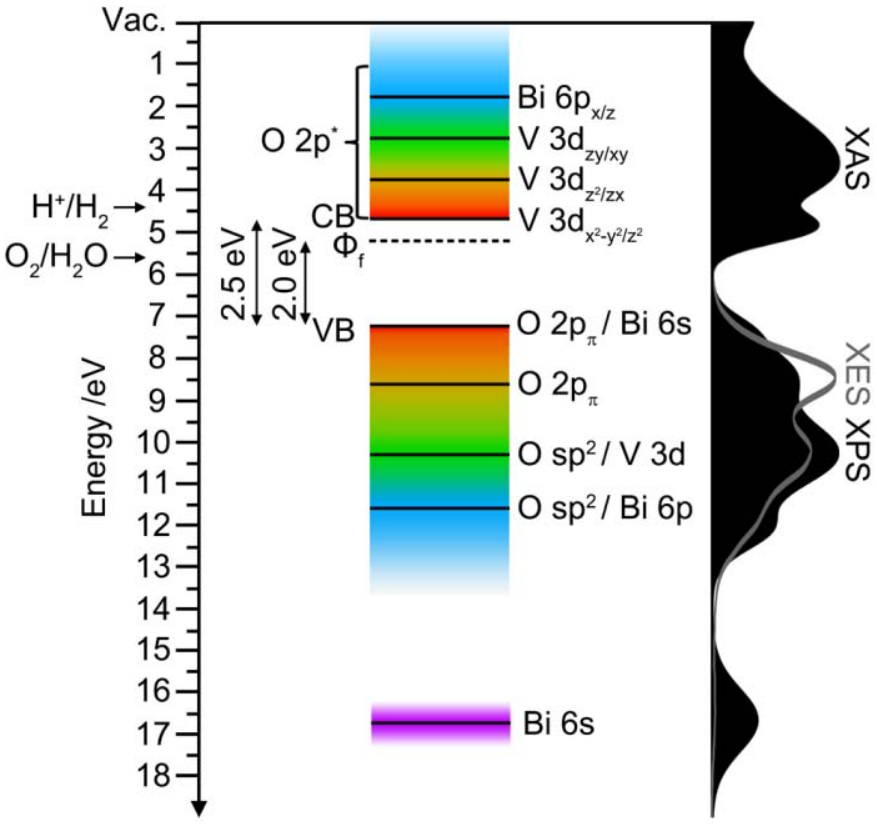

Figure 6: Energy level diagram summarising the results of the work of Cooper et al. for the electronic structure of monoclinic $BiVO_4$. The experimental spectra of X-ray absorption of the empty states of the conduction band and X-ray and photoelectron emission from filled valence states are presented at the right. The Fermi-level is specific to the analysed thin film in their work and was obtained by photoelectron spectroscopy[99]

Das et al. investigated the excitonic effects of $BiVO_4$ for the monoclinic and tetragonal phase and compared it to rutile and anatase. Anatase-TiO_2 and monoclinic $BiVO_4$ both have an indirect band gap and their first exciton is bright and shows polarization perpendicular to the c axis. Compared to rutile-TiO_2 and tetragonal $BiVO_4$, the electron-hole pairs in monoclinic $BiVO_4$ and anatase TiO_2 experience a longer lifetime due to the nature of the indirect band gap. In addition the first exciton of anatase-TiO_2 and monoclinic $BiVO_4$ is bright and polarised perpendicularly to the c-axis. However, the first exciton of the relatively inactive compounds rutile-TiO_2 and tetragonal $BiVO_4$ is dark.[89] The photocatalytic activity is dependent on the exposure of the (010) facet of the m$BiVO_4$ semiconductor, claims Wang et al.[103] To prove this effect, first principles calculations were performed by Yang et al. to compare the properties of the (010) and (011) facets of the $BiVO_4$. The water absorption tests showed that the water absorption energy for the (010) facet is lower than for the (011) facet. Furthermore the calculation of the OER energy pathways reveal, that the OER is thermodynamically favourable on the (010) surface compared to the (011) surface.[97]

1.4.1.1 Synthesis of $BiVO_4$ reported in literature

The most important factor in the phase transition between the three characteristic $BiVO_4$ crystal forms (i.e. monoclinic, zircon-type and tetragonal scheelite) is the temperature. An irreversible transition from zircon-type to monoclinic occurs at around 400–500 °C, while a ferroelastic phase transition between the tetragonal and monoclinic phase occurs reversibly at about 265 °C.[59,104] It was observed that the increase of the calcination temperature from 350 to 800 °C produces an increase in crystallinity and leads to an increase of the O_2 evolution activity of monoclinic $BiVO_4$. Thalluri et al. synthesized monoclinic $BiVO_4$ by precipitation method at ambient temperature, the higher was the calcination temperature (from 350 °C to 800 °C) the lower was the band gap of the powder material (from 2.49 eV to 2.38 eV, respectively). In addition, it was noticed that both crystal size and band gap are correlated with the O_2 evolution activity of $BiVO_4$, which is shown in figure 7.[105,106]

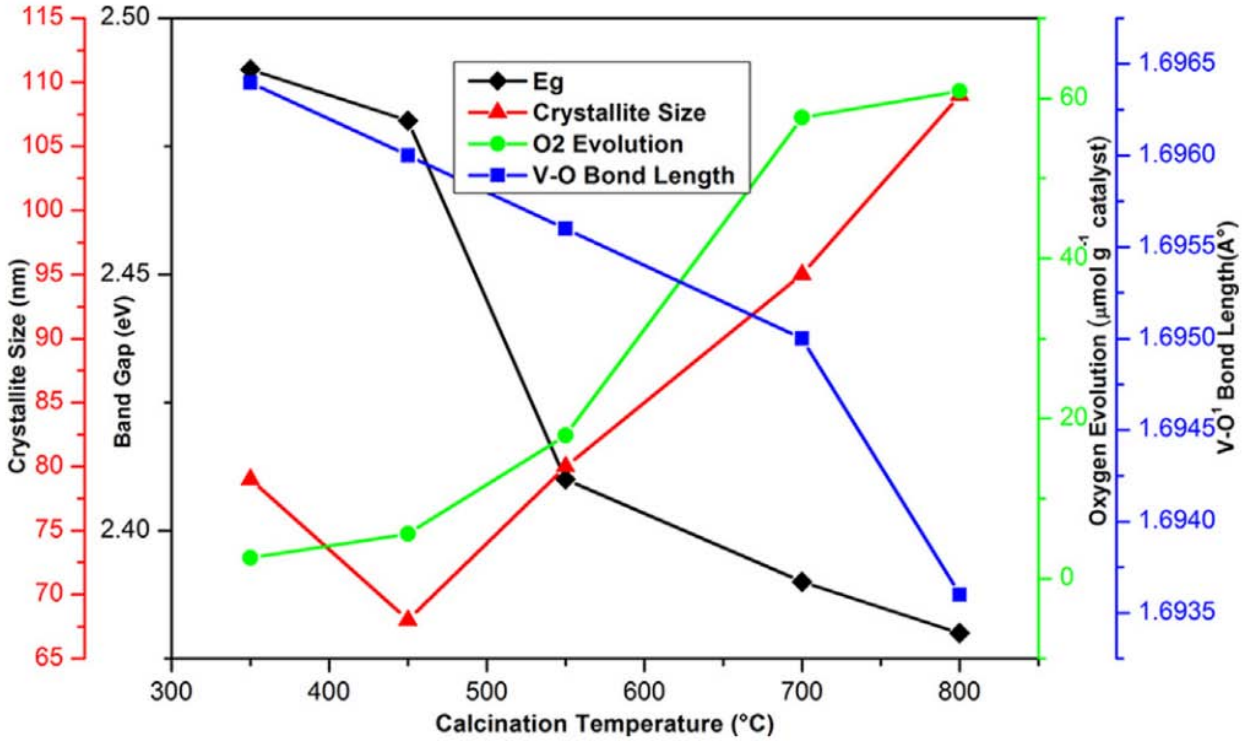

Figure 7: Correlation of characteristic parameters of $BiVO_4$ with O_2 evolution[105]

Lin et al. prepared monoclinic $BiVO_4$ via hydrothermal synthesis at different pH. Their results show, that the morphology, grain size, surface area, and V–O bond length have a strong dependence on the pH value. As the pH value increased, smaller grain size and closer stacking of crystal structure were obtained. Moreover, the key role of pH value for the control of facet exposure, which can affect the photocatalytic performance, has been discussed in their paper.[88] Yu and Kudo et al. synthesised monoclinic $BiVO_4$ over a wide range of pH by a hydrothermal process. The photocatalytic activity was evaluated by investigating the O_2 evaluation rate from aqeous HNO_3 solution. With increasing pH, smaller grain size was observed. However with increasing pH the O_2 evolution rate decreased.[107] Xi et al. synthesised $BiVO_4$ nanoplates and nanorods via hydrothermal route. The photocatalytic activity was evaluated by the O_2 evolution efficiency from aqeous $AgNO_3$ solution. Although the specific surface area of the nanoplates is smaller than that of the nanorods, both the overall and the surface specific activity of the m$BiVO_4$ nanoplates are remarkably higher than those of the nanorods.[108] Zhang et al. analyzed the effect of hydrothermal temperature by fixing the synthesis time to 16 h and varying temperatures from 140 °C to 240 °C. With increasing temperature the photocatalyst size increased and the estimated band gap decreased. In addition, they found out, that samples prepared at low pH contained mixed phase including monoclinic and tetragonal $BiVO_4$.[109] Li's research team prepared $BiVO_4$ crystals exposed with (010) and (110) crystal facets. They found that efficient charge separation can be achieved on different crystal facets. Under the irradiation of visible light, the reduction reaction with photogenerated electrons takes place separately on the (010) facet, whereas the oxidation reaction with photogenerated holes occurs on the (110) facet.[110]

1.4.1.2 Microwave assisted synthesis of $BiVO_4$ reported in literature

Compared to conventional procedure, microwave-hydrothermal process has several advantages such as its rapid synthesis approach, uniform reaction conditions, controlled synthesis environment, ease of synthesis strategy, upright product yield, and enhanced energy efficient, hence it is a reliable technique to synthesize high quality nanomaterials with upright yield.[111–114]

As mentioned above $BiVO_4$ exists in three crystalline phases referred as monoclinic scheelite structure ($mBiVO_4$), tetragonal zircon type structure (t-z $BiVO_4$), and tetragonal scheelite (t-s $BiVO_4$).[91] Monoclinic $BiVO_4$ has been proven to have the best photocatalytic activity among all the crystal structures, however it still has limitations, namely weaker surface adsorption and low charge transport characteristics.[115,116] The heterojunctions between two phases of the same material often have higher interfacial and interparticle transfer rates compared to heterojunctions between two different semiconductors. The heterojunctions between two phases of the same photocatalyst can be achieved by adjusting the pH or the heating temperature during the crystallization process. This simple approach could overcome the disadvantages of pure $mBiVO_4$.[117–119] Microwave irradiation can quickly and evenly heat the substrate in a reaction vessel made out of plastic (Teflon). Hence resulting in a more homogeneous nucleation and a shorter crystallization time, which is very favorable for the synthesis of a highly efficient m-t$BiVO_4$ heterojunction photocatalyst. Yan et al. prepared different $BiVO_4$ photocatalyst phases by varying the ratio of EDTA and EDTA-Na_2 during the synthesis. The synthesised m-t$BiVO_4$ heterojunction photocatalyst showed the highest degradation efficiency for tetracycline among all the crystal phases obtained. The photocatalytic mechanism of the m-t$BiVO_4$ is shown in figure 8 Furthermore the photocatalyst stability was evaluated, where the high decomposition efficiency of tetracycline after four cycles and the obtained XRD pattern indicate, that the photocatalyst has an excellent photostability.[120]

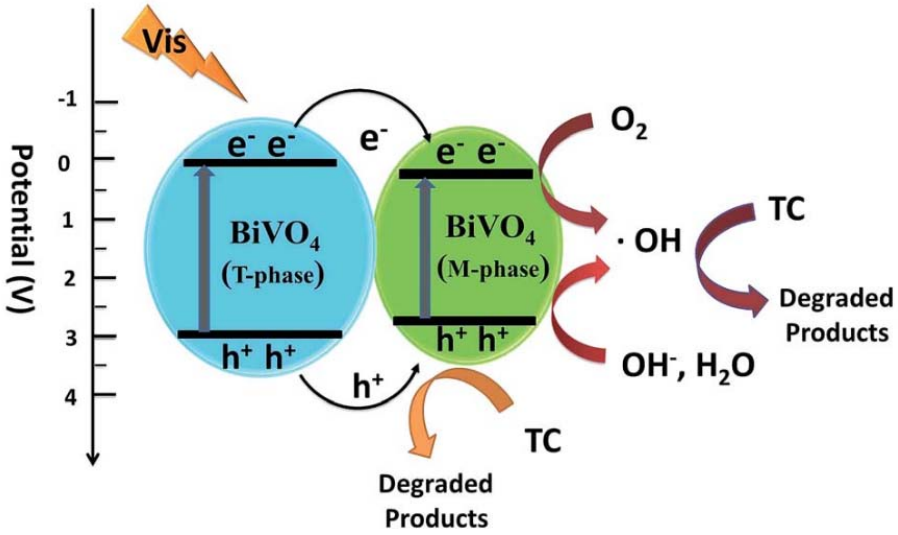

Figure 8: Photocatalytic mechanism of m-t$BiVO_4$ [120]

Zhang et al. prepared monoclinic and tetragonal phases of $BiVO_4$ by controlling the microwave irradiation time and power. The photocatalyst was prepared in an aqueous solution with CTAB as a controlling agent. The photocatalytic properties were investigated by the evaluation of the degradation efficiency of N, N, N', N'-tetraethylated rhodamine and O_2 evaluation efficiency. They found out, that with the time of microwave irradiation prolonging, the tetragonal phase transformed into

monoclinic phase gradually. Furthermore increasing the irradiation power during the reaction leads to narrower band gap of the materials. However in contrast to the results of Yan et al., the working group of Zhang et al. found, that the monoclinic phase had the highest degradation efficiency and O_2 evolution efficiency.[121] Dabodiya et al. confirmed, that longer microwave irradiation time leads to the formation of $mBiVO_4$. They prepared $BiVO_4$ photocatalysts with various crystalline phases and morphologies without any template or surfactant at a fixed power mode of 800 W and constant ramp time by varying the hold time during the reaction. They found out, that at the hold time of 12min leads to 99.92% pure $mBiVO_4$ phase with preferential (010) and (011) crystal facets. However the highest dye degradation efficiency was shown by the mixed phase photocatalyst.[122] The development of specific crystal facets is essential for achieving spatial separation of photogenerated charge carriers, such as the separation of electrons and holes at the (010) and (011) facet of $BiVO_4$.[110] Tan et al. prepared N-doped $BiVO_4$ single-crystalline nanoplates with exposed (040) facets were synthesized via a facile microwave hydrothermal method using NaN_3 as a nitrogen source. In comparison to pure $BiVO_4$ polyhedrons, N-doped $BiVO_4$ nanoplates show higher photocatalytic efficiency. According to the authors the enhancement of photocatalytic activity can be attributed to its small particle size, narrow band gap, and most importantly, existence of multi-atomic BiV_4 centers and surface oxygen vacancies, which can improve the charge–carriers mobility and inhibit the charge–carriers recombination.[90]

Tan et al. investigated the effect of pH during the microwave assisted $BiVO_4$ photocatalyst synthesis. Octahedral and dodecahedron shaped $mBiVO_4$ with exposed 121 and 040 facets were prepared at low pH values (pH=0.59, 0.79), whereat the 121/040 intensity ratio is increasing with increasing pH. Different pH values during the synthesis which result in different morphologies and crystalline phases are shown in figure 9.[118]

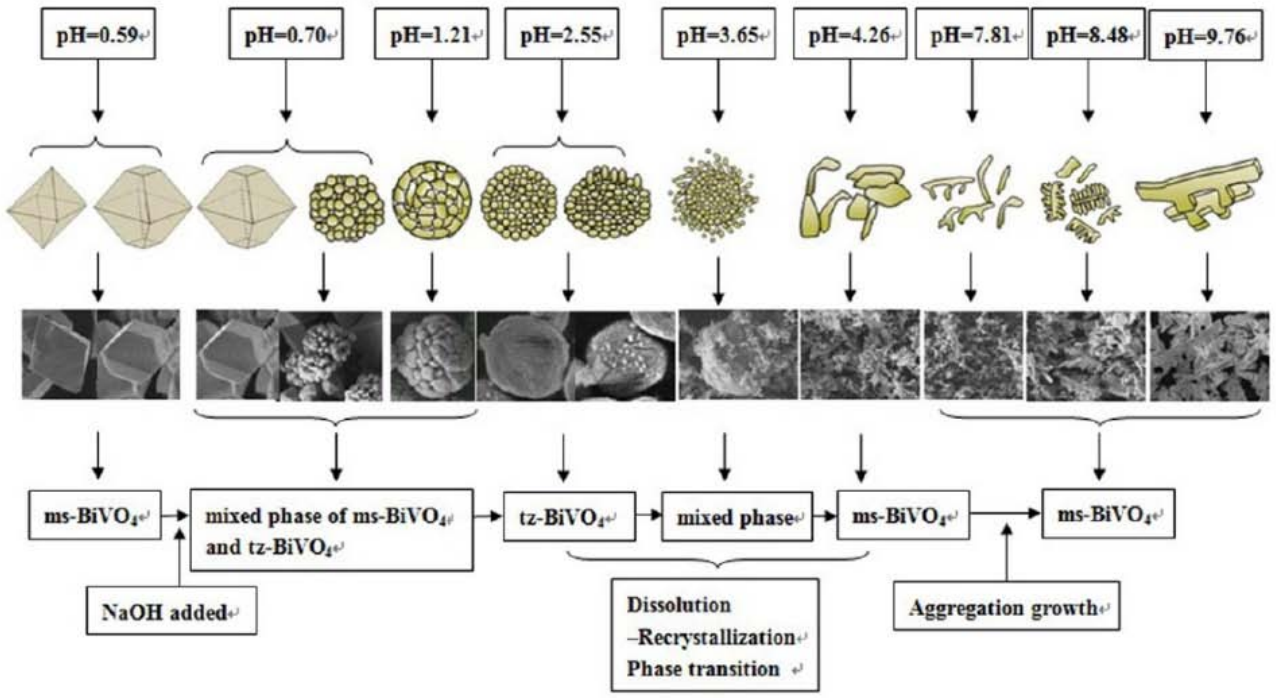

Figure 9: Influence of Different pH Values on the Crystalline Phase and Morphology of $BiVO_4$[118]

Parameters of the microwave synthesis protocol, including pH, temperature, and reaction time,

were varied to control morphology and crystal phase in the synthesis approach of Pingmuang et al. The precursor pH values lower than 7 provided a mixture of monoclinic and tetragonal structures. $BiVO_4$ synthesised at pH>7 provided only monoclinic phase material, with the crystallinity of $BiVO_4$ decreasing as the pH increased. In spite of this decrease in crystal size, surface area also goes down due to heavy agglomeration. The material with the best Rhodamine B degradation efficiency was m$BiVO_4$ with small spherical particles of 50 nm, optical band gap energy of 2.4 eV and pure monoclinic structure was obtained using a pH 7 solution, microwave power less than 300 W, at low temperature (90 °C), and short reaction time (60 min).[123] Shi et al. prepared branched $BiVO_4$ nanocrystal photocatalysts were by a facile microwave-assisted method. Which had unique strawberry-like structure with 5 nm sized mastoids scattered on the 200 nm sized particle surface. The particle surface was decorated with 2wt.% Pt and showed an enhanced degradation of ciprofloxacin compared to pure m$BiVO_4$.[124] Ultrasonication assisted microwave hydrothermal method was carried out for the synthesis of $BiVO_4$ by the working group of Zhang et at. They obtained nut-like, potato-like and broccoli-like nanostructures in different solvents. They found out, that with increasing particle size, the band gap and the photocatalytic activity decreased.[125] Rodrigues et al. reported a study on how the solvent (water, water/ethanol 1:1, ethanol, and ethylene glycol), pH (1 to 14), the use of hexadecyltrimethylammonium bromide (CTAB), and solvothermal vs reflux conditions affect the crystalline structure and morphology of $BiVO_4$ nanomaterials prepared by microwave-assisted methods. They found out, that monoclinic and tetragonal $BiVO_4$ are obtained in acidic media. Also, the use of water and water/ethanol as solvents results in 2D nanomaterials, whereas nanoparticles are observed by using ethanol and ethylene glycol. Finally, the use of CTAB and hydrothermal conditions leads to smaller and denser particles. Furtermore, with increasing pH the band gap of the materials increased as well. They found that monoclinic and or tetragonal $BiVO_4$ is obtained with water as the solvent at a pH ranging from 1 to 10, with ethanol/water 1:1 or pure ethanol as the solvent at an apparent pH range from 1 to 7, and with ethylene glycol at an apparent pH range of 1 to 2. Above these pH values, the obtained materials exhibit very low crystallinity or an α-Bi_2O_3 structure.[126]

1.4.2 $NiFe_2O_4$

1.4.2.1 Synthesis of $NiFe_2O_4$ reported in literature

Spinel nickel ferrite ($NiFe_2O_4$), a multicomponent metal oxide composed only of earth-abundant metals, is an attractive material for visible-light-driven H_2 evolution, because its suitable band gap position and environmental friendliness.[127,128] The possibilities published so far for microwave-assisted hydrothermal synthesis of $NiFe_2O_4$ are not as broad as for $BiVO_4$ therefore only some selected literature for the synthesis of $NiFe_2O_4$ will be presented in this chapter. Wang et al. synthesised $NiFe_2O_4$ with controllable sizes via facile solvothermal synthesis. The average sizes of $NiFe_2O_4$ nanospheres could be controlled from 7 to 200 nm by changing experimental parameters such as the amount of NaOH and reaction duration.[129] Novel spinel-$NiFe_2O_4$/natural mineral (sepiolite, diatomite and kaolinite) composites were developed by Shen et al. using microwave hydrothermal method. $NiFe_2O_4$ nanoparticles with high catalytic activity are obtained under the applied conditions of 1.5 Mpa, 30 min microwave irradiation, and pH=12 of precursors.[130] Lee et al. investigated the optimum conditions to form a single-phase ferrite in detail using the coprecipitation and microwave-hydrothermal methods. The single ferrite-phase in the Ni- and Zn-systems was prepared without any inpurities at 120 °C for 30 min by the microwave hydrothermal reaction.[131] Baykal et al. found, that CTAB is an effective surfactant for the hydrothermal synthesis of $NiFe_2O_4$ with NH_3 and NaOH as hydrolising agents. The working group of Baykal et al. obtained 12nm size nanoparticles of

$NiFe_2O_4$.[132] Kasapoglu et al. performed an EDTA assisted synthesis of $NiFe_2O_4$ which resulted in octahedral shaped nanoparticles.[133] Highly crystalline $NiFe_2O_4$ nanoparticles were synthesised by Dinkar et al. via hydrothermal synthesis with glycerol as a surfactant and NaOH as precipitating agent. Dependent on the surfactant concentration they obtained octahedral and sherical shaped nanoparticles.[134] Xiangfeng et al. prepared $NiFe_2O_4$ nanocubes and nanorods dependent on the pH value of the precursors.[135]

1.4.3 Motivation

The purpose of the current work is the development of a facile microwave assisted hydrothermal synthesis protocol for $BiVO_4$ and $NiFe_2O_4$ photocatalysts, and the evaluation of the water splitting activities of them. As already described in chapter **??**, there were some research groups working on the optimization of microwave-assisted synthesis of $BiVO_4$. Tan et al. found, that between the pH range of 0.59 and 0.79 the 040/121 facet ratio in the octahedral morphology increases with increasing pH.[90] However, the work of Tan et al. leaves some questions unanswered, namely: Is it possible to accurately adjust the degree of exposure from the 040 facet with the minimum change in pH? How does the morphology change at slightly lower and higher pH values? The hold time of the microwave irradiation during the synthesis played an essential role in $BiVO_4$ phase composition and morphology according to Dabodiya et al. In their paper it was published, that 12 minutes of microwave irradiation leads to m$BiVO_4$ crystals with exposed (010) (011), whereby reduced irradiation times resulted in a mixture of monoclinic and tetragonal $BiVO_4$.[122] This work focuses, among others, on the question, how the formation mechanism of monoclinic $BiVO_4$ with an octahedral morphology is at short microwave irradiation times. In the paper by Rodrigues et al., it was published that the use of a mixture of ethanol and water instead of only water in microwave assisted hydrothermal synthesis leads to a 2D morphology, and the use of cetyl trimethyl ammonium bromide (CTAB) as surfactant causes a decrease in particle size, consequently the resulting particles were also denser.[126] From the information obtained from the publication of Rodrigues et al. the question arises: Can the crystal facet growth be controlled with addition of ethanol and/or surfactants to the reaction mixture? After the successful synthesis of $BiVO_4$ and after the evaluation of the oxygen evolution reaction activity of each of the samples the oxygen evolution reaction activity can be linked to the pH value during preparation, the irradiation time, the amount of solvent and type of surfactant in the reaction mixture. With the best samples, heterojunction formation can be tried out with a semiconductor, which is capable of hydrogen evolution reaction. Because of its suitable band gap $NiFe_2O_4$ is a promising candidate for the hydrogen evolution reaction. In the previous publications, the microwave assisted synthesis of $NiFe_2O_4$ was little mentioned therefore this work focuses on the optimization of the synthesis process of microwave-assisted hydrothermal synthesis of $NiFe_2O_4$. In case of successful synthesis of $NiFe_2O_4$ and its good hydrogen evolution activities, heterojunction between $BiVO_4$ and $NiFe_s$hould be tried to ensure better activity in water splitting.

2 Experimental

2.1 Chemicals

All chemicals used for the synthesis were obtained by commercial suppliers. $Ni(NO_3)_2 \times 6H_2O$ from Sigma Aldrich (99.9% pure), $Fe(NO_3)_3 \times 9H_2O$ from Art 3883 (99% pure), NH_4VO_3 from Roth (99.8% pure) and $Bi(NO_3)_3 \times 5H_2O$ from Riedel de Haen (98% pure), cetyl trimethyl ammonium bromide (CTAB) from Carl Roth (98% pure), sodium dodecylbenzenesulfonate from Sigma Aldrich (technical grade). The solvent used for the syntheses was deionized water.

2.2 Characterisation

In order to obtain visual information on the morphology of the sample, scanning electron microscopy (SEM) images were taken using FEI Quanta 250 FEG at 200 keV scanning electron microscope. For the sample preparation a small amount of powder was placed on a sticky carbon tape and was evacuated. The SEM image was recorded at a typical acceleration voltage of 10 kV.

X-ray diffraction (XRD) was performed using XPERT II: PANalytical XPert Pro MPD (Θ–Θ Diffractometer). A few mg of the sample was placed on a Si-sample holder and irradiated with a Cu X-ray source (8.04 keV, 1.5406 Å). The signal was obtained with Bragg–Brentano Θ/Θ-diffractometer geometry ranging from 5° to 50° degrees while rotating the sample. The detector system was a semiconductor X'Celerator (2.1°) detector. For the calculation of the 040/121 facet ratio, the raw data of the XRD measurements of the monoclinic $BiVO_4$ samples were used. The value of the intensity of the peak at 31 2Θ (040 facet) was divided with the value of the intensity of the peak at 28.5 2Θ (121 facet) to get the 040/121 facet ratio which will be used later in chapter 3.

Diffuse reflectance spectroscopy (DRS) was used to investigate the optical absorption properties of different powder samples. For that, a few mg of a powder-sample were inserted into the sample holder of a Jasco V-670 Spectrophotometer. The reflectance was then measured for wavelengths between 190 nm and 900 nm.

Attenuated total reflectance Fourier transformed infrared spectroscopy (ATR-FTIR) measurements were performed using a Tensor 27 FTIR from Bruker equipped with a ZnSe crystal. For each measurement the ZnSe crystal was covered with a few mg of a crystalline sample. A background spectrum of air was collected which was then subtracted from the actual sample spectrum. The spectra were recorded from 400 cm^{-1} to 4000 cm^{-1} with a resolution of 4 cm^{-1} and 32 scans.

Raman measurements were conducted with LabRAM HR800 from Horiba. Ne:YAG diode was used as the 532 nm laser source and the characteristic Raman peak of Si at 520.8 cm^{-1} was used as the calibration peak. The laser intensity was keep at 5 mW.

2.3 Determination of the catalyst activity

2.3.1 OER experiments

The photocatalytic O_2 evolution from an aqueous silver nitrate solution were used as model reactions to determine the photocatalytic properties of the synthesized materials. A total content of 1 mg of the catalyst power was dispersed by a magnetic stirrer in 2 mL of an aqueous $AgNO_3$ solution (1.725mg/mL) in a 2 necked watercooled, quartz-glass reactor. As a light source a monochromatic visible light LED lamp with a wavelength of 445 nm ± 20 nm (SOLIS 445-C from Thorlabs) was

used, and the illumination was carried out from the side. A needle-type, optical oxygen sensor (FireSting Pro from pyroscience) was used to detect the concetration of O_2. The OER setup is shown in figure 10.

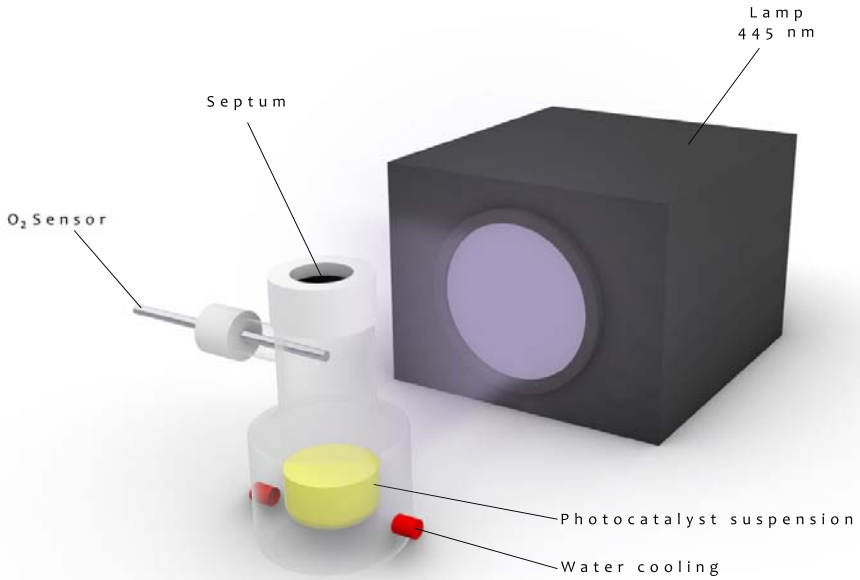

Figure 10: Schematic OER setup

2.4 General preparation of $BiVO_4$

Solution A: $Bi(NO_3)_3 \times 5H_2O + H_2O + HNO_3$

Solution B: $NH_4VO_3 + H_2O$

$Bi(NO_3)_3 \times 5H_2O$ was dissolved in distilled water and HNO_3 was stirred for 30 min at room temperature. NH_4VO_3 was dissolved in boiling distilled water and was stirred and heated for 30 min. The NH_4VO_3 was added dropwise to the $Bi(NO_3)_3 \times 5H_2O$ solution under vigrous stirring. After stirring for 20 min at room temperature, the reaction mixture was transferred in a 30 mL microwave vial. The reaction was carried out in an Anton Paar 400 monowave at 200 °C. The samples were fitrated, washed with water and ethanol three times and were put in the oven at 60 °C overnight. The general preparation of $BiVO_4$ is shown in figure 11.

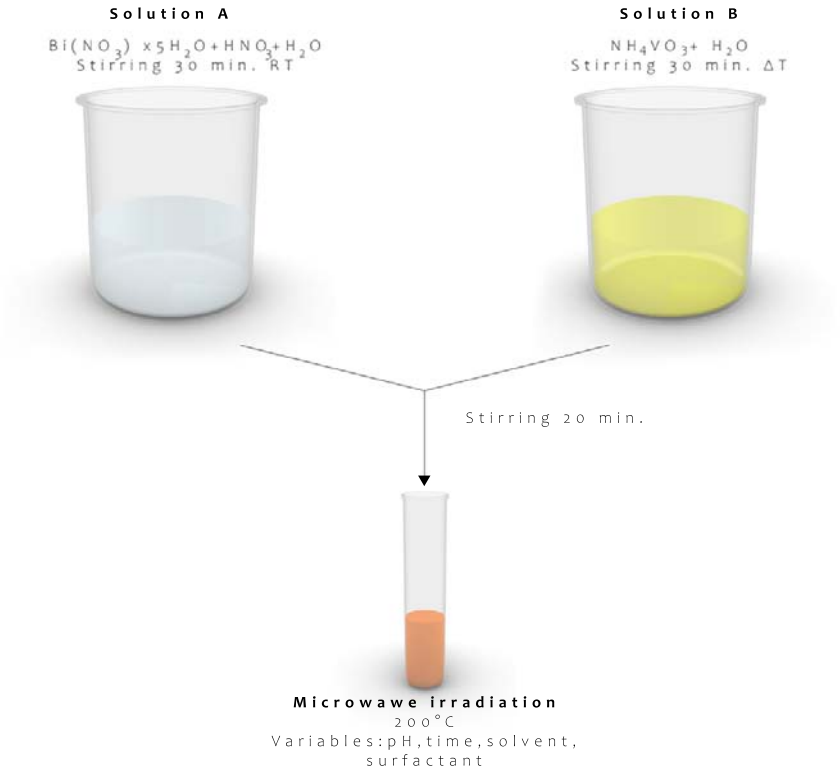

Figure 11: General microwave assisted hydrothermal synthesis scheme of $BiVO_4$

2.4.1 pH-variation

The general preparation of $BiVO_4$ is found in section 2.4. In this section the samples are listed, which were prepared at different pH values. The exact amount of precursor in mmol, added water and HNO_3 in mL, furthermore the reaction time minutes and the resulting pH value is found in table 1 and 2. The sample with the number 02 was prepared with the addition of 0.16 mL 100% HNO_3. Furthermore one part of this sample was put in the oven at 120 °C overnight and is marked suffix '-oven' in the following sections. Every other sample was prepared with the addition in table 1 and table 2 specified amount of 60% HNO_3. At the preparation of the samples with the number 08, 09 and 10, the precursor amount was reduced to $\frac{1}{5}$ while the reaction volume stayed the same, which resulted in a 0.05 $\frac{\text{mol}}{\text{L}}$ solution of the precursors. The synthesis details of the samples with the number 74-78 are shown in table 2. The preparation of these samples was carried out by reducing the reaction volume with $\frac{1}{3}$, which resulted in a 0.25 $\frac{\text{mol}}{\text{L}}$ solution of the precursors.

Table 1: Synthesis details of $BiVO_4$ with different pH values

Sample number	**01**	**02**	**03**	**04**	**05**	**06**	**07**	**08**	**09**	**10**
Precursor [mmol]	3.75	3.75	3.75	3.75	3.75	3.75	3.75	0.75	0.75	0.75
water [mL]	12.57	14.84	14.84	7.9	7.9	7.87	7.87	7.84	7.87	7.9
HNO_3 [mL]	2.43	$0.16^{100\%}$	$0.16^{60\%}$	0.1	0.1	0.13	0.13	0.16	0.13	0.13
concentration $\frac{mol}{L}$	0.25	0.25	0.25	0.25	0.25	0.25	0.25	0.05	0.05	0.05
pH	**-0.59**	**0.88**	**0.88**	**1.4**	**1.4**	**1.076**	**1.076**	**0.88**	**1.076**	**1.4**
reaction time [min]	40	40	40	40	40	40	40	40	40	40

Table 2: Synthesis details of $BiVO_4$ with different pH values

Sample number	**74**	**75**	**76**	**77**	**78**
Precursor [mmol]	1.25	1.25	1.25	1.25	1.25
water [mL]	4.91	4.915	4.92	4.925	4.93
HNO_3 [mL]	0.09	0.085	0.08	0.075	0.07
concentration [mol/L]	0.25	0.25	0.25	0.25	0.25
pH	**-0.03**	**0.011**	**0.08**	**0.125**	**0.45**
reaction time [min]	40	40	40	40	40

2.4.2 Optimisation of the synthetic conditions

According to the scanning electron microscopy and the X-ray powder diffraction results of the samples prepared at different pH value, of which the synthesis details were described in section 2.4.1, the sample with the number 02 was chosen. This material exhibited excellent morphology, further resulting in a pure-phased monoclinic material. The synthesis was repeated and is shown in table 3. These samples are labeled with the sample number 29, 30 and 31. These synthesis was repeated with a reduced volume of $\frac{1}{3}$ (sample 38) and $\frac{1}{5}$ (sample 39) as well.

Table 3: Synthesis details of the repeated synthesis of the selected reference of $BiVO_4$

Sample number	**29**	**30**	**31**	**38**	**39**
Precursor [mmol]	3.75	3.75	3.75	1.25	0.75
water [mL]	14.84	14.84	14.84	4.95	2.49
HNO_3 [mL]	0.16	0.16	0.16	0.05	0.01
pH	1.3	1.3	1.3	1.3	1.3
concentration [mol/l]	0.25	0.25	0.25	0.25	0.25
reaction time [min]	40	40	40	40	40

2.4.3 Time variation

The general preparation of $BiVO_4$ is found in section 2.4. In this section the samples are listed, which were prepared with the reference pH value of 1.3 at different reaction times. The exact amount of precursor in mmol, added water and HNO_3 in mL, furthermore the reaction time in minutes is found in table 4.

Table 4: Synthesis details of $BiVO_4$ with different reaction times

Sample number	**70**	**43**	**44**	**45**	**46**	**47**	**48**	**69**	**49**	**50**	**71**	**51**	**52**	**33**	**32**
Precursor [mmol]	1.25	3.75	1.25	1.25	1.25	1.25	1.25	1.25	1.25	1.25	1.25	1.25	1.25	3.75	3.75
water [mL]	4.95	14.84	4.95	4.95	4.95	4.95	4.95	4.95	4.95	4.95	4.95	4.95	4.95	14.84	14.84
HNO_3 [mL]	0.05	0.16	0.05	0.05	0.05	0.05	0.05	0.05	0.05	0.05	0.05	0.05	0.05	0.16	0.16
pH	1.3	1.3	1.3	1.3	1.3	1.3	1.3	1.3	1.3	1.3	1.3	1.3	1.3	1.3	1.3
reaction time [min]	**0**	**2**	**2**	**4**	**4**	**6**	**6**	**6**	**8**	**8**	**8**	**10**	**10**	**20**	**60**

2.4.4 Solvent variation

The general preparation of $BiVO_4$ is found in section 2.4. In this section the samples are listed, which were prepared with the reference pH value of 1.3 with different amounts of ethanol added. The exact amount of precursor in mmol, added water and HNO_3 in mL, furthermore the reaction time in minutes is found in table 5.

Table 5: Synthesis details of $BiVO_4$ with different amounts of Ethanol

Sample number	**72**	**73**	**34**	**40**	**53**	**35**	**41**	**36**	**42**	**37**
Precursor [mmol]	1.25	1.25	1.25	1.25	1.25	1.25	1.25	0.75	1.25	1.25
water [mL]	4.95	4.75	3.7	3.7	3.7	2.45	2.45	1.2	1.2	-
HNO_3 [mL]	0.05	0.05	0.05	0.05	0.05	0.05	0.05	0.05	0.05	0.05
pH	0.88	0.88	0.88	0.88	0.88	0.88	0.88	0.88	0.88	0.88
reaction time [min]	40	40	40	40	2	40	40	40	40	40
Ethanol [mL]	**0.05**	**0.25**	**1.25**	**1.25**	**1.25**	**2.5**	**2.5**	**3.75**	**3.75**	**4.95**
Ethanol [%]	**1**	**5**	**25**	**25**	**25**	**50**	**50**	**75**	**75**	**100**

2.4.5 Surfactant variation

The general preparation of $BiVO_4$ is found in section 2.4. In this section the samples are listed, which were prepared with the reference pH value of 1.3 with the surfactant sodium dodecylbenzonesulfonate (SDBS) and Cetyltrimethylammoniumbromid (CTAB). The exact amount of precursor in mmol, added water and HNO_3 in mL, furthermore the reaction time in minutes is found in table 6.

Table 6: Synthesis details of $BiVO_4$

Sample number	**67**	**68**
Precursor [mmol]	1.25	1.25
water [mL]	4.95	4.95
HNO_3 [mL]	0.05	0.05
pH	1.3	1.3
reaction time [min]	40	40
Surfactant [mg]	**25^{SDBS}**	**5^{CTAB}**

2.5 Synthesis of $NiFe_2O_4$

0.5 mmol $Ni(NO_3)_3 \times 6H_2O$ and 1 mmol $Fe(NO_3)_3 \times 9H_2O$ was dissolved in distilled water and was stirred for 10 min at room temperature. 1M NaOH was dropped to the solution, til the desired pH was obtained, and the mixture was stirred for additional 3 min. The reaction mixture was transferred in a 30 mL microwave reaction vial and the synthesis was carried out at 180 °C for 30 min. The samples were filtrated and washed three times with water. The product was left to dry in an oven at 60 °C overnight.

Table 7: Synthesis details of $NiFe_2O_4$

Sample number	**11**	**12**	**13**	**14**	**15**
water [mL]	13.5	13.5	12.15	9.15	4.8
1M NaOH [mL]	1.5	1.5	2.85	5.85	10.25
pH	1.89	1.89	3	11	14

2.5.1 pH variation

0.5 mmol $Ni(NO_3)_3 \times 6H_2O$ and 1 mmol $Fe(NO_3)_3 \times 9H_2O$ was dissolved in distilled water and was stirred for 10 min at room temperature. 1M NaOH was dropped to the solution, til the desired pH was obtained, and the mixture was stirred for additional 3 min. The reaction mixture was transferred in a 30 mL microwave reaction vial and the synthesis was carried out at 180 °C for 30 min. The samples were filtrated and washed three times with water. The product was left to dry in an oven at 60 °C overnight. The exact amount of added water and HNO_3, furthermore the resulting pH value is shown in table 8.

Table 8: Synthesis details of $NiFe_2O_4$

Sample number	**18**	**19**	**20**	**21**	**22**	**23**	**24**	**25**	**26**	**27**	**28**
water [mL]	11	11.2	11.3	11.4	10.25	10.31	10.36	10.36	10.4	10.2	7
1M NaOH [mL]	4	3.8	3.7	3.6	4.75	4.69	4.64	4.64	4.6	4.8	8
pH	6.4	6	4.46	3.89	10.5	10	9.5	9.5	9	8.5	14

2.5.2 Time and temperature variation (pH: 9.5, 10)

0.5 mmol $Ni(NO_3)_3 \times 6H_2O$ and 1 mmol $Fe(NO_3)_3 \times 9H_2O$ was dissolved in distilled water and was stirred for 10 min at room temperature. 1M NaOH was dropped to the solution, til the desired pH was obtained, and the mixture was stirred for additional 3 min. The reaction mixture was transferred in a 30 mL microwave reaction vial and the synthesis was carried out via microwave irradiation. The samples were filtrated and washed three times with water. The product was left to dry in an oven at 60 °C overnight. The exact amount of added water, HNO_3 in mL, and the resulting pH value, furthermore the exact Temperature and microwave irradiation time is shown in table 9.

Table 9: Synthesis details of $NiFe_2O_4$

Sample number	**54**	**55**	**56**	**57**	**58**	**59**	**60**	**61**	**62**	**63**	**64**	**65**	**66**
Fe precursor [mmol]	0.00033	0.001	0.00033	0.00033	0.00033	0.00033	0.00066	0.001	0.001	0.001	0.001^{FeCl_3}	0.001^{FeCl_3}	0.001
water [mL]	3.46	0.36	3.46	3.46	3.44	3.46	6.9	10.31	10.31	10.36	14	14	14
1M NaOH [mL]	1.54	4.64	1.54	1.54	1.56	1.54	3.08	4.69	4.69	4.64	1^{NH4OH}	1^{NH4OH}	1^{NH4OH}
pH	9.5	9.5	9.5	9.5	10	10	10	10	10	9.5	9.5	9.5	9.5
reaction temperature [°C]	200	200	200	220	200	240	220	220	220	220	220	200	200
reaction time [min]	30	30	30	30	30	40	40	40	60	60	60	60	60

3 Results and Discussion

In this chapter, the results of $BiVO_4$ are presented. First, the results of the pH-dependent synthesis are discussed, whereat the optimization of the morphology of $BiVO_4$ was tried. Then, the results of the monoclinic $BiVO_4$ semiconductors synthesized by the microwave irradiation time dependent synthesis will be discussed. Finally, the properties of the photocatalysts obtained by the solvent-dependent synthesis are analyzed. The subsections of the results section are divided in the following way: First, the scanning electron microscopy (SEM) images, which represents the synthesis series well are shown and discussed. The SEM images of all products are shown in the appendix. Subsequently, the X-ray powder diffraction (XRD) results of all products are shown and discussed in the following chapter. Additionally the values determined for the crystallite size, which were obtained via Sherrer equation from the XRD data are presented as well. After that, the diffuse reflectance spectra (DRS) of all synthesized materials are discussed, and the calculated band gaps obtained from the Tauc-plot are presented as well. In addition, the Fourier-transformed infrared spectroscopy (FT-IR) spectra of the semiconductors obtained in the solvent-dependent synthesis were recorded and are discussed. Finally, the oxygen evolution reaction activities of all $BiVO_4$ photocatalysts are shown. The dependence of the catalytic activity on the type of polymorph, the morphology, the size of the material, the crystallite size and the band gap are determined.

3.1 pH dependent synthesis

The variation of the pH during the synthesis of the photocatalyst material was carried out, in order to obtain $BiVO_4$ with well defined crystal structure and morphology. The synthesis details are shown in section 2.4.1. According to the findings of Tan et al.[118], it is expected, that with increasing pH, the 121/040 facet intensity ratio increases as well. For the investigation of the effect of the pH on the morphology of the material, the pHs -0.03, 0.011, 0.08, 0.125, 0.45, 0.88, 1.076 and 1.4 was tried out at a constant temperature of 200 °C and constant irradiation time of 40 minutes. In the following, the appearance, SEM, XRD and DRS of the samples resulted from the pH dependent synthesis are discussed.

3.1.1 Appearance

Figure 12 shows the appearance of zircon tetragonal (a) and monoclinic (b) $BiVO_4$. The zircon tetragonal $BiVO_4$ appears to be a pale yellow colored powder. However, the monoclinic $BiVO_4$ resulted in bright yellow powder, based on the XRD data as will be discussed in section 3.1.3. As already mentioned in section 1.4.1 the difference between monoclinic and tetragonal $BiVO_4$ is reflected in the structural distortion of the VO_4 tetrahedra in the monoclinic phase. Thus, the distance between Bi^{3+} and O^{2-} in the monoclinic structure is different from that in the tetragonal structure, which leads to orbital hybridization and has an influence on the value of the band gap.[89] The band gap of monoclinic $BiVO_4$ is 2.4 eV. The band gap of zircon tetragonal $BiVO_4$ is around 2.8 eV.[88,136] The coloration mechanism of monoclinic $BiVO_4$ upon visible light absorption results from the charge transfer transition between the hybrid orbital Bi 6s/O 2p located in the valence band and the 3d conduction band of vanadium. It can be concluded, that the monoclinic phase shows vivid yellow color, because of its narrower band gap, which leads to more visible light absorption than for the tetragonal phase.[95,137]

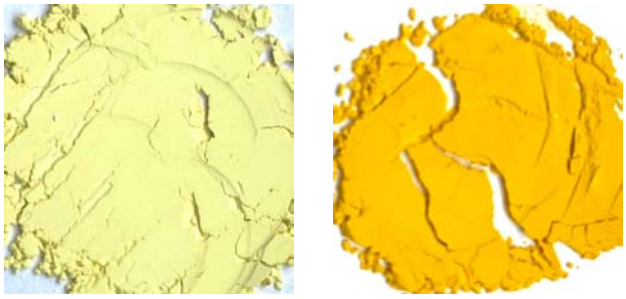

(a) $tBiVO_4$ powder (b) $mBiVO_4$ powder

Figure 12: Zircon tetragonal and scheelite monoclinic $BiVO_4$ powder

3.1.2 Scanning electron microscopy

Figure 13 shows the most expressive morphologies, which were obtained in the scanning electron microscopy (SEM) results of the crystalline $BiVO_4$ products. Table 10 summarizes the different morphology designations of the subfigures of figure 13. In the following these designations are used to describe the morphology of the obtained crystals, which were prepared at different pH values. Additional SEM images are shown in the appendix.

Table 10: Morphology designations of the subfigures in figure 13

Subfigure	Morphology
a)	capped octahedron
b)	polyhedron
c)	cluster of polyhedra
d)	sphere consisting of smaller particles
e)	sphere
f)	layered structure
g)	plate like
h)	needle like

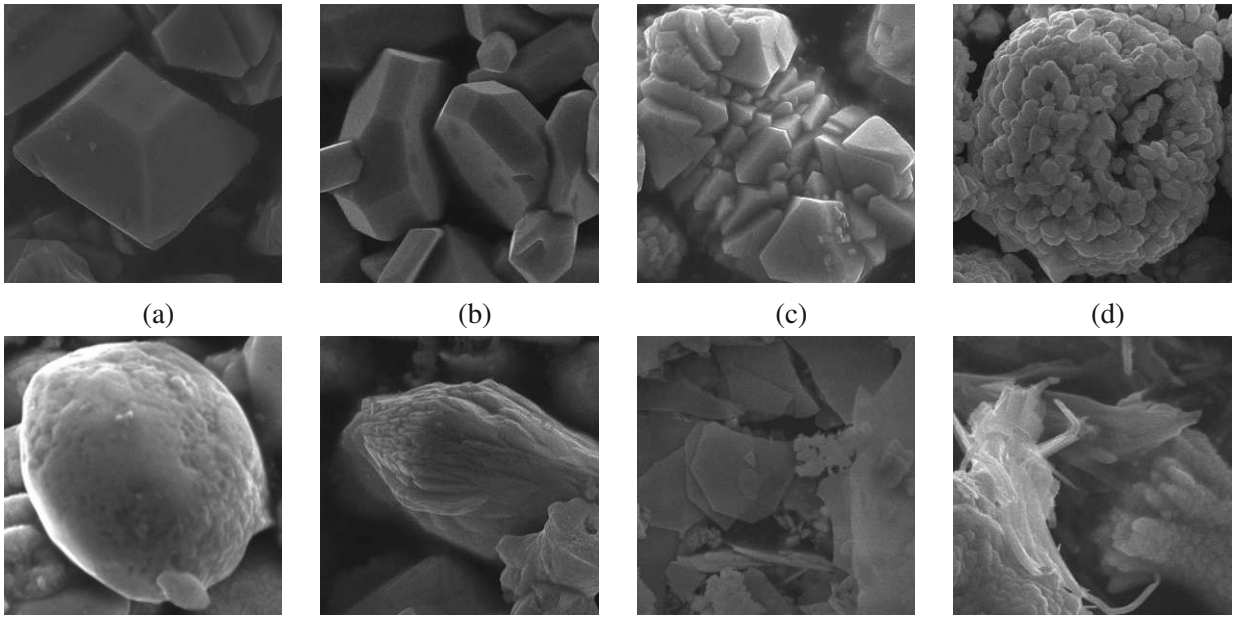

Figure 13: SEM images of different morphologies of crystalline $BiVO_4$ products

The microwave assisted synthesis of $BiVO_4$ was carried out at different pH values, of which synthesis details are shown in table 1, which is shown in section 2.4.1.

Figure 14 serves as a good representation of the morphology of the pH-dependent synthesis, whereat for each pH value used in the synthesis, a SEM image is shown. It is visible, that low pH, namely -0.032 and 0.011 resulted in sphere like morphology, or irregular shaped particles. The samples which were prepared at the pH of 1.076 and 1.4 resulted in irregular shaped particles or a mixture of polyhedron and irregular shaped particles. From figure 14 it is visible, that for the formation of octahedron shaped particles the optimum pH range is 0.08-0.88. Furthermore, the samples prepared in the pH range of 0.08-0.88 resulted in bright yellow powder which was an indication of monoclinic $BiVO_4$. Hence it can be said, that in order to obtain monoclinic $BiVO_4$ with well defined morphology the pH value during the synthesis must be adjusted carefully.

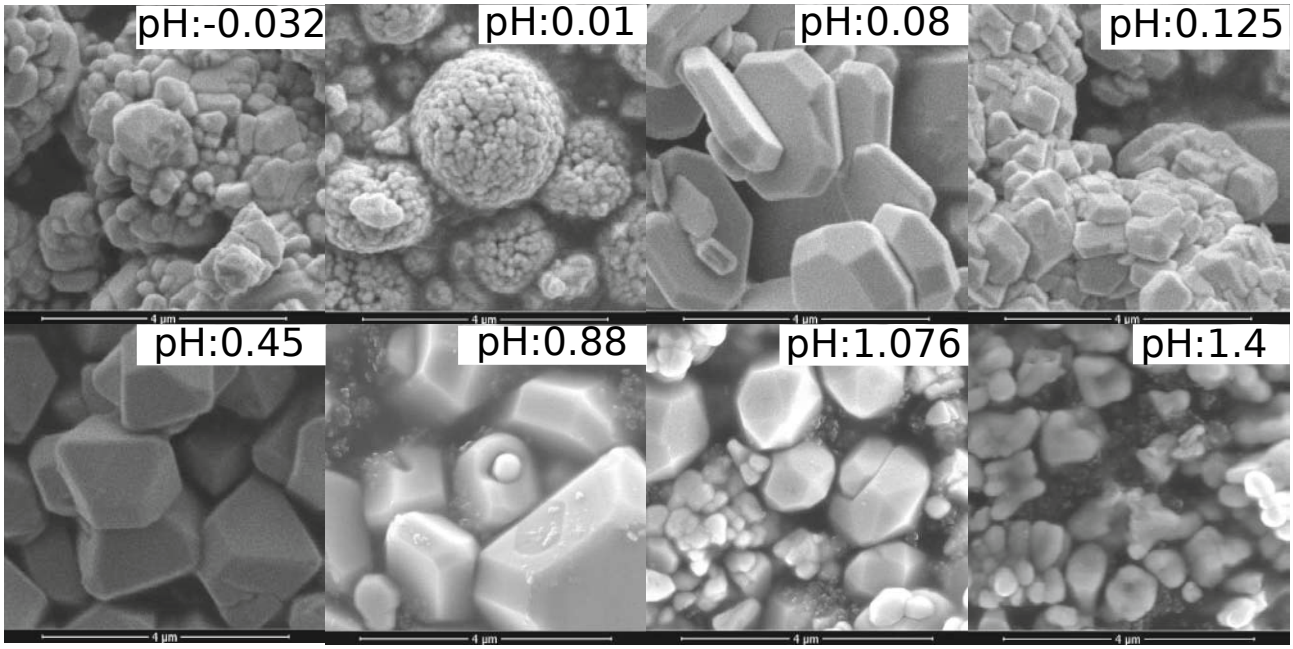

Figure 14: Morphology of the samples, which were synthesized with different pH values during synthesis

3.1.3 X-ray powder diffraction

The X-ray powder diffractograms of $BiVO_4$ are shown in figure 15. In figure 15 a) the XRD powder diffractograms of the samples are shown, which were prepared at 3 different pH values during the synthesis, namely 0.88, 1.076 and 1.4. One of the most characteristic feature of the XRD spectrum of the monoclinic $BiVO_4$ is the splitting peaks at the position of 18.5 2Θ, 35 2Θ and 45 2Θ. The XRD spectrum of the scheelite tetragonal $BiVO_4$ shows the same peak positions as the monoclinic $BiVO_4$, but they can be distinguished by the presence of the splitting peaks. One of the most significant peak, which tells the presence of tetragonal $BiVO_4$ is the peak at 24 2Θ. The diffractogram of the samples, which were prepared at the pH of 1.076 shows, that a composite material between t-s $BiVO_4$ and t-z $BiVO_4$ is obtained, because for the tetragonal $BiVO_4$ characteristic peak at 24 2Θ is visible. Additionally there are peaks visible at the positions of the black dashed line, which should represent monoclinic $BiVO_4$, but these peaks are not splitting peaks, so the sample, which was prepared at the pH of 1.076 resulted in a mixed phase of zircon tetragonal and scheelite tetragonal $BiVO_4$. However, on the X-ray diffractogram of sample 09, which was prepared at the pH of 1.076 an unidentified peak is visible at approximately 22 2Θ. The origin of the peak was identified via the Highscore XRD analysis software. The peak could originate from VBi_2O_5 [138] or $V_3Bi_{5.4}O_{15}$ [139]. According to the diffractogram, the samples, which were prepared at the pH of 0.88 and 1.4 have only matching peak positions with the reference of monoclinic $BiVO_4$, additionally they show the characteristic splitting peaks at 18.5 2Θ, 35 2Θ and 45 2Θ hence it is assumed, that pure phased m$BiVO_4$ was obtained. In summary, the samples which were prepared at the pH of 0.88 and pH of 1.45 resulted in monoclinic $BiVO_4$. However, the samples, which were prepared at the pH of 1.076 resulted in a composite between scheelite-tetragonal and zircon-tetragonal $BiVO_4$. This results show, that within the pH range from 0.88 to 1.45, the system could be in a metastable state such that even small synthetic variations, namely precursor ratio and preparation temperature can trigger the formation of a mixed-phase compound. The intensity ratio of the 040 and 121 is in high correlation with the SEM images,

since sample 03 and 05 shows highly exposed 040 facets, while as for sample 02 and 08 the 040 facet exposure is negligible.

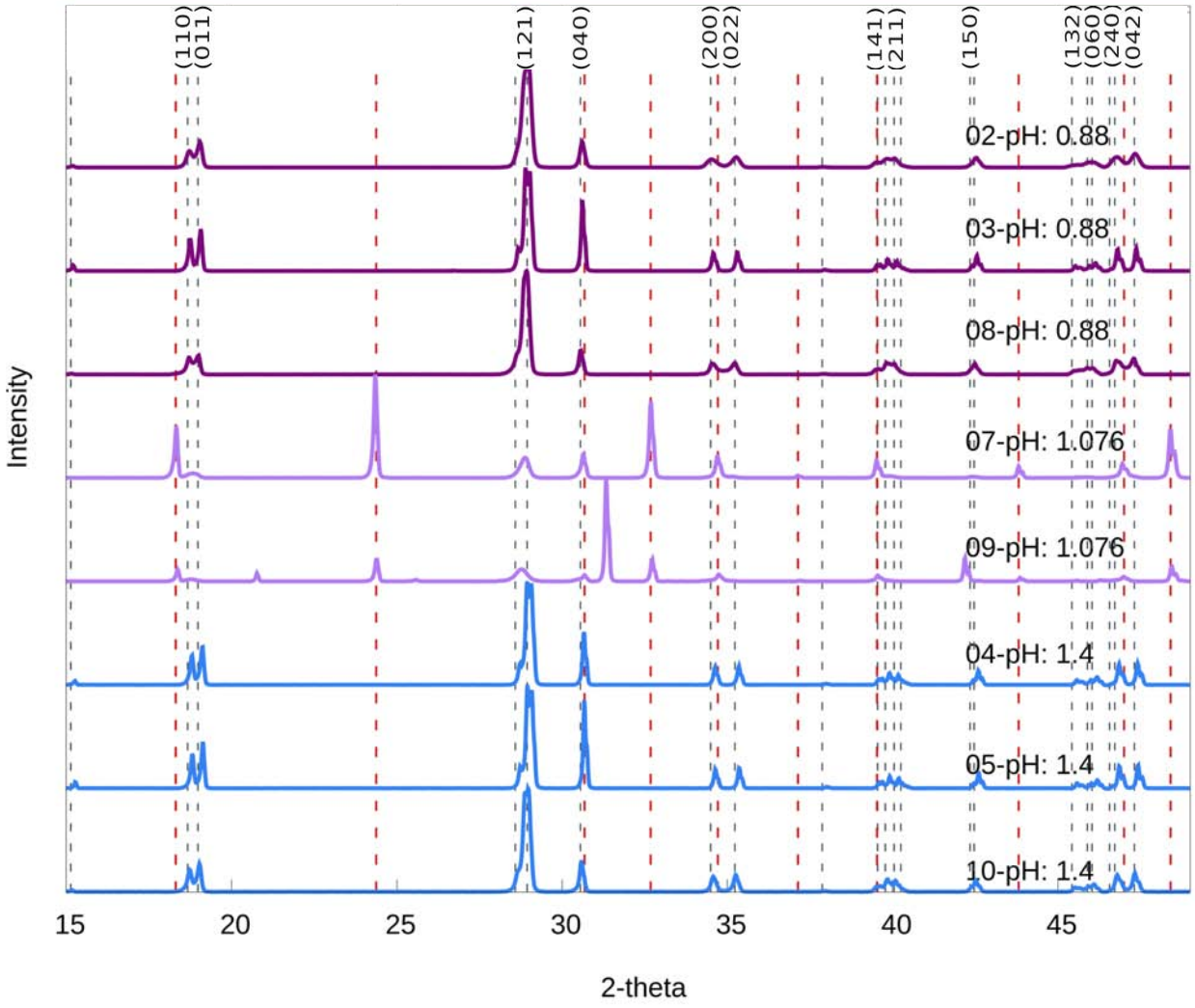

Figure 15: X-ray powder diffractogram of $BiVO_4$ samples, which were prepared by a pH dependent synthesis with constant irradiation temperature of 200 °C and irradiation time of 40 min. The diffractogramms have the following notation: sample number-pH value. The black dashed line represents the reference peak positions of $mBiVO_4$ and the red dashed line represents t-z $BiVO_4$

The crystal size of the samples were calculated using the Scherrer equation, which is shown in equation 9. Where T is the crystallite sine in nm, B is the full width at half maximum (28.5, 31 and 42 2Θ), Θ is the Bragg angle (deg), k is 0.9 and λ is 15.4 Å. The calculation of the crystallite size reveals the size of the smallest single crystal in a particle. The crystallite sizes of the samples prepared at variable pH are shown in table 11. There is no apparent trend between the crystallite sizes and the preparation conditions, however, pH variation allowed to prepare $BiVO_4$ samples with a broad range of crystallite sized ranging from 25.82 nm to 111.56 nm. The impact of this parameter on the photocatalytic performance will be discussed in chapter 3.4.

$$\tau = \frac{K\lambda}{\beta cos\Theta} \tag{9}$$

In order to obtain the 3 values for one sample shown in table 11 the full width at half maximum of the peaks at approximately 28, 31 and 42 2 Θ were obtained.

Table 11: Crystallite size obtained by the Scherrer equation by taking the full width at half maximum value for the peaks at 28, 31 and 42 2 Θ

Sample number	**02**	**02 oven**	**03**	**04**	**05**	**07**	**08**	**09**	**10**
Crystallite size [nm]	57.1	57	91.3	114.2	91.4	35.1	65.2	23.9	65.2
	57.9	57.9	76.1	190.3	95.1	77.3	58.9	77.3	77.3
	67.7	55.5	148.1	111.2	148.2	40.3	135.4	147.2	111
Average [nm]	60.9	56.8	105.6	138	111.56	40.23	86.5	82.8	84.5

Additionally, samples in the pH range of -0.032-0.45 were prepared, and their X-ray powder diffractograms are shown in figure 16. According to the X-ray powder diffractogram of the sample which was prepared at the pH value of -0.032 resulted in a mixture of scheelite tetragonal and zircon tetragonal, because both peaks which are characteristic for zircon tetragonal and scheelite tetragonal phase are visible. Furthermore, there are no splitting peaks visible, which is an indication for the presence of scheelite tetragonal $BiVO_4$. The sample, which was prepared at the pH of 0.011 resulted in pure zircon tetragonal phase according to the XRD, because the diffraction positions match with the reference peak positions of tetragonal $BiVO_4$. The samples, at the pHs of 0.08-0.45 all resulted in pure monoclinic $BiVO_4$. The average crystallite sizes of these samples were around 25 nm, which is relatively small compared to the crystallite size of the samples which were prepared at the pH of 0.88-1.45.

Overall it can be said, according to figure 16 and figure 15, that the pH range of 0.08-1.45 leads to pure phased monoclinic $BiVO_4$, assuming that the XRD results from the semiconductors prepared at the pH of 1.076 are an outlier. Additionally, the crystallite sizes of the sample with the number 74-78 were calculated via the Scherrer-equation (equation 9) and the results are shown in table 12. The samples prepared in the pH range of -0.032-0.45 are having small single crystalline regions compared to the samples prepared at the pH range of 0.88-1.4. The expected catalytic activity should also be lower for the semiconductors with smaller crystalline regions, because as the area of crystalline regions decreases, the number of defects in the crystal increases, thus meaning that there is a higher probability for the recombination of the photo-induced charge carriers.

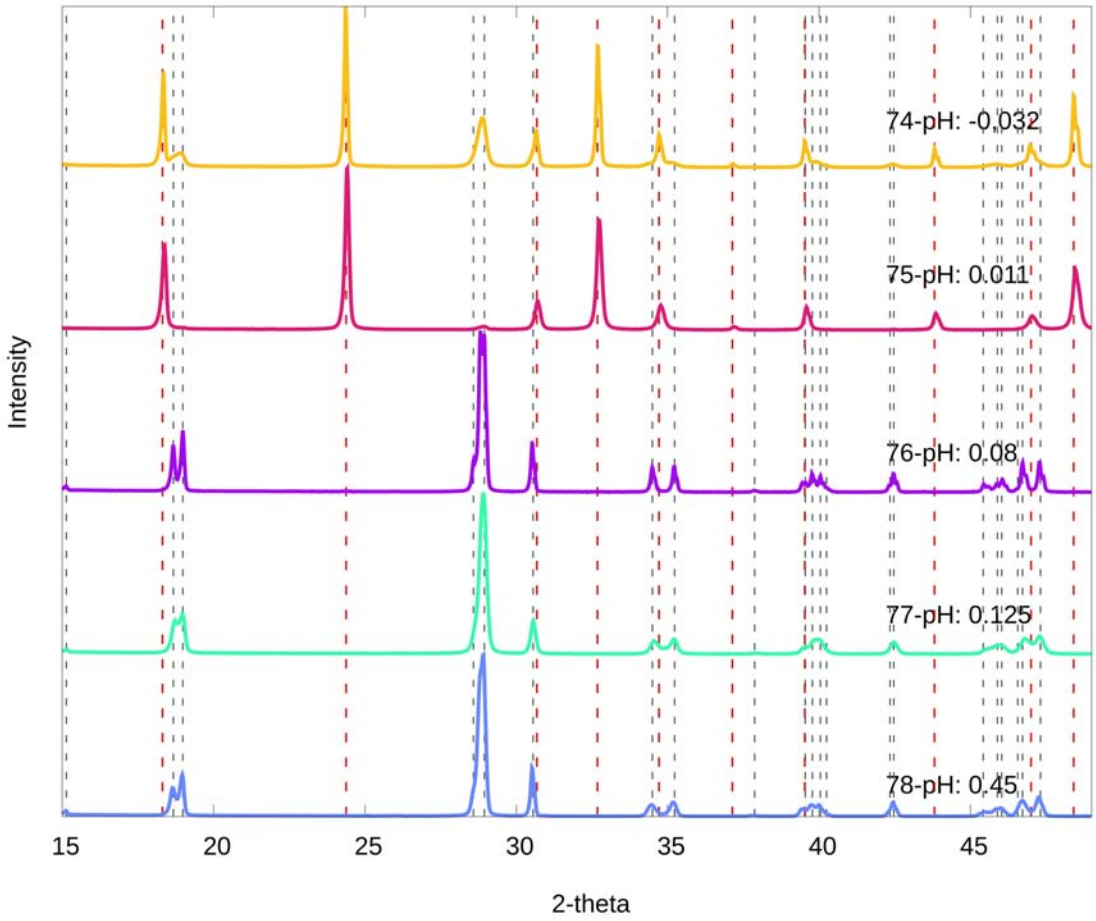

Figure 16: X-ray powder diffractogram of $BiVO_4$ samples, which were prepared by a pH dependent synthesis with constant irradiation temperature of 200 °C and irradiation time of 40 min. The diffractogramms have the following notation: sample number-pH value. The black dashed line represents the reference peak positions of m$BiVO_4$ and the red dashed line represents t-z $BiVO_4$

Table 12: Crystallite size calculated by the Scherrer equation using the highest intensity peak

Sample number	**74**	**75**	**76**	**77**	**78**
Crystallite size [nm]	25.85	25.82	25.84	25.83	25.85

3.1.4 UV-Vis Diffuse reflectance spectroscopy

The UV-Vis diffuse reflectance spectra (DRS) of the samples with the number 02-10 is shown in figure 17 a). In figure 17 b) a reference DRS spectra is shown which was taken from the paper of Tan et al.[118]. In figure 17 a) is shown, that the samples with the number 02-05, 08 and 10 show absorption in the region of 400-500 nm. All materials are showing strong absorption in the visible light region, which proves a visible light active photocatalytic reaction is possible. The electron transition hybrid Bi 6s - O 2p valence band to V 3d conduction band is responsible for the good absorption characteristics of $BiVO_4$ in the visible region until approximately 520 nm.[88] According to section 3.1.3 the samples prepared at the pH value of 1.076 resulted in a mixed phase between

t-s $BiVO_4$ and t-z $BiVO_4$. As reported in previous reports, the crystalline phase change leads to an electronic structure change.[118,140,141]. The visible-light absorption band with an absorption edge of 430 nm for tetragonal $BiVO_4$ is assigned to the electron transition from an O_{2p} valence band to a V_{3d} conduction band, while the valence bands at the top of the monoclinic $BiVO_4$ may be formed by both O_{2p} (64%) and Bi_{6s} (18%), namely, a hybrid orbital of Bi_{6s} and O_{2p} ($Bi_{6s\text{-}O2p}$).[59,142,143] These findings explain, why the absorption curve of the samples 06, 07 and 09 show a step like absorption in the region of 420-500 nm.

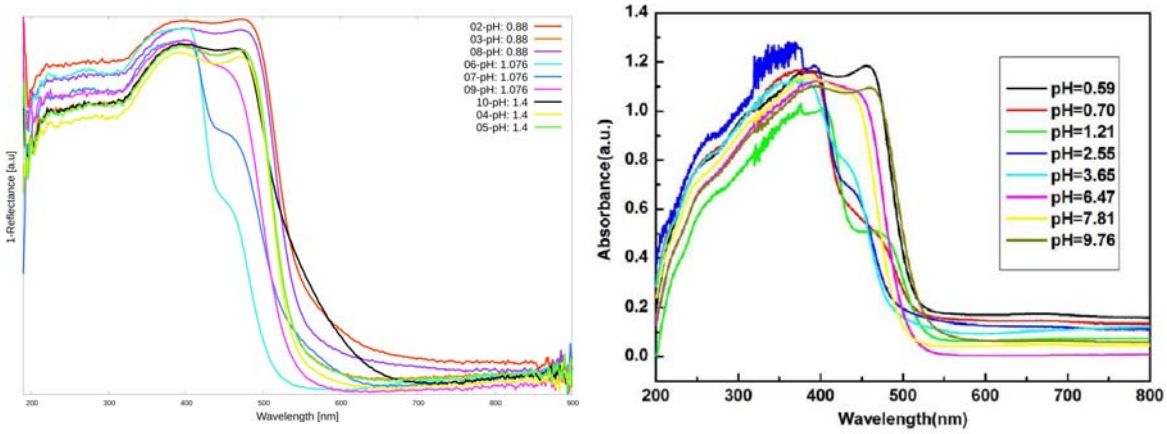

(a) (b)

Figure 17: a) Diffuse reflectance spectra of $BiVO_4$, which were obtained by varying the pH value during synthesis and keeping the irradiation time and temperature constant(200 °, 40 min). The spectra has the following notation: Sample number-pH value, b) Reference diffuse reflectance spectra of $BiVO_4$ [118]

The band gaps estimated, based on the relationship between absorbance and photon energy, by extrapolating the linear region of the Tauc-plot whereat the absorbance multiplied by the energy squared is plotted against the energy as seen in figure 18. The established values are shown in table 13. The samples which were prepared at the pH value of 1.076 resulted in a composite. The samples prepared at the pH value of 0.88 and 1.4 have only one calculated band gap which is about 2.39 eV. These samples were evaluated as monoclinic phase in section 3.1.3 according to their XRD diffractograms. The zircon tetragonal phase has a reported band gap of 2.8 eV, which was evaluated for the samples 06, 07 and 09. These samples resulted in a mixed phase, according to their XRD diffractogram shown in section 3.1.3. Conclusively, the XRD results are in high correlation with the DRS results. The photocatalytic activity at visible light is expected to be higher for the samples which have a calculated band gap of 2.39 eV than for the samples, which resulted in tetragonal phase, because semiconductors with a band gap value around 2.8 eV absorb UV light more effectively.

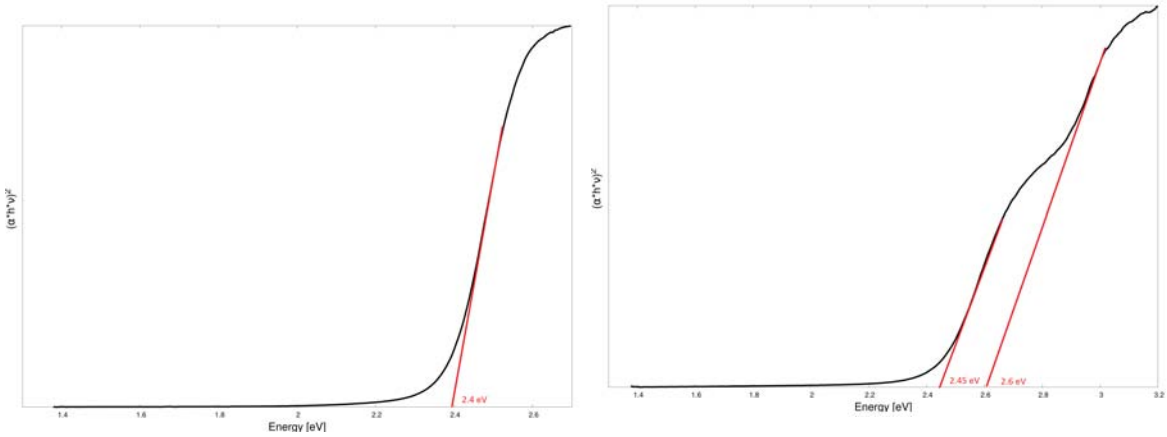

(a) monoclinic $BiVO_4$

(b) mixed phase of monoclinic and zircon tetragonal $BiVO_4$

Figure 18: Tauc-plot obtained from the diffuse reflectance spectra of two different $BiVO_4$ samples, which were obtained by varying the pH value during the synthesis

Table 13: Band gaps of the $BiVO_4$ samples estimated by the Tauc method

Sample number	**02**	**03**	**04**	**05**	**06**	**07**	**08**	**09**	**10**
band gap [eV]	2.38	2.39	2.39	2.39	2.48 2.86	2.4 2.8	2.38	2.44 2.53	2.38

The crystalline samples with the number 74-78 were prepared at lower pH, namely -0.032-0.45, and their UV-Vis diffuse reflectance spectra (DRS) are shown in figure 19. In figure 19 a) is shown, that the samples with the number 76-78, have and absorption behaviour between 400 and 500 nm, which is characteristic for monoclinic $BiVO_4$. According to XRD results of the same samples presented in section 3.1.3 the samples 74 and 75 resulted in a mixed phase between $mBiVO_4$ and $tBiVO_4$ and their absorption graph show a step like absorption in the region of 420-500 nm. The band gaps of the samples 74-78 were estimated via the Tauc plot of the diffuse reflectance spectra, and are shown in table 14. The DRS results are in high correlation with the XRD results of the samples 74-78 presented in section 3.1.3. The expected visible light photocatalytic activity for sample 76-78 is higher, than for the samples 74 and 75, because sample 74 and 75 resulted in either mixed phase or only tetragonal phase $BiVO_4$. Mixed phase or only tetragonal $BiVO_4$ have a wider band gap compared to only monoclinic $BiVO_4$ therefore they visible light absorbtion is weaker, than the absorption of pure phased monoclinic samples.

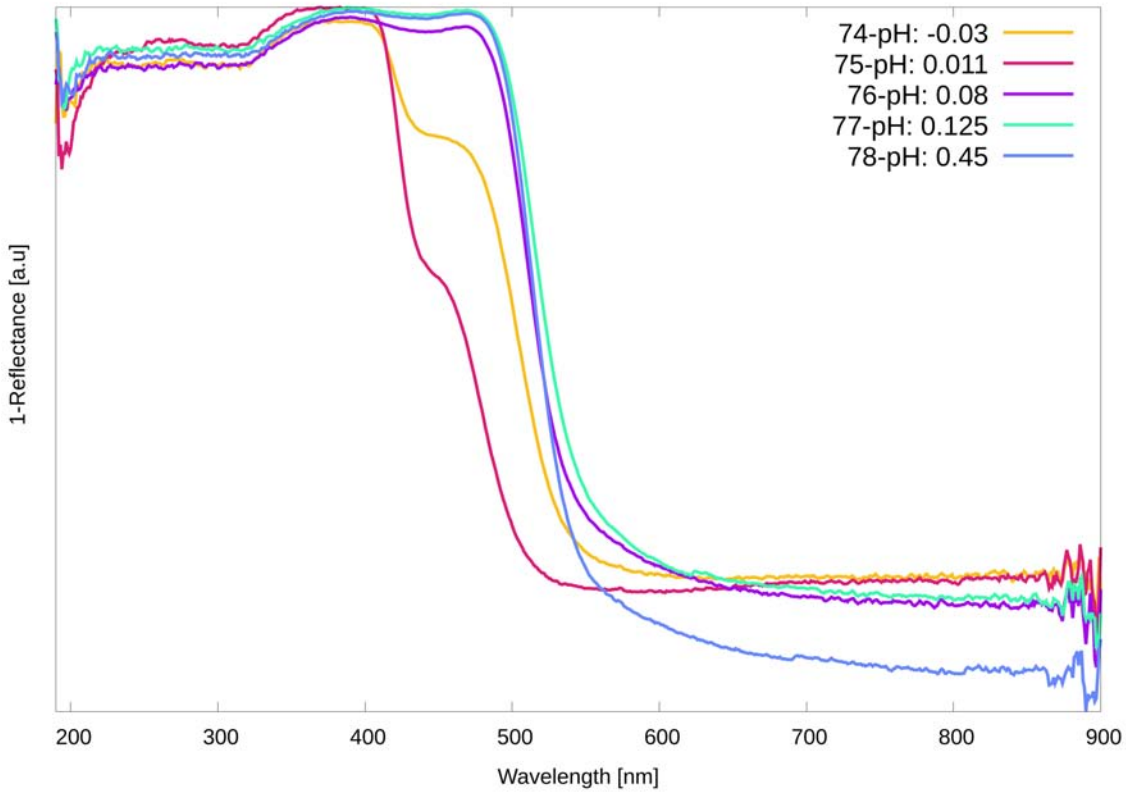

Figure 19: Diffuse reflectance spectra of $BiVO_4$, which were obtained by varying the pH value during synthesis and keeping the irradiation time and temperature constant(200 °C, 40min). The spectra has the following notation: Sample number-pH value

Table 14: Band gaps of the $BiVO_4$ samples estimated by the Tauc method

Sample number	**74**	**75**	**76**	**77**	**78**
band gap [eV]	2.41	2.52	2.41	2.39	2.40
	2.79	2.88			

3.1.5 Summary

The table 15 summarizes the results of the pH dependent synthesis of $BiVO_4$, whereat morphology of the particles, polymorph, crystallite size, band gap, and OER activity are shown dependent on the pH value during preparation. Too low pH values, namely -0.03 and 0.01 lead to either mixed phase or tetragonal phase. The samples prepared at higher pH value, resulted in monoclinic phase, besides the sample prepared at the pH of 1.076. The SEM investigation of the monoclinic phase reveals, that the morphology is either capped octahedron, polyhedron or a cluster of smaller polyhedra. The samples which resulted in tetragonal phase, show sphere like particles, which are either dense or consists of smaller particles. The mixed phase samples resulted in both of the morphologies, which are characteristic for monoclinic and tetragonal phase. As shown later in section 3.4 the OER activity is dependent on the established band gap value. It was tried to understand if the pH value during the preparation of the catalyst has any influence on the band gap. The band gap was plotted against the

band gap value and is shown in figure 20. It is visible, that lower pH values lead to higher band gap values, although, only a weak correlation between the parameters could be established.

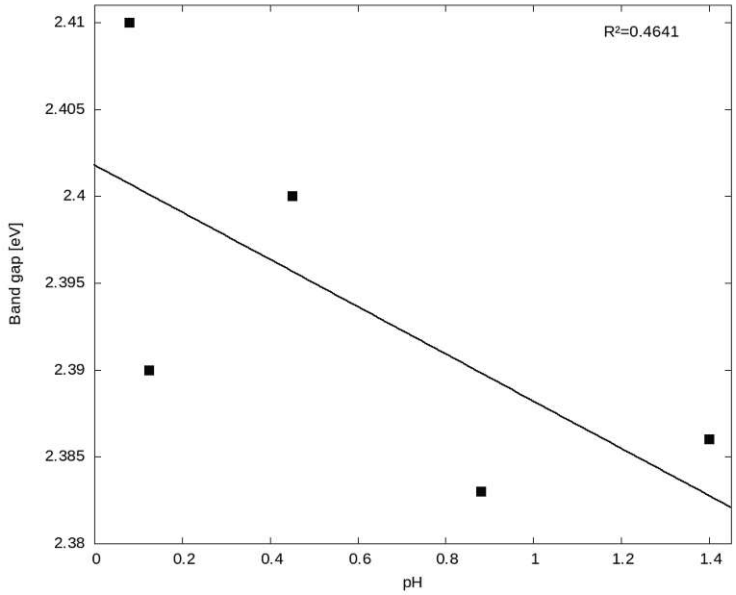

Figure 20: Band gap value of monoclinic $BiVO_4$ determined with the Tauc-plot and plotted against the pH value during preparation

Table 15: Summary of the results discussed in section 3.1

pH	Sample number	Morphology	Size [µm]	Polymorph	Crystallite size [nm]	Band gap [eV]	Oxygen evolution activity [µmol/h]
-0.03	74	sphere like, which consists of smaller crystals + octahedron	4	t-s + t-z	25.85	2.41; 2.79	0.058
0.011	75	sphere like, which consists of smaller crystals	2	t-z	25.82	2.52; 2.79	0.039
0.08	76	capped octahedron like flat crystals with cut edges	2	m	25.84	2.41	0.827
0.125	77	cluster of small polyhedrons	6-10	m	25.83	2.39	0.367
0.45	78	capped octahedron of which a small area of 010 facet is exposed	2	m	25.85	2.4	0.746
0.88	02	octahedron	2-3	m	57	2.38	0.31
0.88	03	capped octahedron with exposed 010 facet	2-3	m	91	2.39	0.259
0.88	08	lose spheres which consists of smaller crystals + polyhedron + irregular shaped particles	2-3	m	65	2.38	0.042
1.076	06					2.48; 2.86	0.048
1.076	07	lose spheres which consists of smaller crystals + polyhedron	2	m + t-z	35	2.4; 2.8	0.048
1.076	09	-	-	t-s + t-z	23.9	2.44; 2.53	0.135
1.4	04	capped octahedron with exposed 040 facet	2-3	m	114	2.39	0.436
1.4	05	capped octahedron with exposed 040 facet + polyhedron	2-3	m	91	2.39	0.229
1.4	10	irregular shaped particles	1	m	65	2.38	0.305

3.2 Time dependent synthesis

The synthesis of $BiVO_4$ was tried out without microwave irradiation and with different times of microwave irradiation, in order to understand the formation mechanism of $BiVO_4$. Zhang et al.[121] prepared monoclinic and zircon tetragonal $BiVO_4$ by controlling the microwave irradiation time, whereat at prolonged microwave irradiation the tetragonal phase transferred into monoclinic phase

gradually. According to the results published in the paper of Zhang et al. pure monoclinic phase is expected to form after 12 minutes of microwave irradiation time. The synthesis details are shown in the section 2.4.3. For monitoring the formation mechanism, the irradiation times 10 s, 20 s, 30 s, 1 min, 1.5 min, 2 min, 4 min, 6 min, 8 min, 10 min, 20 min and 60 min were tried out. In the following section the appearance, SEM, XRD and DRS results of monoclinic $BiVO_4$ are presented and discussed. The results of all products of the time dependent synthesis are shown in the appendix.

3.2.1 Appearance

The figure 21 a) shows the appearance of the $BiVO_4$, which was prepared without microwave irradiation, and is resulted in an orange powder. Based on the color of the product shown in figure 21 a), it is assumed, that the band gap value of this product is smaller than for the vivid yellow colored product shown in figure 21 b), in order to identify this product, in the present section XRD and DRS are utilized. The vivid yellow color can be an indication, that the sample shown in figure 21 b) resulted in monoclinic $BiVO_4$, because the electronic transition from the O 2p/Bi 6s hybrid orbital to the V 3d conduction band corresponds to this color.[59] Further analysis (XRD and DRS) of the products exhibiting a vivid yellow color are shown in this section.

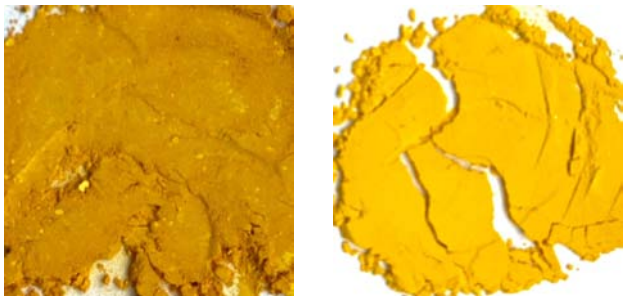

(a) $BiVO_4$ powder without microwave irradiation (b) $BiVO_4$ powder with microwave irradiation

Figure 21: $BiVO_4$ powder prepared without microwave irradiation and monoclinic $BiVO_4$ powder

3.2.2 Scanning electron microscopy

Figure 22 gives an overview of the morphologies of the samples which were prepared at different irradiation times. The synthesis of $BiVO_4$ was carried out without microwave irradiation as a reference. The image shows irregular shaped particles in the nm range, which highlights the importance of the MW synthesis that results in the formation of larger crystals and more defined morphologies. From figure 22 it is visible, that already 2 minutes of microwave irradiation lead to well defined octahedral morphology. At 60 minutes of microwave irradiation it seems like, that high-indexed facets are exposed as well. Overall, besides of the observations listed above, there was no correlation between the irradiation time and the obtained morphology. Another synthesis was carried out, whereat small amounts of the semiconductor was taken from the same microwave vial at 10 s, 20 s, 30 s, 1 min, 1.5 min, 2 min, 4 min, 6 min, 8 min and 10 min of microwave irradiation. The SEM images of the as-synthesised samples are shown in figure 23. From figure 23 it is visible, that polyhedron shaped crystals are already formed at 10 seconds of microwave irradiation. However, no connection is apparent between the irradiation time and morphology. It can be proposed that the generation of larger $BiVO_4$ crystals requires very short MW times, down to seconds, However, only those particles that

grow to a certain "critical" size maintain it after MW irradiation is stopped. The rest of the particles that have not yet reached a certain dimension undergo dissolution and appear to be similar to the starting mixture (figure 22 a)). The irregularity of the morphologies obtained after different time of MW irradiation (figure 22) can be related to the high sensitivity of the synthesis to various parameters, such as the preparation of the solution and the ratio of Bi and V precursors.

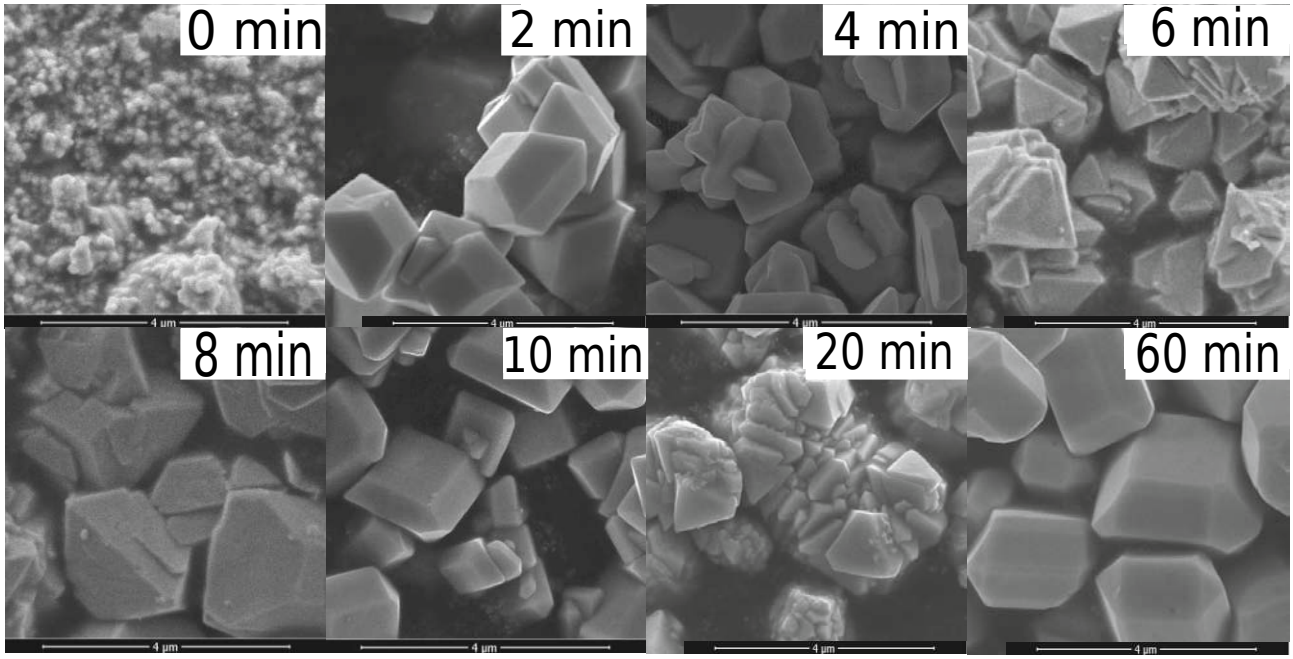

Figure 22: SEM images of some samples which were prepared by varying the irradiation time during preparation

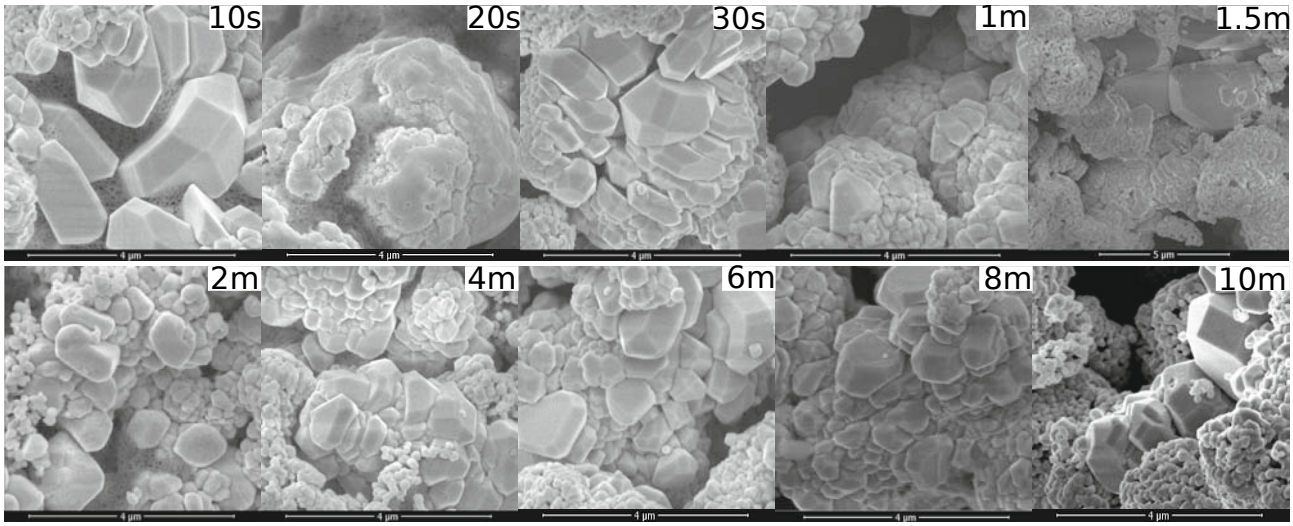

Figure 23: SEM images of the in-situ time dependent synthesis

3.2.3 X-ray powder diffraction

The synthesis of $BiVO_4$ with different microwave irradiation times was tried out. Their X-ray powder diffractogram is shown in figure 24. The X-ray diffractogram of the sample which were prepared without microwave irradiation time is shown in figure 24 a), and is labeled with the sample number 70. The sample resulted in mostly zircon tetragonal $BiVO_4$, however one peak at approximately 28 2 Θ is visible, which is characteristic for the monoclinic $BiVO_4$. According to Zhang et al., a mixed phase of monoclinic and tetragonal $BiVO_4$ should be formed at very short microwave irradiation times, namely below 12 min, yet in this work the synthesis of single-phase monoclinic $BiVO_4$ was successful even at 2 min.[121] As it is known, that monoclinic $BiVO_4$ exhibits the best photocatalytic activity among all the polymorphs[88,136], it is expected, that the samples obtained in the time dependent synthesis show excellent oxygen evolution activity.

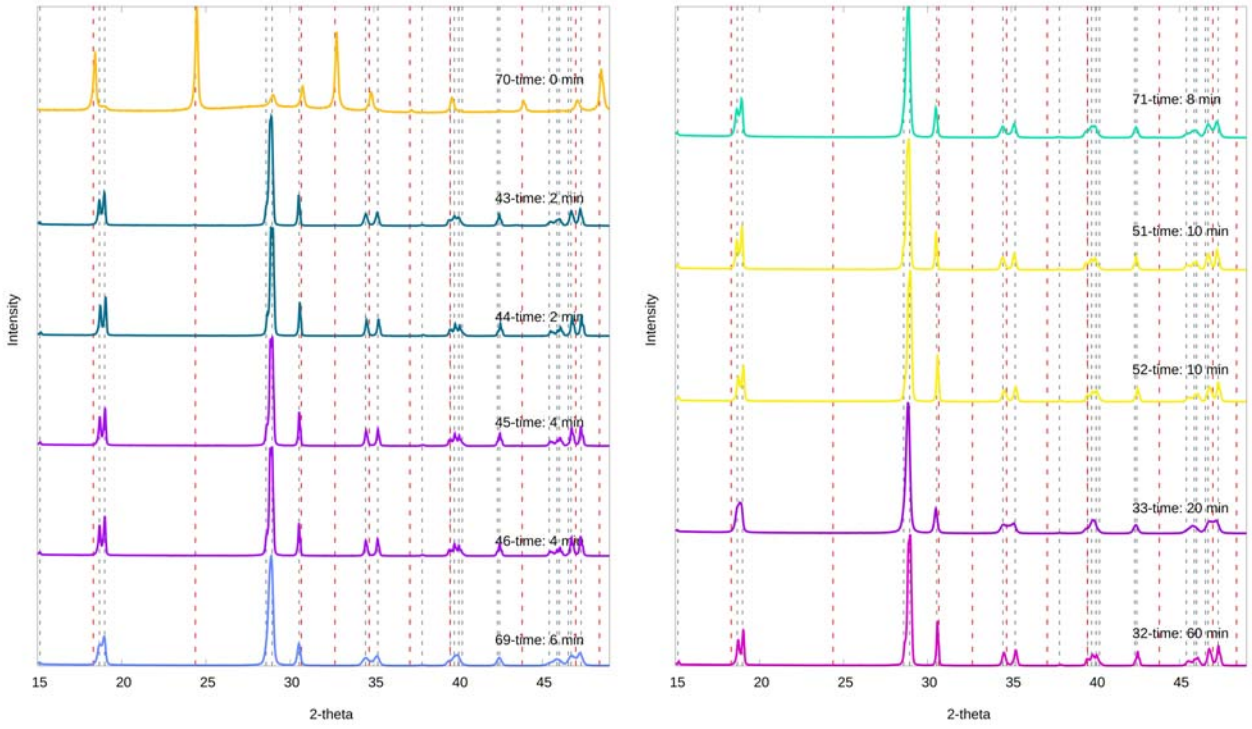

(a) (b)

Figure 24: X-ray powder diffractogram of $BiVO_4$ samples, which were prepared by a time dependent synthesis with constant irradiation temperature of 200 °C and pH of 0.88 during preparation. The diffractograms have the following notation: sample number-irradiation time. The black dashed line represents the peak positions in the reference X-ray diffractogram of the monoclinic $BiVO_4$, whereat the red dashed line represents the reference of tetragonal $BiVO_4$

3.2.4 UV-Vis Diffuse reflectance spectroscopy

Different microwave irradiation times were tried out for the synthesis of $BiVO_4$, such as 2, 4, 6, 8, 10, 20 and 60 minutes. The UV-Vis diffuse reflectance spectra of the samples which were synthesised at 2, 4, 6, 8, 10, 20 and 60 minutes are shown in figure 25. In the spectrum of the sample 70, which was made by only precipitating the precursors without microwave irradiation, is not a sharp absorption observed like it is visible in the spectra of the other samples. According to the X-ray

powder diffractogram of sample 70 shown in section 3.2.3, this sample resulted in a mixed phase between monoclinic and tetragonal $BiVO_4$. All the other samples where microwave irradiation was used for the synthesis, the diffuse reflectance spectra shows a steep absorption between 400 nm and 500 nm. This is in good agreement with X-ray powder diffractogram results, hence these samples resulted in pure monoclinic phase according to their XRD diffractograms shown in section 3.2.3.

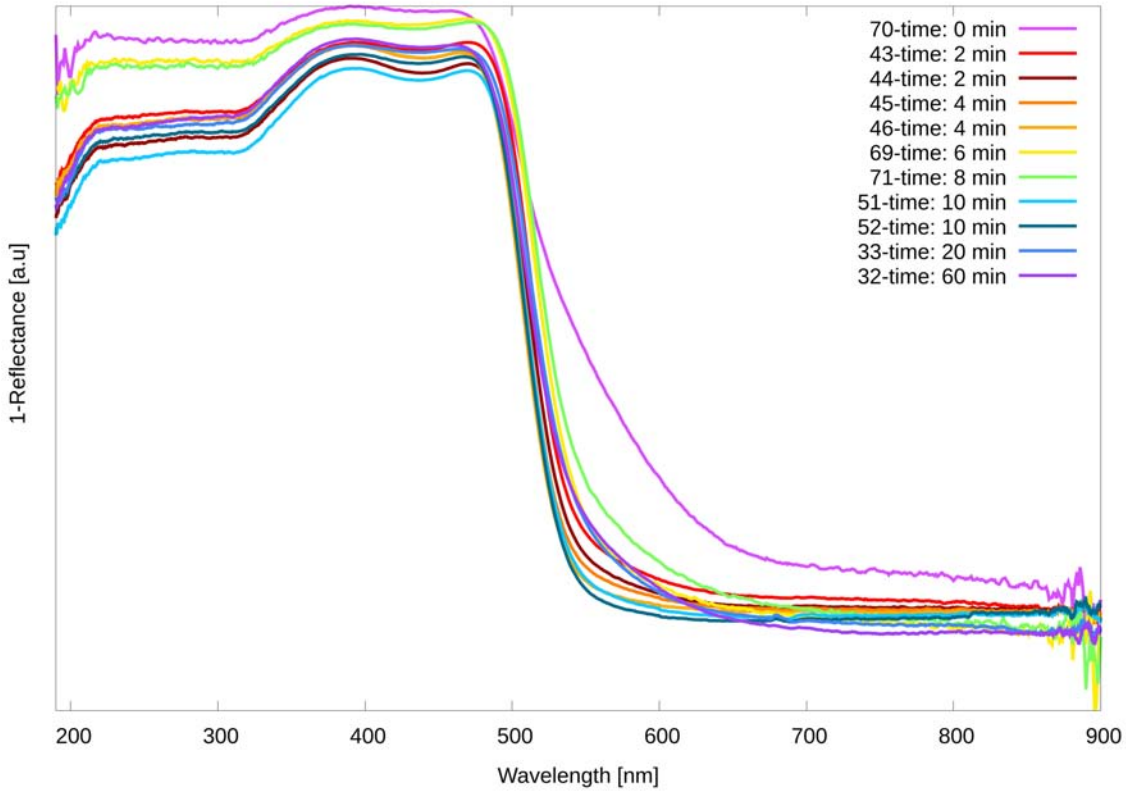

Figure 25: Diffuse reflectance spectra of $BiVO_4$, which were obtained by varying the microwave irradiation time during synthesis and keeping the temperature and pH value constant(200 °C, pH 0.88). The spectra has the following notation: Sample number-irradiation time

The band gaps estimated, based on the relationship between absorbance and photon energy, by extrapolating the linear region of the Tauc-plot whereat the absorbance multiplied by the energy squared is plotted against the energy. The established values are shown in table 16 and table 17. The sample 70 was prepared without microwave irradiation, and resulted in an orange powder. This sample possess a calculated band gap of 2.37 eV. The other samples, which were prepared at variable microwave irradiation time resulted in monoclinic phase, and their calculated band gap is around 2.4 eV.

Table 16: Estimated band gaps of $BiVO_4$

Sample number	**70**	**43**	**44**	**45**	**46**	**69**
band gap [eV]	2.37	2.4	2.4	2.42	2.43	2.39

Table 17: Estimated band gaps of $BiVO_4$

Sample number	**71**	**51**	**52**	**33**	**32**
band gap [eV]	2.38	2.4	2.42	2.38	2.39

As shown later in section 3.4 the band gap value is in linear correlation with the OER activity. It was tried to understand, if the irradiation time of the samples during preparation has an impact on the band gap value. On figure 26 the band gap value is plotted against the microwave irradiation time. It is visible, that 6 minutes of microwave irradiation leads to the highest band gap value. A microwave irradiation time above 20 minutes leads to narrow band gap values, although, only a weak correlation between the parameters could be established.

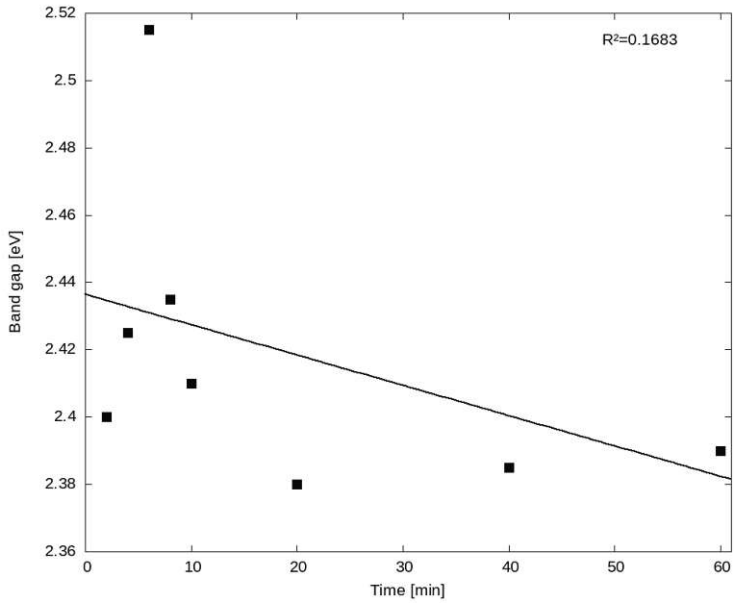

Figure 26: Band gap value of monoclinic $BiVO_4$ determined with the Tauc-plot and plotted against the irradiation time during preparation

3.2.5 Summary

The table 18 summarizes the results of the time dependent synthesis of $BiVO_4$, whereat morphology of the particles, polymorph, crystallite size, band gap, and OER activity are shown dependent on the microwave irradiation time during preparation. There was a sample prepared without microwave irradiation, which resulted in mixed phase of monoclinic and tetragonal $BiVO_4$ and its SEM results reveal irregular shaped particles which are in the nanorange. As described already in section 3.1.5, typical morphologies for the monoclinic phase are capped octahedron, polyhedron and cluster of smaller polyhedra. The tetragonal phase characteristically shows sphere like particles, which are either dense or consists of smaller particles. The synthesis under different microwave irradiation times was performed to observe the formation of the morphologies of the $BiVO_4$ materials. No trend was observed between irradiation time and morphology, but it can be assumed that the generation of larger crystals requires very short microwave irradiation times, namely seconds. It is assumed that the crystals that have not reached a certain stability dissolve again and look similar to the morphology of

the precipitate. Besides the microwave irradiation time, other aspects have a great influence on the morphology, such as the mixing of the starting products and the ratio of these.

Table 18: Summary of the results discussed in section 3.2 for the samples for which different microwave irradiation times were tried out

Time [min]	Sample number	Morphology	Size [µm]	Polymorph	Crystallite size [nm]	Band gap [eV]	Oxygen evolution activity [µmol/h]
0	70	irregular shaped particles + clusters of particles	particles: few nm; clusters: 2 nm	t-s + t-z	25.84	2.37	0.53
2	43	capped octahedron with exposed 040 facets	2	m	62.93	2.4	0.817
2	44	capped octahedron with exposed 040 facets	3-4	m	125.93	2.4	1.638
4	45	flat crystals with cut edges + polyhedron	2	m	65.87	2.42	1.507
4	46	capped octahedron + cluster of smaller particles	2	m	94.41	2.43	0.9
6	69	cluster of octahedron	2	m	25.84	2.39	
8	50	capped octahedron + cluster of smaller particles	3-4	m	65.85	2.39	0.753
8	71	cluster octahedron	2	m	25.86	2.38	
10	51	capped octahedron with exposed 040 facets	2	m	57.64	2.4	0.929
10	52	capped octahedron + irregular shaped particles	1-2	m	25.21	2.42	1.645
20	33	cluster of octahedron	4	m	29.45	2.38	0.213
60	32	octahedron + polyhedron	3-4	m	48.32	2.39	0.65

3.3 Solvent and surfactant variation

Synthesis with different amounts of ethanol as a solvent instead of water were tried out, in addition samples were made with CTAB and SDBS as surfactant. The synthesis were carried out in order to control facet growth. According to the results of Rodrigues et al.[126] it was expected, that the use of ethanol as a solvent leads to the formation of 2D morphology, and the use of surfactants leads to the formation of smaller particles. The exact synthesis details are described in section 2.4.4. The synthesis with 1%, 5%, 25%, 50%, 75% and 100% ethanol and the addition of CTAB and SDBS. In the following the appearance, SEM, XRD and DRS results of the samples, which were prepared at variable amounts of ethanol as a solvent and the addition of surfactants during the synthesis.

3.3.1 Appearance

Figure 27 shows the samples which were prepared with the addition of different amounts of ethanol during preparation. The sample with 1% of ethanol is shown in figure 27 a) and it resulted in a bright yellow powder which is characteristic for the monoclinic $BiVO_4$ phase. The appearance of the samples with higher amounts of ethanol are shown in figure 27 b)-d), they resulted in green powder. It can be assumed, that the green colored samples have a bigger band gap than the yellow colored monoclinic $BiVO_4$ samples, thus it is also assumed, that the samples, which possess green color are not monoclinic $BiVO_4$.

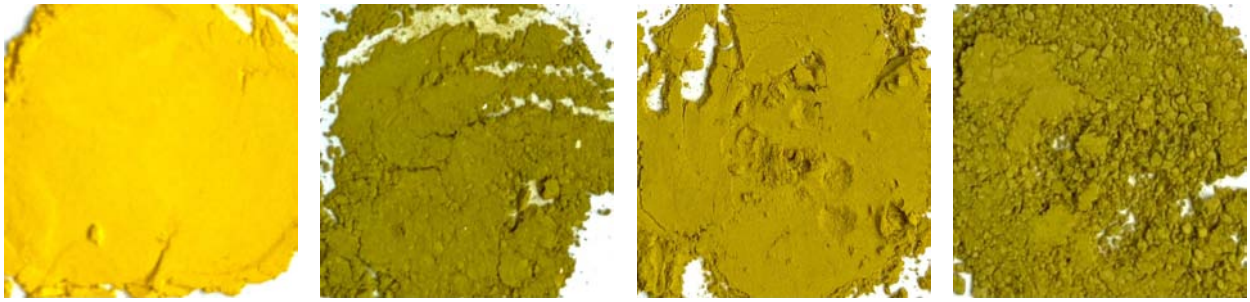

(a) 1% Ethanol (b) 25% Ethanol (c) 50% Ethanol (d) 75%Ethanol

Figure 27: Appearance of some samples, which were prepared with variable amount of ethanol as a solvent

3.3.2 Scanning electron microscopy

Figure 28 shows the morphologies of the semiconductors which were synthesised with different amounts of ethanol as well as different surfactants. Solvent-dependent synthesis of $BiVO_4$ resulted in a variety of morphologies. Only the product synthesized with the addition of 1% ethanol to the reaction mixture has a similar morphology to the products identified as monoclinic $BiVO_4$ in the previous chapters. All other products discussed in this chapter have acicular or plate-like morphology. The detailed description of the morphologies of the individual products are visible in table 3.3.5. The synthesis of the $BiVO_4$ with variable amount of ethanol as a solvent was carried out in order to control facet growth. A 2D morphology was expected in the presence of ethanol, which was only achieved for the sample with 75% added ethanol. The other samples resulted in acicular morphology or layered morphology. There was no discernible trend between ethanol addition and morphology.

The synthesis of $BiVO_4$ was carried out with the addition of SDBS and CTAB as a surfactant, of which the synthesis details are described in the section 2.4.5. The sample 67, was prepared by the addition of SDBS, whereat sample 68 was prepared by the addition of CTAB to the reaction mixture. Both of the samples shows a sphere like cluster consisting of smaller particles. The addition of surfactants to the reaction mixture should result in a reduction in the size of crystalline products.[126] However, no correlation between the use of surfactants and size was detected.

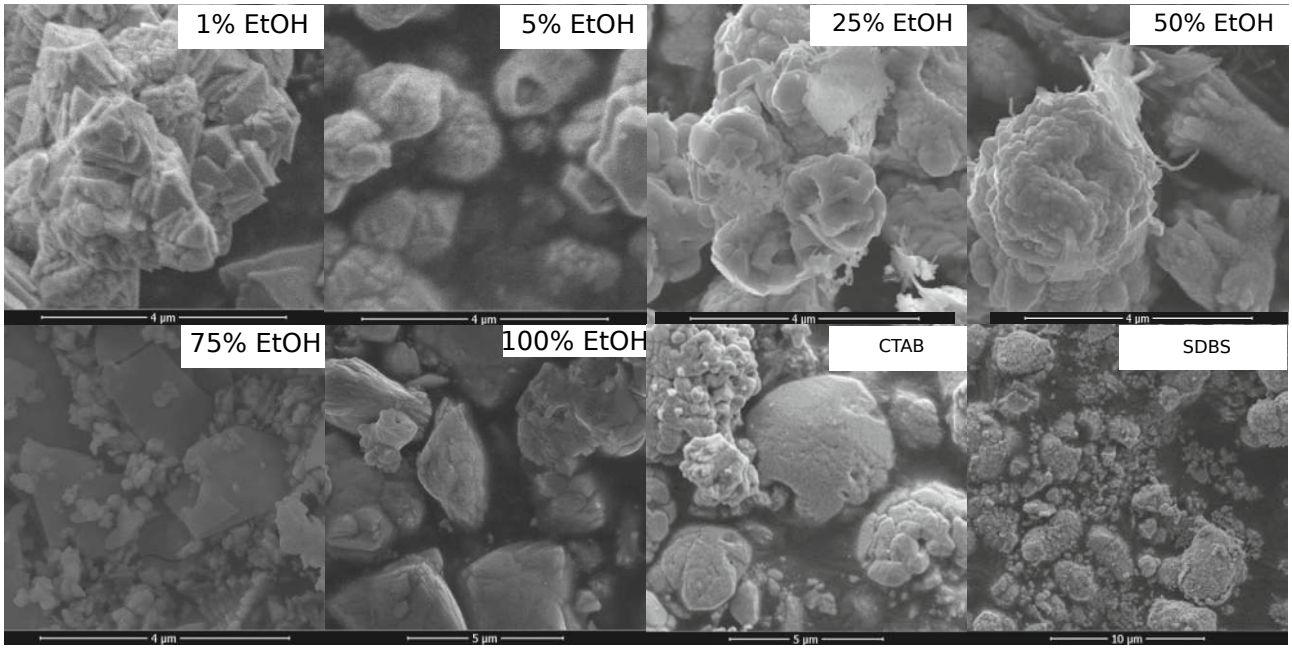

Figure 28: SEM images of some samples, which were prepared by the variation of ethanol amounts during the synthesis, as well as different surfactants

3.3.3 X-ray powder diffraction

The X-ray diffractograms of the samples with 1%, 5%, 25%, 50%, 70% ethanol and only ethanol as solvent are shown in figure 29. One characteristic peak for zircon tetragonal $BiVO_4$ is at 24 2 Θ, which is observed in the XRD of sample number 72, 73, 35, 41 and 37. The splitting peaks at 18.5 2 Θ, 35 2 Θ and 46 2 Θ exists in the monoclinic structure, but not in the scheelite tetragonal structure. The splitting of the peaks is only slightly visible for sample 72. The sample 72 was prepared by addition of 1% ethanol to the reaction mixture, during synthesis, and according to the XRD it resulted in a mixture of zircon tetragonal and scheelite monoclinic phase, because its XRD shows the characteristic peak for zircon tetragonal $BiVO_4$ at 24 2 Θ and it shows the splitting peaks, which are characteristic for the monoclinic phase, namely at 18.5 2 Θ, 35 2 Θ and 46 2 Θ. Furthermore, the products synthesized with the addition of 25% ethanol resulted in t-s $BiVO_4$. All other products are a composite of t-s and t-z $BiVO_4$. On the diffractogram of sample 42 shown in figure 29 a small peak at approximately 22 2Θ and 32 2Θ is visible, and were identified with the Highscore XRD analysis software. The peaks at 22 2Θ and 32 2Θ could originate from pure Bi[144], NH_4NO_3[145] or $Bi_{12.03}O_{20.27}V_{0.89}$[146]. The summary of the phases associated with each product are shown in table 3.3.5. In summary, almost all the samples, which were prepared with the addition of ethanol resulted in mixed phase between monoclinic and zircon tetragonal or scheelite tetragonal and monoclinic phase. The calculated crystallite size values of the samples, which are shown in table 19 are relatively small. Both the monoclinic phase and low crystallinity are expected to have a negative impact on catalytic activity. The oxygen evolution activities of the products are discussed in section 3.4.

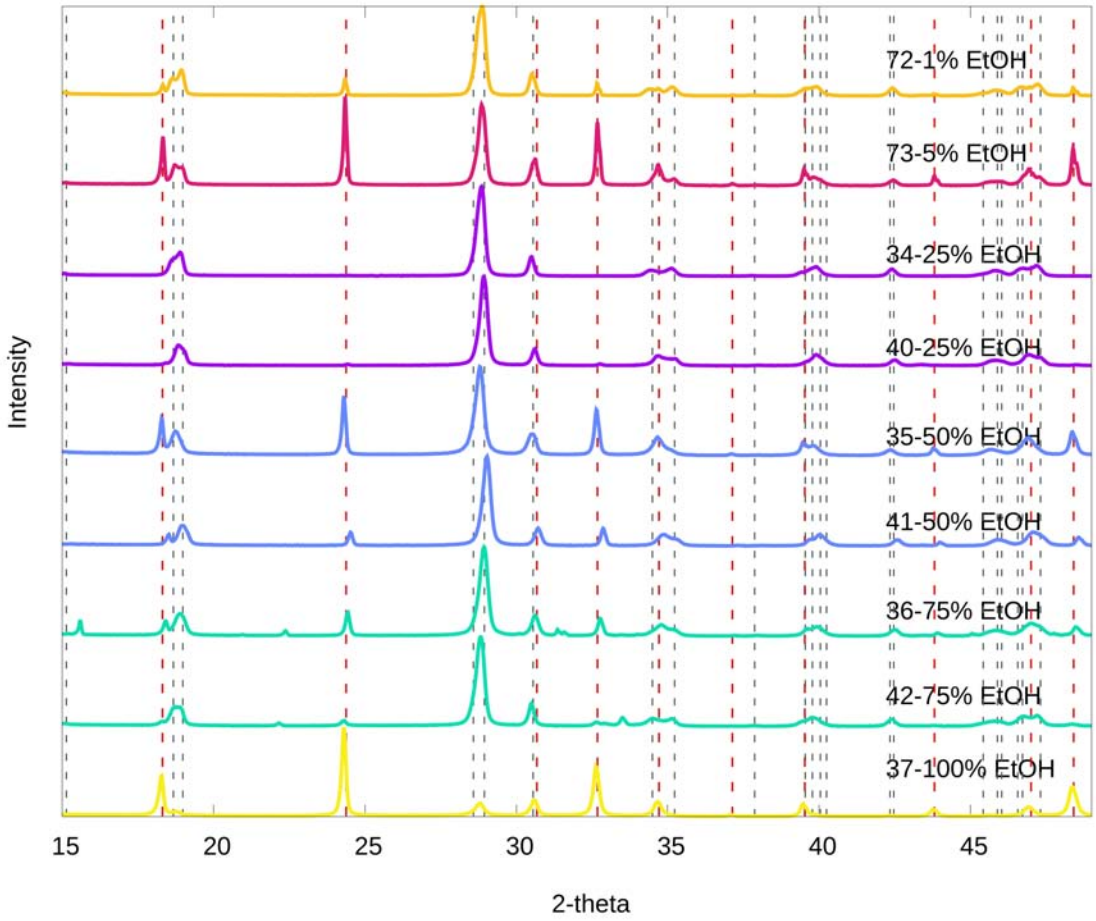

Figure 29: X-ray powder diffractogram of $BiVO_4$ samples, which were prepared by a solvent dependent synthesis with constant irradiation temperature of 200 °C, pH of 0.88 and irradiation time of 40 min during preparation. The diffractograms have the following notation: sample number-amount of ethanol. The black dashed line represents the peak positions in the reference X-ray diffractogram of the monoclinic $BiVO_4$, whereat the red dashed line represents the reference of tetragonal $BiVO_4$

Table 19: Crystallite sizes calculated by the Sherrer equation using the highest intensity peak respectively

Sample number-EtOH amount	72-**0.01**	73-**0.05**	34-**0.25**	40-**0.25**	35-**0.5**	41-**0.5**	36-**0.75**	42-**0.75**	37-**1**
Crystallite size [nm]	25.86	25.93	20.79	29.44	27.21	25.21	25.24	25.25	25.54

The XRD results of the samples, which were prepared with SDBS and CTAB as surfactant are shown in figure 30. According to the XRD of sample 67, which was prepared with SDBS the peak positions are the same as marked for the monoclinic $BiVO_4$ sample, but the splitting peaks at 18.5 2Θ, 35 2Θ and 46 2Θ, which are characteristic for monoclinc $BiVO_4$ are not visible. It is assumed, that sample 67 resulted in scheelite tetragonal $BiVO_4$. On the XRD of the sample 68 a highly pronounced peak is visible at 24 2Θ which is an indication for zircon tetragonal $BiVO_4$, additionally peaks are visible at the characteristic peak positions, which are marked for the monoclinic $BiVO_4$. However, the splitting peaks which are characteristic for monoclinic are not visible, thus it can be concluded,

that the sample, with the number 68 resulted in a mixture of zircon tetragonal and scheelite tetragonal $BiVO_4$. Because of their polymorph nature, for both samples, the expected oxygen evolution activity is low.

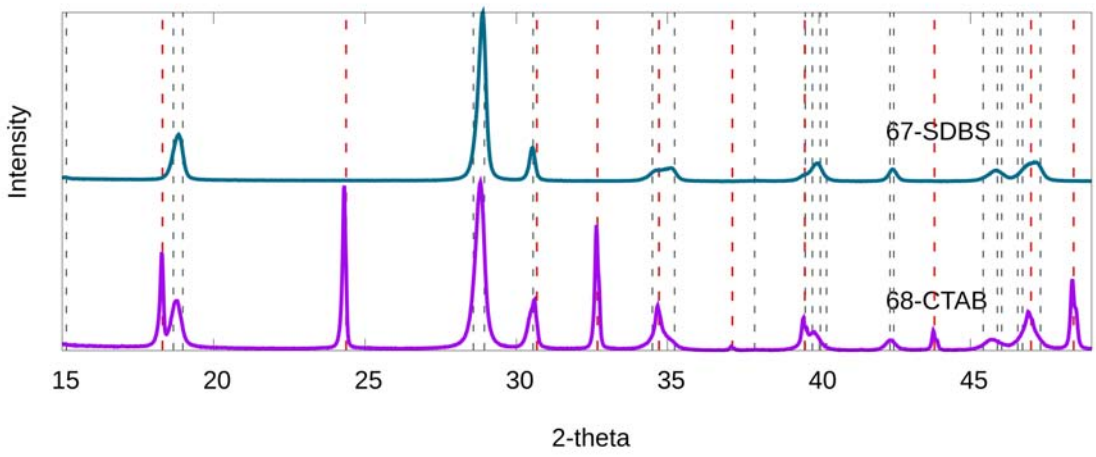

Figure 30: X-ray powder diffractogram of $BiVO_4$ samples, which were prepared by a solvent dependent synthesis with constant irradiation temperature of 200 °C, pH of 0.88 and irradiation time of 40 min during preparation. The diffractograms have the following notation: sample number-type of surfactant. The black dashed line represents the peak positions in the reference X-ray diffractogram of the monoclinic $BiVO_4$, whereat the red dashed line represents the reference of tetragonal $BiVO_4$

Table 20: Crystallite sizes calculated by the Sherrer equation using the highest intensity peak respectively

Sample number-surfactant	67-**SDBS**	68-**CTAB**
Crystallite size [nm]	30.06	26.03

3.3.4 UV-Vis Diffuse reflectance spectroscopy and Fourier-transformed Infrared spectroscopy

The UV-Vis Diffuse reflectance spectra of the samples was measured and is shown in figure 31. All the samples show steep absorption in the range of 400-500 nm. According to the X-ray powder diffraction of these samples, which are shown in section 3.3.3, besides of the samples which were prepared with the addition of 25%, all the samples resulted in a mixed phase of either monoclinic and zircon tetragonal $BiVO_4$ or scheelite tetragonal and zircon tetragonal. The samples which are a mixed phase of tetragonal and monoclinic $BiVO_4$ should show a step like absorption in the range of 420-500 nm, however in the absorption spectra there are only steep absorption curves visible, which are characteristic for the monoclinic phase of $BiVO_4$. The band gaps estimated from the Tauc-plot, and is shown in table 21. Sample 72 and 34 have an established band gap of 2.4 eV. For sample 73 and 35 2 band gaps could be calculated from the Tauc-plot. Every other sample has a band gap, which is higher, than 2.4 eV as expected from their green color. According to the published results of Tayyebi et al.[147] the appearance of scheelite tetragonal $BiVO_4$ is a green powder, which is in correlation with the appearance of the samples, which were prepared with different amounts of ethanol as a solvent.

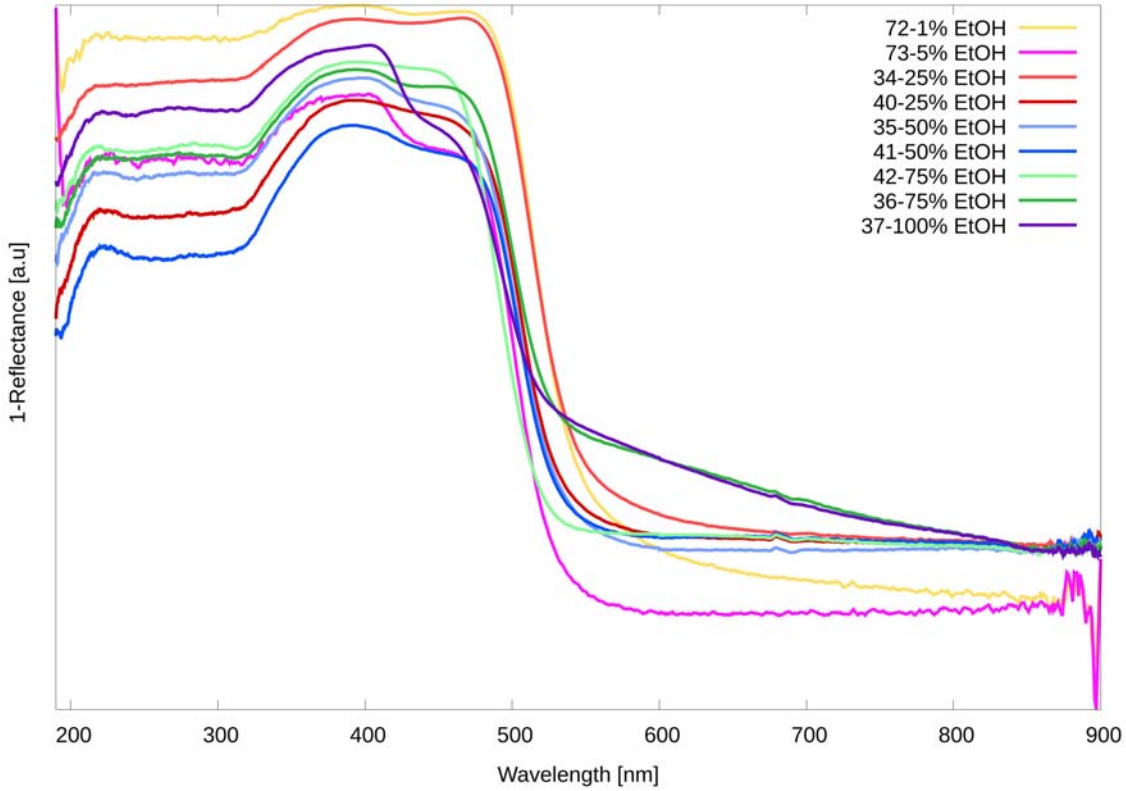

Figure 31: Diffuse reflectance spectra of $BiVO_4$, which were obtained by varying the amount of solvent during the synthesis and keeping the irradiation time, temperature and pH value constant (200 °C, 40min, pH 0.88). The spectra has the following notation: Sample number-solvent

Table 21: Estimated band gaps of $BiVO_4$

Sample number	**72**	**73**	**34**	**40**	**35**	**41**	**42**	**36**	**37**
band gap [eV]	2.4	2.39 2.56	2.4	2.43	2.39 2.47	2.45	2.48	2.44	2.48

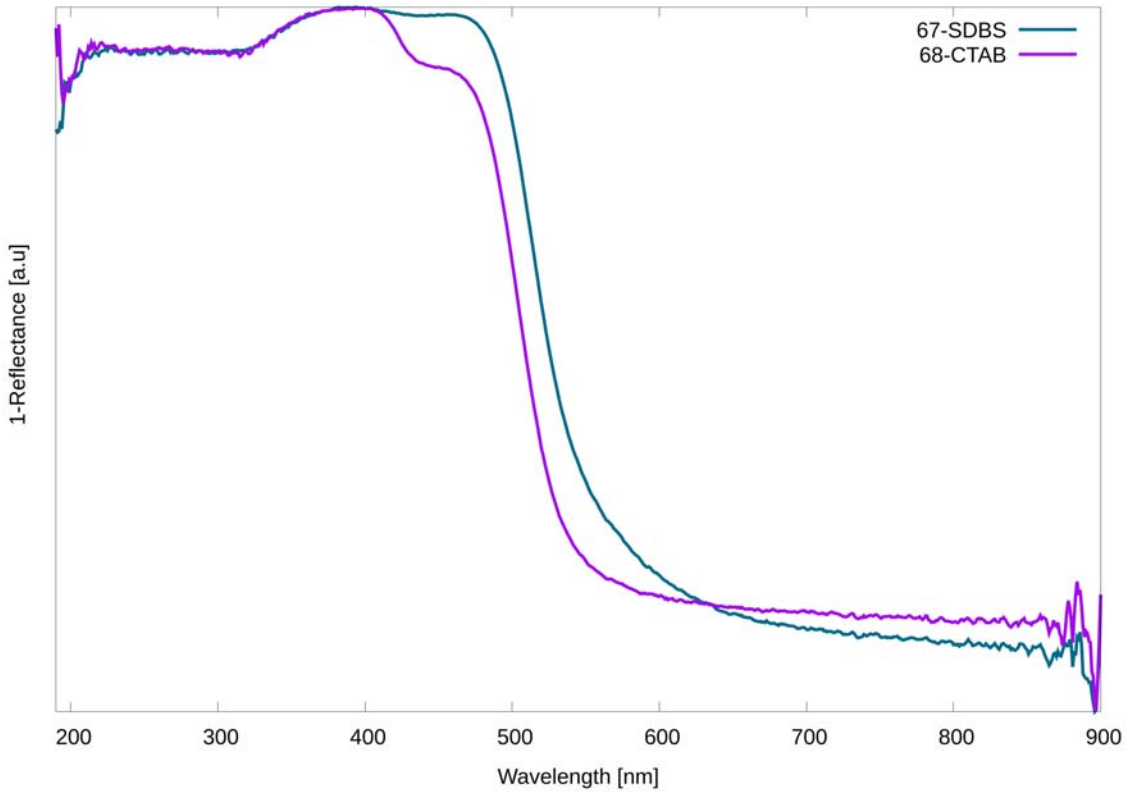

Figure 32: Diffuse reflectance spectra of $BiVO_4$, which were obtained by varying the type of surfactant during the synthesis and keeping the irradiation time, temperature and pH value constant (200 °C, 40min, pH 0.88). The spectra has the following notation: Sample number-surfactant

Table 22: Estimated band gaps of $BiVO_4$

Sample number	**67**	**68**
band gap [eV]	2.38	2.43; 2.66

According to the X-ray powder diffraction patterns of the as-synthesised products, besides of the samples synthesised with 25% ethanol added to the reaction mixture, all of the resulted in a mixed phase between zircon tetragonal and monoclinic $BiVO_4$ or scheelite tetragonal or zircon tetragonal $BiVO_4$. The samples which were evaluated as a mixed phase of $mBiVO_4$ and $tBiVO_4$ should show a step like absorption in the range of 420-500 nm in their diffuse reflectance spectra, however, all the samples show absorption behaviour, which is characteristic for monoclinic $BiVO_4$. Sun et al. evaluated an intermediate product, which is formed during the synthesis of monoclinic $BiVO_4$, with the structural composition of $BiVO_4 \times 0.4H_2O$. $BiVO_4 \times 0.4H_2O$ is reported to show an XRD pattern which is characteristic for the tetragonal $BiVO_4$. The authors assume, that the aligned tunnels in $mBiVO_4$ provide space for the intercalation of water molecules, which in turn leads to lattice distortion of $mBiVO_4$, thus enabling the XRD pattern of hydrated $BiVO_4$ to look like that of $tBiVO_4$. The authors identified the product among other analysis techniques with fourier transformed infrared spectroscopy as well.[148] Hence, FT-IR analysis was performed and is shown in figure 35. As comparison the FT-IR spectra of a few samples which were evaluated as only monoclinic and a mixture of monoclinic and tetragonal $BiVO_4$ (see section 3.1) are shown in figure 33. The FTIR spectrum of

the $BiVO_4$ shows an intense and broad band that includes the characteristic bands of $BiVO_4$; the symmetric and asymmetric stretching vibrations of VO_4 at 737 cm^{-1} and 830 cm^{-1} [149], respectively. The band at 1623 cm^{-1} corresponds to bending vibrations of adsorbed H_2O molecules. [150,151] In figure 34 one FT-IR spectrum of monoclinic and tetragonal $BiVO_4$ is shown from 500-1000 cm^{-1} respectively. It is visible, that the peak at approximately 850 cm^{-1} is red shifted for tetragonal $BiVO_4$ compared to monoclinic $BiVO_4$ which is derived from the symmetric and antisymmetric stretching vibration of the V-O bond in the VO_4 tetrahedra. The reason for the red shift is the structural distortion of monoclinic $BiVO_4$ compared to tetragonal $BiVO_4$, whereat the V-O bond has 4 equivalent distances in the tetragonal $BiVO_4$ and 2 different distances in the monoclinic $BiVO_4$.[142] CO_3^{2-} derived band is marked with a blue dashed line in figure 33 and figure 35 at approximately 1420 cm^{-1}. The peak at approximately 1030 cm^{-1} is originating from aliphatic C-H vibrations, and is marked with a lilac dashed line in figure 33 and figure 35.[142] The peak could appear due to the adsorption of atmospheric carbon dioxide during the sample preparation.[150] The band at approximately 1623 cm^{-1}, which corresponds to the bending vibrations of H_2O is marked with a red dashed line in figure 33 and figure 35.[152] The peak at 1623 cm^{-1}, which indicates the presence of water is visible on the FT-IR spectra of the monoclinic samples 02 and 03, which is shown in figure 33. However, the peak is not visible for the tetragonal samples 07 and 09 shown in figure 33 Furthermore, the peak at 1623 cm^{-1} is slightly pronounced in the samples shown in figure 35 a) and b) besides for sample 72, which was made with the addition of 1% ethanol to the reaction mixture. The FT-IR spectra of the samples which were prepared with the addition of 5%, 25%, 50%, 75% and 100% ethanol to the reaction mixture, could have resulted in a product with absorbed water on their surface. The presence of water could even lead to the conclusion, that the preparation of the samples 73, 34, 40, 35, 41, 36, 42 and 37 resulted in the intermediate product $BiVO_4 \times 0.4H_2O$. As mentioned above the product $BiVO_4 \times 0.4H_2O$ was observed by Sun et al.[148], which is a monoclinic structured product with intercalated water molecules, which shows the XRD pattern of tetragonal $BiVO_4$. Regarding the presence of water in the samples which were prepared with different amounts of ethanol, evidenced by FT-IR, and the tetragonal XRD pattern of the same samples, the conclusion can be made, that these samples resulted in the intermediate product $BiVO_4 \times 0.4H_2O$.

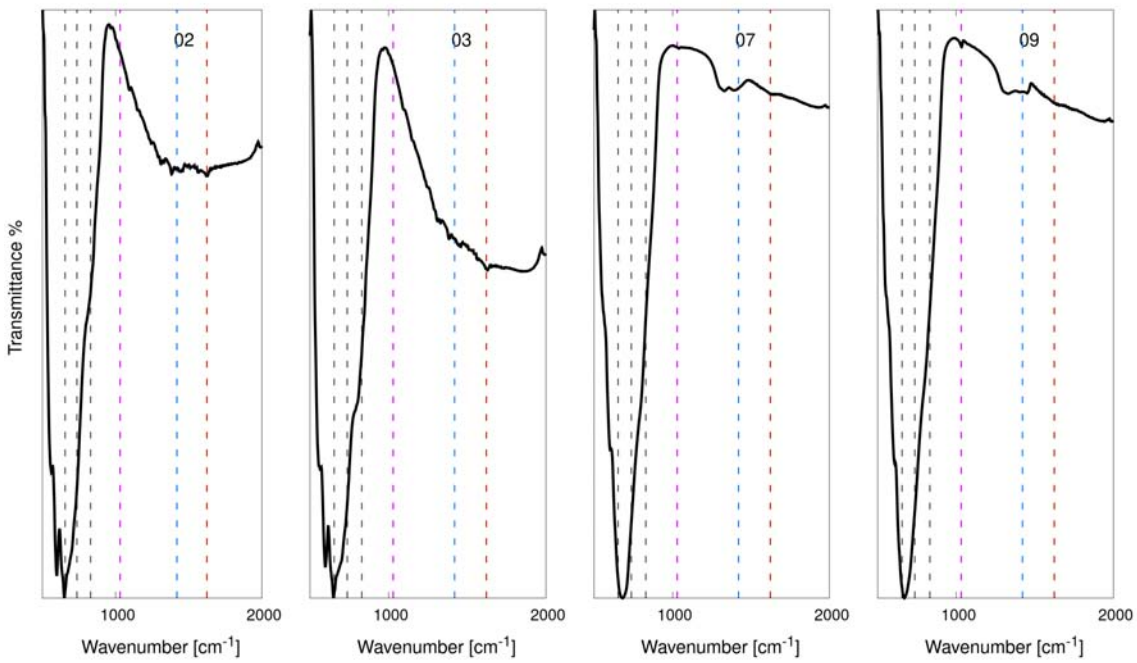

Figure 33: FT-IR spectra of the samples with the number 02, 03, 07 and 09, of which synthesis details are shown in section 2.4.1 and results in section 3.1; sample 02 and 03: monoclinic $BiVO_4$, sample 07 and 09: tetragonal $BiVO_4$; black dashed line: VO_4, red dashed line: bending vibrations of absorbed H_2O, blue dashed line: CO_3^{2-}, lilac dashed line: C-H vibrations [149–151]

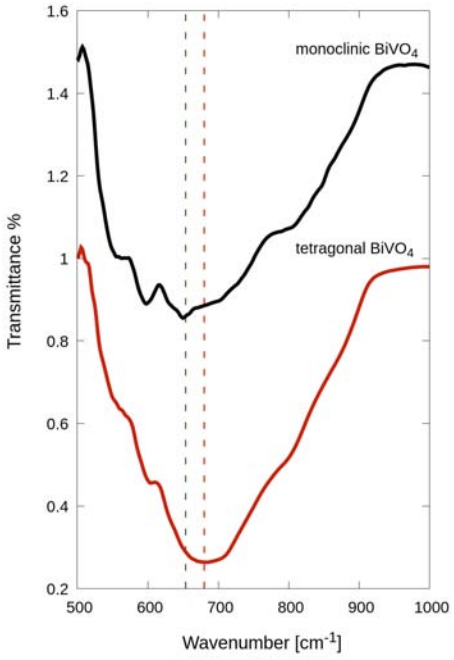

Figure 34: FT-IR spectrum of monoclinic and tetragonal $BiVO_4$

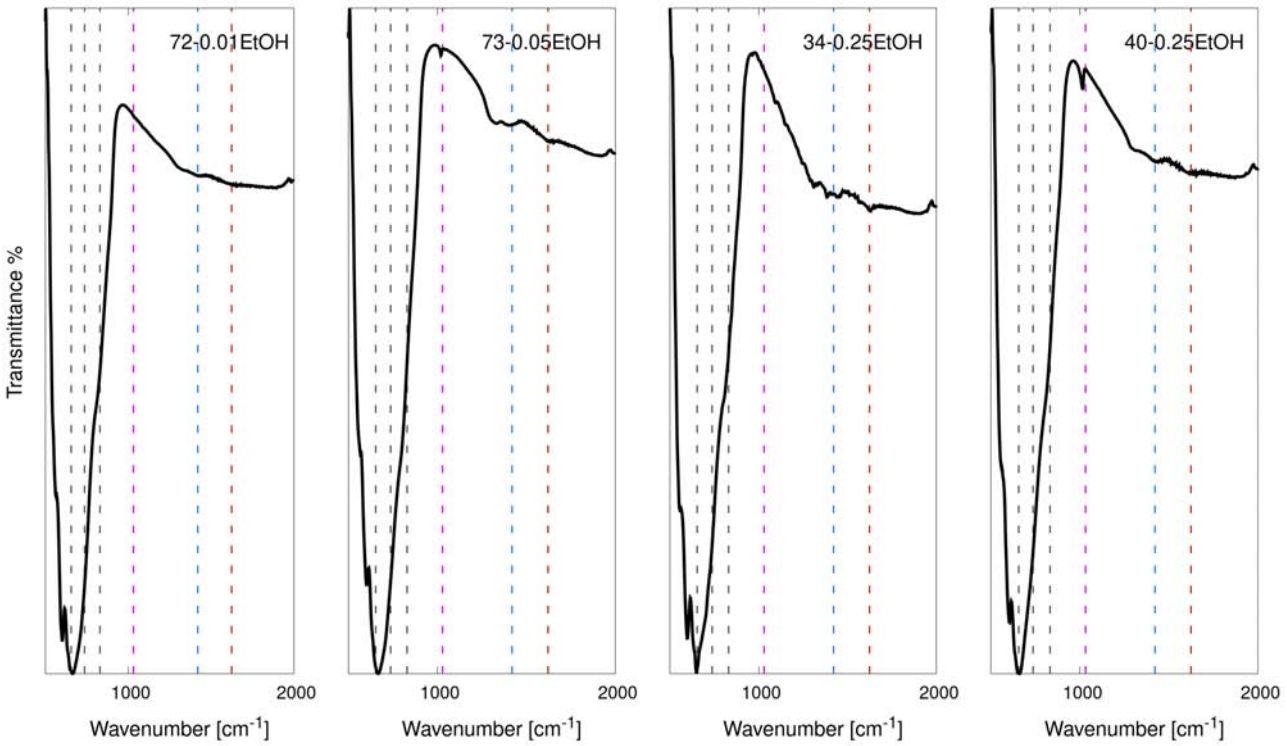

(a)

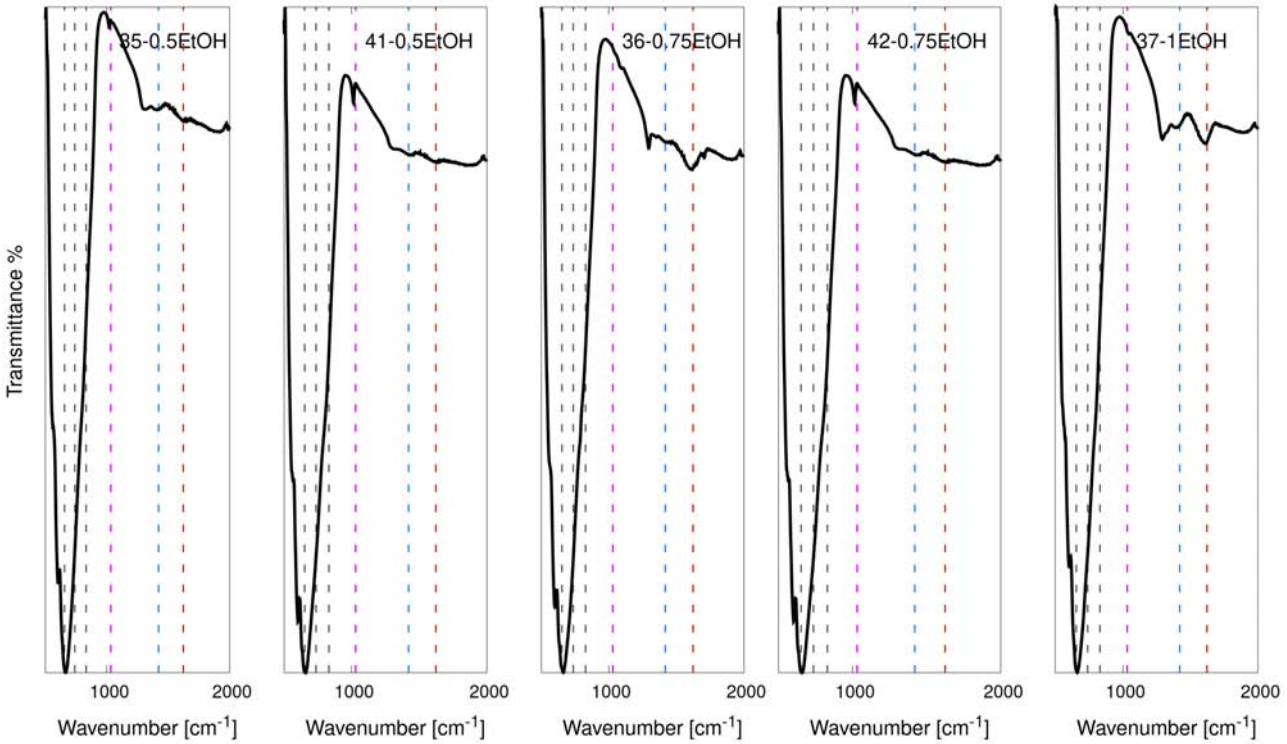

(b)

Figure 35: FT-IR spectra of the samples which were prepared with the addition of ethanol to the reaction mixture; black dashed line: VO_4, red dashed line: bending vibrations of absorbed H_2O, blue dashed line: CO_3^{2-}, lilac dashed line: C-H vibrations[149–151]

3.3.5 Summary

The table 23 and table 24 summarizes the results of the synthesis of $BiVO_4$ at which different amounts of ethanol was used as a solvent and different type of surfactants were used, respectively. The morphology of the particles, polymorph, crystallite size, band gap, and OER activity are shown dependent on the microwave irradiation time during preparation. The synthesis was carried out in order to control the morphology of the obtained semiconductors during synthesis. According to Rodrigues et al.[126], the use of ethanol as a solvent should lead to the formation of 2D materials. Only one SEM image showed plate like morphology, namely the sample which was prepared with 75% of added ethanol to the reaction mixture. In general a predominant number of the samples of the solvent dependent and surfactant dependent synthesis resulted in scheelite tetragonal $BiVO_4$ or composites between scheelite tetragonal and zircon tetragonal $BiVO_4$, which are expected to have poor oxygen evolution activity.

Table 23: Summary of the results discussed in section 3.3 for the samples, whereat different amounts of ethanol was added during the synthesis

Ethanol [%]	Sample number	Morphology	Size [µm]	Polymorph	Crystallite size [nm]	Band gap [eV]	Oxygen evolution activity [µmol/h]
1	72	cluster of octahedrons	4-10	m + t-z	25.86	2.4	0.186
5	73	sphere like morphology	1-2	t-s + t-z	25.93	2.39; 2.56	0.088
25	34	cluster of smaller polyherdrons + grains in the nm range	cluster:10; smaller particles: few nm	t-s	20.79	2.4	0.413
25	40	sphere shaped cluster of smaller particles + needle like morphology	4-10	t-s	29.44	2.43	0.06
50	35			t-s + t-z	27.21	2.39; 2.47	0.126
50	41	cluster of smaller particles + needle like morphology	4	t-s + t-z	25.21	2.45	0.076
75	36	-	-	t-s + t-z	25.24	2.44	0.145
75	42	small grains + plate like particles	grains: nm range; plates: 5 µm	t-s + t-z	25.25	2.48	0.375
100	37	layered structure	5	t-s + t-z	25.54	2.48	0.025

Table 24: Summary of the results discussed in section 3.3 for the samples, whereat different surfactants was added during the synthesis

Surfactant	Sample number	Morphology	Size [µm]	Polymorph	Crystallite size [nm]	Band gap [eV]	Oxygen evolution activity [µmol/h]
SDBS	67	sphere like cluster of smaller particles	2-5	st	30.06	2.38	0.197
CTAB	68	sphere like cluster of smaller particles	3-4	st+zt	25.93	2.39; 2.56	0.158

3.4 Oxygen evolution reaction

This section will report results of the photocatalytic OER tests for the prepared samples, including those prepared at various pH (section 2.4.1) and various time (section 2.4.3), as well as those prepared using EtOH co-solvent and surfactants (section 2.4.4).

The oxygen evolution was evaluated of all the $BiVO_4$ samples by irradiating with a 445 nm LED lamp. The OER setup is shown in figure 10. The catalyst amount was 1 mg, as a sacrificial agent 20 µmol $AgNO_3$ was used in 2 mL of deionized water (details in section 2.3.1)

The figure 36 gives an explicit overview of the oxygen evolution activities of the samples which were synthesised at different reaction conditions. The figure 36 a), b), c) and d) shows the oxygen evolution in µmol plotted against the UV-lamp irradiation time in minutes, which are assorted by the variation of the reaction parameter during preparation of the catalyst. The black line represents a reference experiment performed only with the sacrificial agent $AgNO_3$ and without any catalyst present under visible light irradiation, while the grey line represents the activity of TiO_2 under visible light irradiation. The figure 36 b) contains the catalytic activity of one hour visible light irradiation of the sample which was prepared without microwave irradiation.

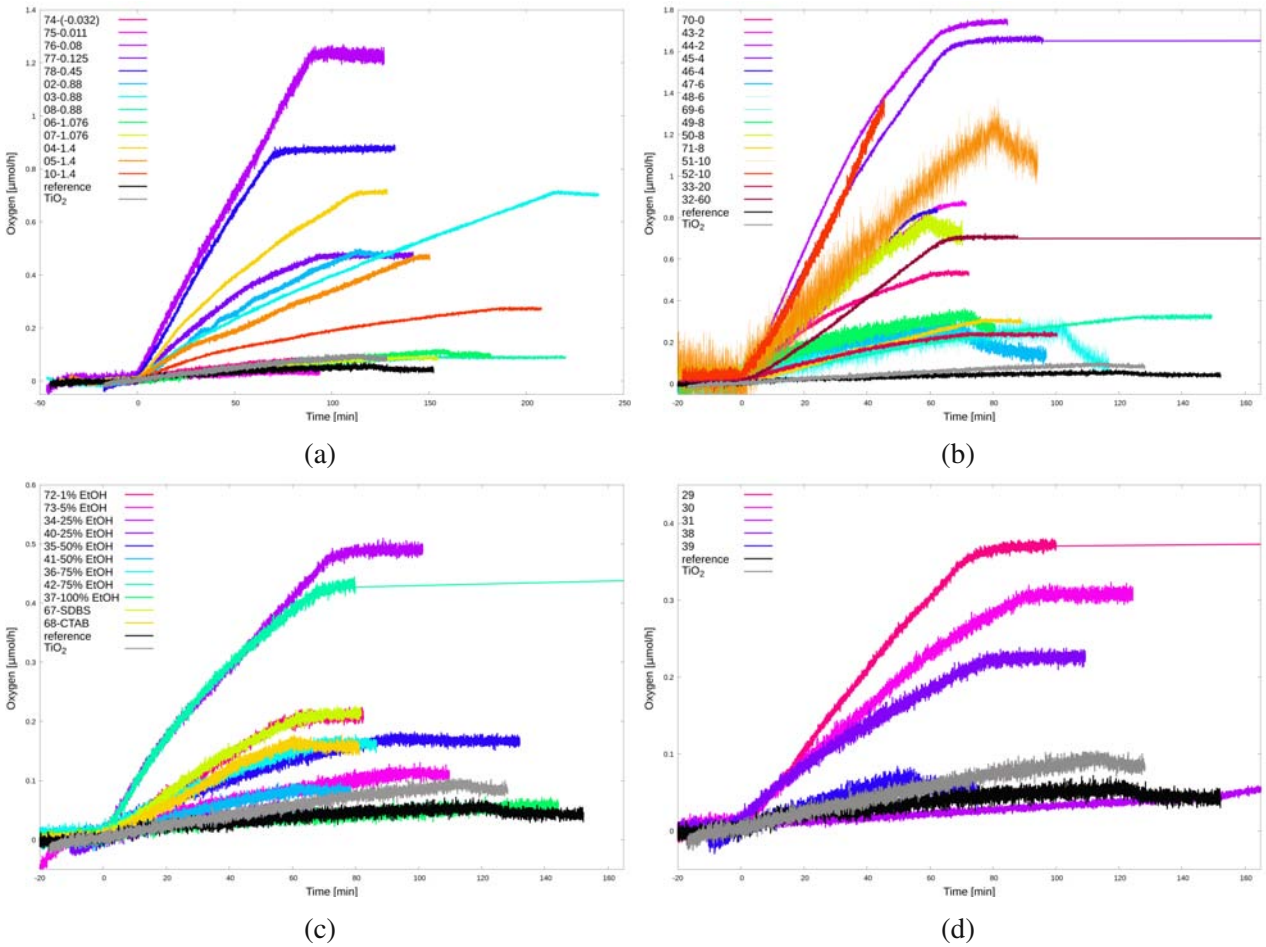

Figure 36: Summary of the oxygen evolution reaction activity in µmol/h of $BiVO_4$; a) : OER activity of the samples prepared with different pH values; b): OER activity of the samples prepared at different microwave irradiation times; c): OER activity of the samples prepared with the variation of solvent and surfactant; d): OER activity of the samples prepared as reference material

3.4.1 OER activity of the photocatalysts obtained via pH dependent synthesis

Figure 37 shows the activity of the catalysts as bar diagrams after one hour of visible light irradiation in µmol/h. The blue filled bars represents the monoclinic $BiVO_4$, the bars with magenta color represents the samples, which resulted in a mixed phase between monoclinic and tetragonal $BiVO_4$, and the bars with a orange colour represents the tetragonal $BiVO_4$ samples. From figure 37 it is visible, that in general monoclinic samples have better OER activities , than tetragonal or mixed phase samples. The summary of the morphology, size, XRD, OER activity of the samples which were prepared at different pH values is shown in section 3.1.5, and these parameters are need to be taken into account, in order to explain, why the oxygen evolution reaction activity has the following order: pH:0.08>0.45>1.4>0.125>0.88. From the pH series, the sample which was prepared at the pH of 0.08 has the highest OER activity. The reason for that could be, that the sample resulted in capped octahedron morphology with highly exposed 010 facets. As mentioned earlier, the exposure of the 010 facet is influencing the OER activity. Besides of the excellent morphology, the sample prepared at the pH value of 0.08 has a high established band gap value. The sample prepared at the pH value of 0.45 shows well defined capped octahedron morphology, but its 010 facet is not that exposed. Its calculated band gap is 2.4 eV and according to the SEM the size of the particles are about 2 µm. The SEM results of the sample prepared at the pH value of 0.125 reveals a cluster of polyhedron morphology, which could be the reason, that this sample performed worse compared to the other samples.

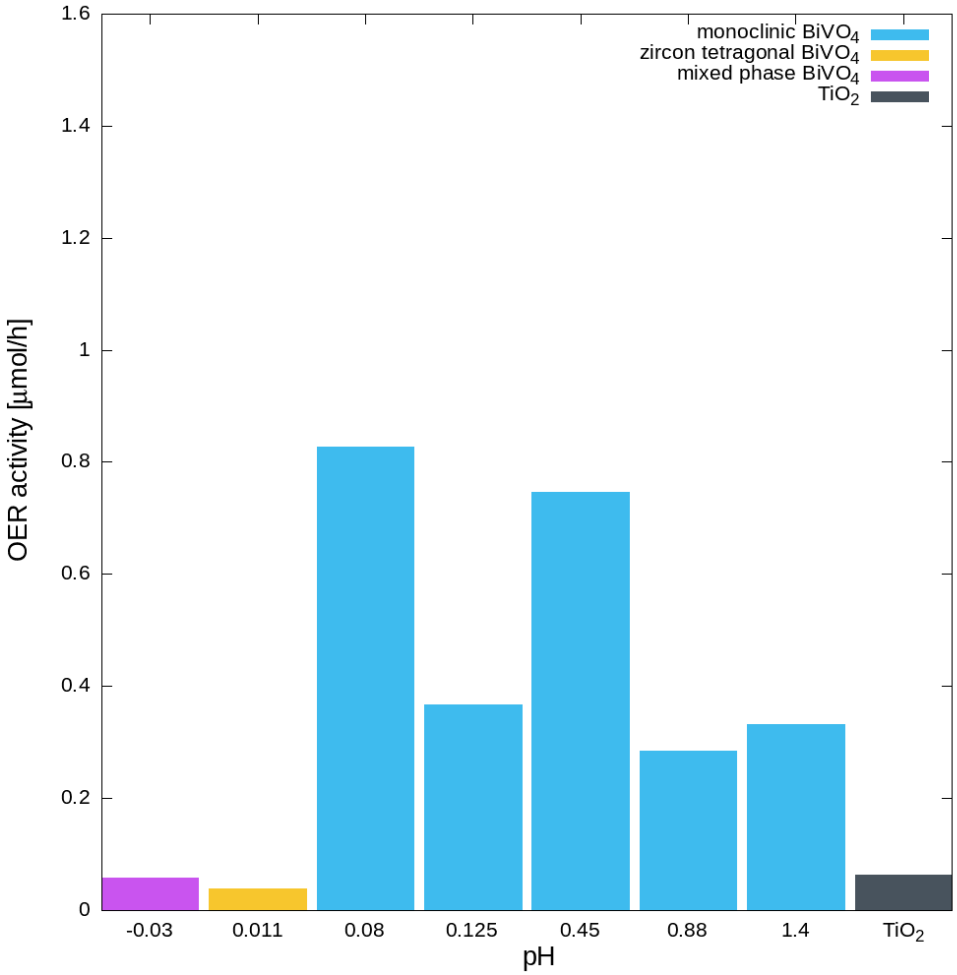

Figure 37: Summary of the oxygen evolution reaction activity in µmol/h of $BiVO_4$ plotted as bar diagram of the samples prepared with different pH values

3.4.2 OER activity of the photocatalysts obtained via time dependent synthesis

The results of the samples, which were synthesised at different microwave irradiation times are summarized in section 3.2.5. Their OER activity is shown in figure 38, The oxygen evolution activity of the photocatalysts acquired by the microwave irradiation time dependent synthesis have no linear trend of the catalytic activity and the synthesis time. The catalytic activity decreases in the following order: 4 min>10 min>2 min>8 min>60 min>20 min>6 min. To understand this trend, the results of morphology , crystallinity and band gap are used. The morphology has a decisive influence on the catalytic activity. Namely, well defined capped octahedron shaped crystals have better activity than polyhedron. Thus, the activity of the photocatalyst synthesized at 8 minutes of microwave irradiation is relatively low because the morphology resulted in polyhedron and irregular shaped particles. The exposure of the 010 facets of the crystal has a significant influence on the catalytic activity. Thus, the product synthesized at 4 minutes of microwave irradiation time has the best photocatalytic activity because the 010 facets of this semiconductor are very exposed. The crystallite size plays a crucial role in the photocatalytic reaction, since the recombination probability of the photogenerated charge carriers is high if the photocatalyst has small crystallite size. Thus, the catalytic activity is high at larger crystallite sizes as also observed in the photocatalyst made with 2 minutes of microwave irradi-

ation. And the photocatalytic activity is low for those samples, which had small calculated crystallite sizes, such as the sample which was prepared at 6 minutes of microwave irradiation and 20 minutes of microwave irradiation. A trend can be observed in the relationship between the band gap and the oxygen evolution activity, such as the higher the band gap, the higher the catalytic activity of a semiconductor. All the above parameters have a great effect on the catalytic activity. However, the relationship between the parameters and the oxygen evolution reaction activity is complex, because the activity depends not only on one parameter but on the interaction of all parameters.

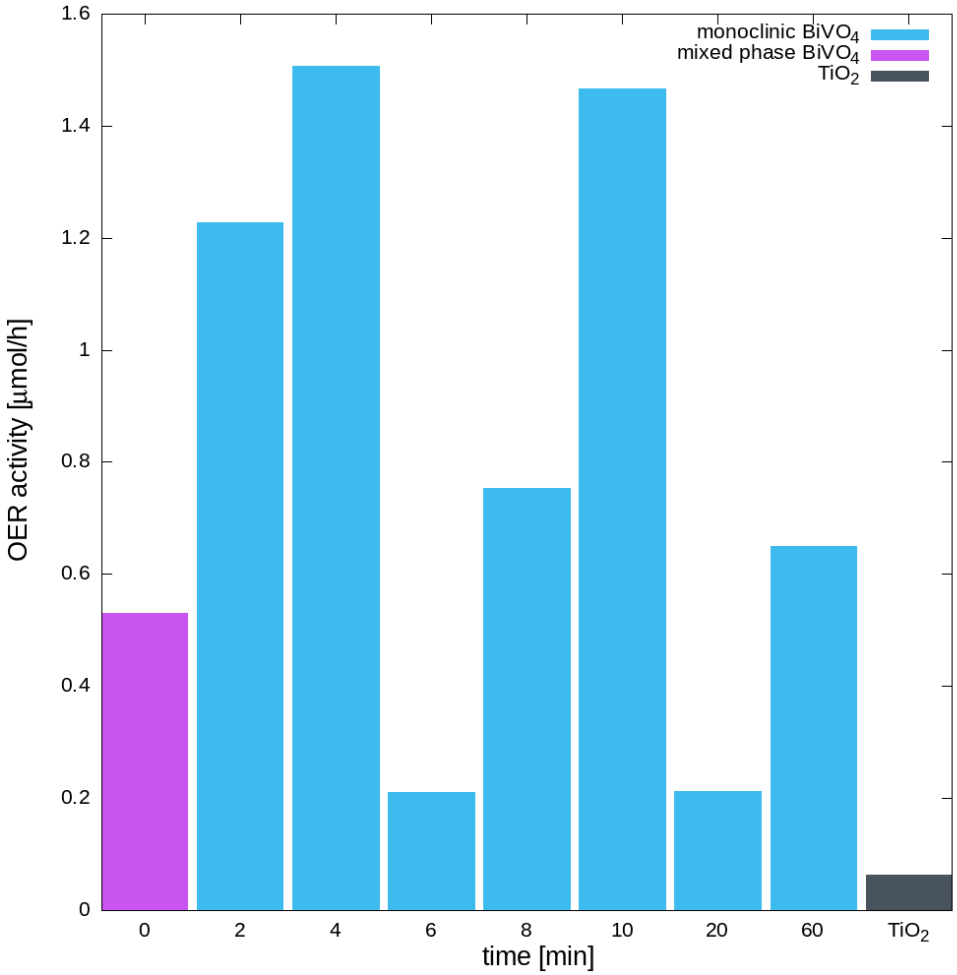

Figure 38: Summary of the oxygen evolution reaction activity in µmol/h of $BiVO_4$ plotted as bar diagram of the samples prepared with different microwave irradiation times

3.4.3 OER activity of the photocatalysts obtained via the solvent and surfactant dependent synthesis

The results of the samples, which were prepare with different amount of ethanol and different surfactants are shown in section 3.3.5. Their oxygen evolution reaction activity is plotted as a bar diagram and shown in figure 39. The samples mostly resulted in a mixed phase between scheelite tetragonal and zircon tetragonal $BiVO_4$. The OER activity of the products, which resulted in the monoclinic phase is higher in average, than the OER activity of the mixed phase samples. The morphology of mixed-phase samples explains why some photocatalysts had better activities than others. For example,

the semiconductor with the best activity, namely the sample made with the addition of 75% ethanol to the reaction mixture, had plate like morphology, whereat it is assumed, that the large surface area is advantageous for the OER reaction. Furthermore, this sample also has a large determined band gap compared to other samples in this array, which is also an indicator of good catalytic activity. As discussed in chapter xy, the parameters of polymorph type, morphology, band gap and crystallite size also seem to play a role in deciding why some photocatalysts perform better. However, the activity depends not only on one parameter but on the interaction of all parameters.

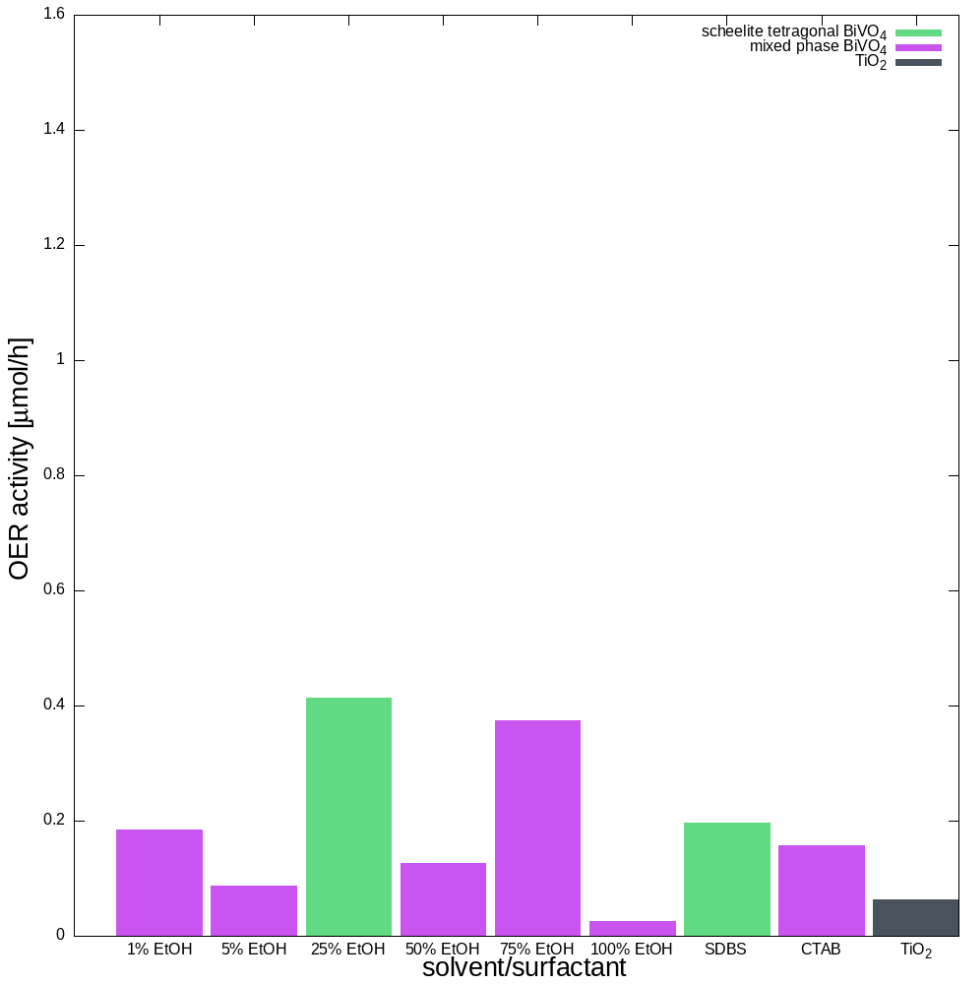

Figure 39: Summary of the oxygen evolution reaction activity in µmol/h of $BiVO_4$ plotted as bar diagram of the samples prepared with the addition of different amounts of ethanol and surfactants

3.4.4 Factors in control of OER performance

By analyzing different series of samples, it could be concluded that independent of the synthetic process and the synthetic parameters, some morphological and structural factors seem to determine the performance. Given the large pool of samples produced in this work, this chapter deals with the general correlation between these parameters and photocatalytic performance.

The different polymorphs of the product were put in relation with the oxygen evolution activity and are shown in figure 42 a). From this visualisation it is clear, that the monoclinic samples had the best oxygen evolution activity. Monoclinic $BiVO_4$ seems best for visible light-active photocatalytic

water splitting compared to the tetragonal phases because monoclinic $BiVO_4$ exhibited the narrowest band gap of all. Furthermore, the band gap of monoclinic $BiVO_4$ is an indirect band gap, which is advantageous for the separation of photogenerated charge carriers.

The oxygen evolution activity was investigated with the focus on the morphology of the products. The graphical representation of this relation is shown in figure 42 b). On figure 42 b) it is visible, that the samples which had capped octahedron and polyhedron morphology performed the best in the OER in average. The samples which exhibited highly exposed 010 facets had the best OER activity, because the water oxidation reaction is thermodynamically more favourable on the 010 facet, than on other facets.

The size of the particles was determined from the SEM images of the crystalline $BiVO_4$ products. The relation of the OER activity to the size of the particles is shown in figure 42 c). The relation is plotted with boxplots. For the sizes 1 µm, 1.5 µm, 4.5 µm, 5 µm and 10 µm there was only one corresponding OER activity value. More OER activity values belongs to the sizes 2 µm, 2.5 µm, 3 µm, 3.5 µm and 4 µm, and in the figure 42 b). The samples, which resulted in the average size of 3.5 µm had the highest OER activity.

The relation of the OER activity in µmol/h and the crystallite size in nm, is shown in figure 42 d). From the figure 42 d) it is visible, that the increase of the crystallite size leads to a higher OER activity. The reason for that could be, that with bigger crystallite sizes the semiconductor has less defects. Defects provide recombination centers for the photoinduced charge carriers. The less defects a semiconductor has, the better the charge carrier separation.

The relation of the band gap is investigated against the OER activity of the monoclinic samples, and is shown in figure 42 e). The OER activity is increasing with increasing band gap of the monoclinic samples. It can be assumed, that with increasing band gap, the oxygen evolution reaction is made thermodynamically more favourable, by lowering the valence band position of monoclinic $BiVO_4$.

In summary, during the evaluation of the OER activity trend in figure 36, there was found out, that most of the properties of the crystalline products are accountable for the efficiency of the OER. In general, monoclinic products have the highest visible light active photocatalytic activity. Among the monoclinic products, those, which showed capped octahedron like morphology in their SEM data have performed better in the OER, especially those samples with exposed 010 facet. Figure 40 shows the photocatalytic activity in decreasing order for monoclinic $BiVO_4$ as a function of morphology. It is visible, that the best performing semiconductors exhibit exposed 010 facets, and the photocatalytic activity decreases with decreasing exposure of the 010 facet in the capped octahedron morphology. Furthermore, the photocatalytic activity significantly decreases for polyhedra and clusters of polyhedra. The connection between the morphology and the OER activity is shown as well in figure 41. The ratio of the 040 121 facets was determined from the XRD data and was plotted against the OER activity. From figure 41 it is visible, that the catalytic activity increases with increasing 040/121 facet ratio.

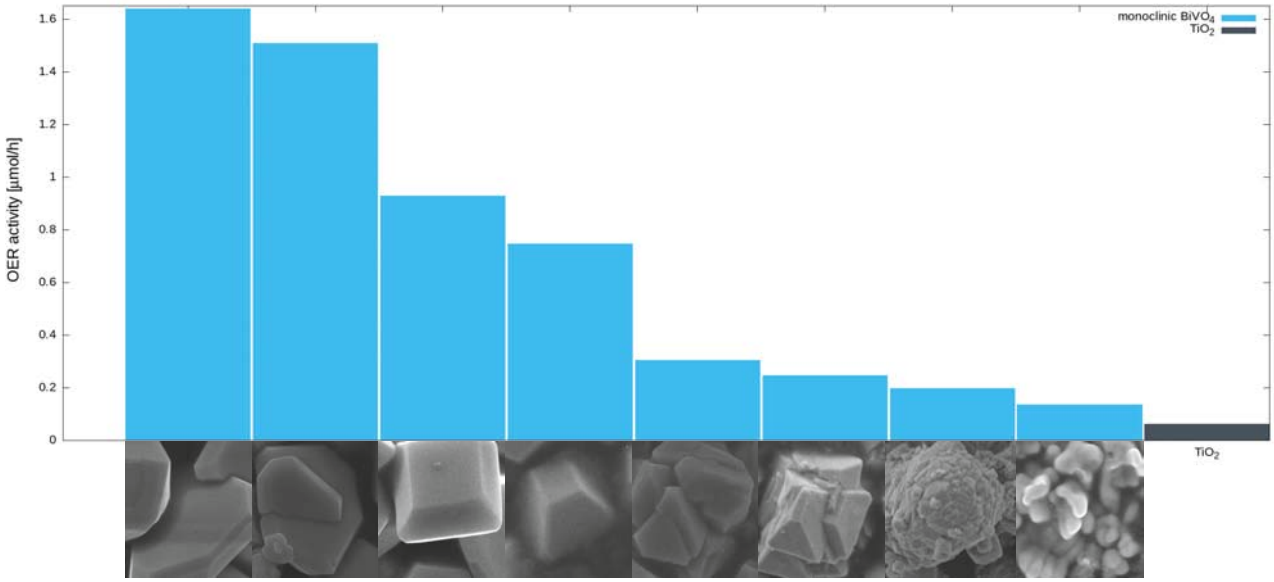

Figure 40: Oxygen evolution activity of some selected samples in µmol/h against the morphology of monoclinic $BiVO_4$

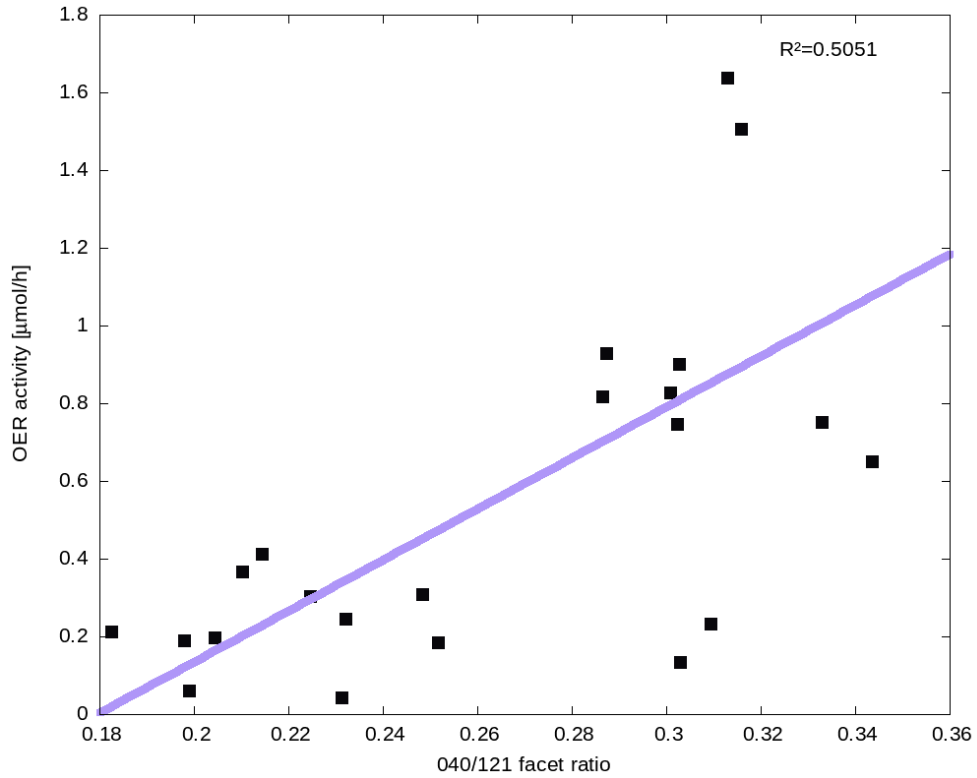

Figure 41: Oxygen evolution reaction activity plotted against the 040 121 facet ratio which was determined from the XRD data of all the monoclinic samples

For a good OER activity the average particle size of in the range of 2-3.5 µm is preferred. The OER activity increases with increasing band gap value and increasing crystallite size. However, it was found out, that the value of the band gap has a higher impact on the OER activity than the crystallite

sizes. In figure 42 e) the influence of the band gap value on the OER activity is visualized, and the influence of the crystallite size on the OER activity is shown in figure 42 d). The linear regression between OER activity and the band gap is more accurate, than between OER activity and crystallite size, which is a further indication, that the band gap value has a higher influence than the evaluated crystallite size.

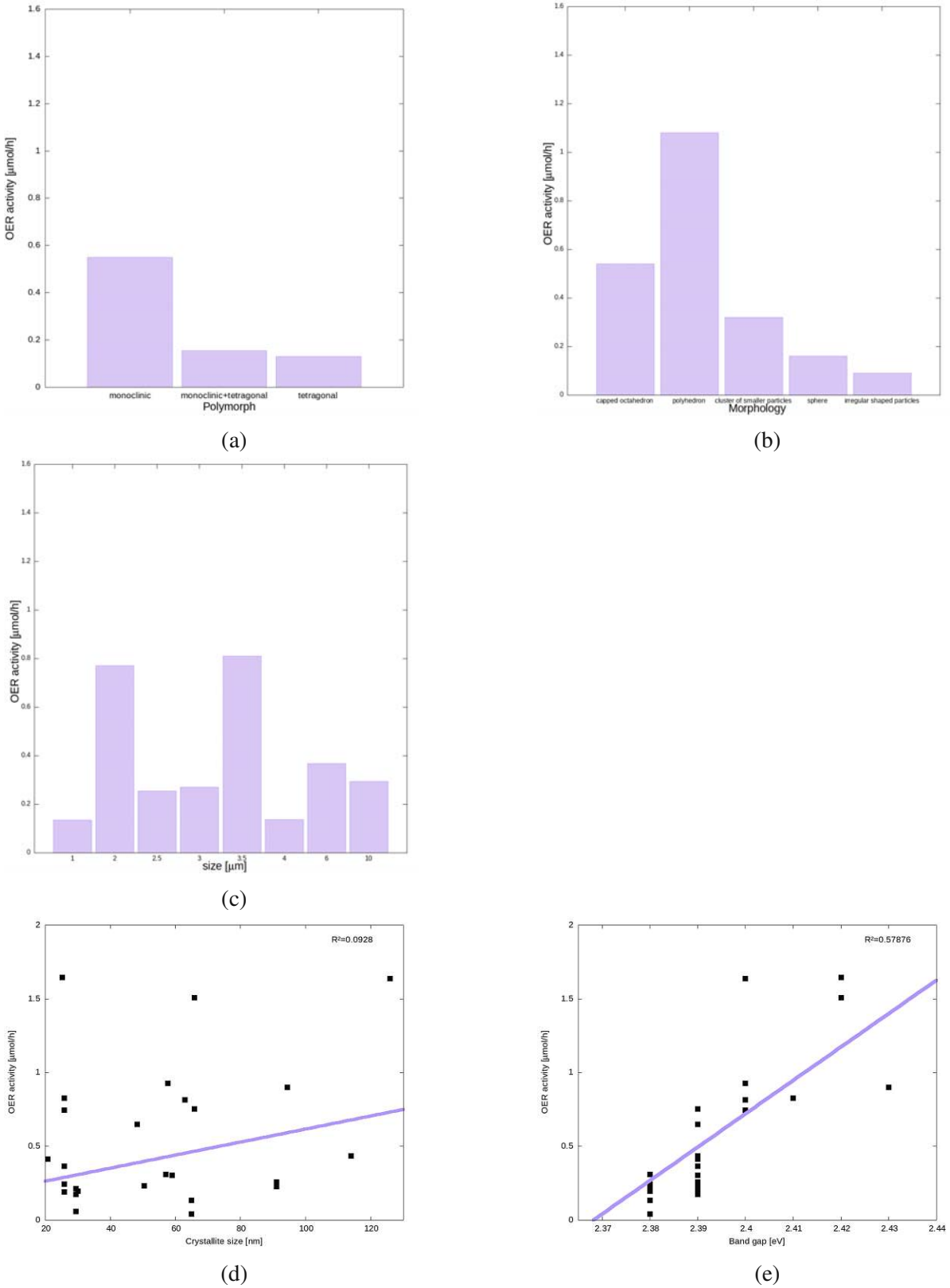

Figure 42: Summary of the oxygen evolution activity in µmol/h of $BiVO_4$; a) OER activity of the samples are plotted against different polymorphs evaluated by XRD; b) OER activity of the samples are plotted against different morphology observed in SEM; c) OER activity of the samples are plotted against the size of the particles observed in SEM; d) OER activity of the samples are plotted against their crystallite sizes calculated by the Scherrer-equation; e) OER activity of the monoclinic samples plotted against their band gap calculated by the Tauc-plot

4 Conclusion

In the present work monoclinic $BiVO_4$ was succesfully synthesised with a facile microwave assisted hydrothermal synthesis protocol, by varying the synthesis parameters, such as pH, irradiation time, amount of ethanol as a solvent and type of surfactant. The pH dependent synthesis was tried out in order to obtain monoclinic $BiVO_4$ with well defined morphology. It was found out, that low pH values lead to mixed phase or tetragonal $BiVO_4$, too high pH values lead to undefined morphology. Hence and optimum pH of 0.08-0.88 was determined. The time dependent synthesis was tried out in order to understand the formation mechanism of $BiVO_4$. Already 2 minutes of microwave irradiation lead to monoclinic $BiVO_4$ particles with well defined capped octahedron morphology, and already 10 seconds of microwave irradiation was sufficient to obtain particles with polyhedron morphology. Different amounts of ethanol as a solvent, and different type of surfactants were used during the synthesis in order to control facet growth. A predominant number of these samples resulted in scheelite tetragonal $BiVO_4$. The expected facet growth control effect was only archieved at one sample, which exhibited 2D morphology. The oxygen evolution activity of the samples was determined from aqueos solution and without the use of a cocatalyst by irradiation with visible light. The best oxygen evolution activites were originating from samples, which resulted in monoclinic $BiVO_4$. Its better OER perfromance was assigned to two factors. On one hand, its narrower band gap allows for stronger visible light absorption. On the other hand, the structural distortion of the VO_4 tetrahedra leads to the manifestation of optical anisotropy compared to scheelite tetragonal and zircon tetragonal phase. As a result, the Bi 6s lone state has a high impact on the valence band of the monoclinic $BiVO_4$ which favours separation of photoinduced charge carriers. In addition to the crystalline phase, other factors also have a major influence on the photocatalytic oxygen evolution reaction. The most suitable samples for catalytic water splitting were those with an octahedral morphology, especially when their 010 facets are exposed. The best particle size of the obtained crystals for OER proved to be in the range of 2-3.5 µm. A linear relationship was discovered between the crystallite size and the catalytic activity, the higher the crystallite size the better the catalytic activity. The value of the band gap had a stronger influence on the catalytic activity. The catalytic activity was also found to be increasing linearly with the band gap. The catalytic activity increases linearly with the increasing band gap value, with the influence of the band gap on the OER activity being much greater than the influence of the crystallite size. Sample 45 can serve as a representation of such an optimum (synthetic conditions are described in table 4).

5 Appendix

In the following chapter, the obtained raw data of SEM, XRD and DRS measurements of $BiVO_4$ are shown, which is intended to serve as supporting information to the section 3.

The results of the SEM, XRD, DRS, FT-IR spectroscopy and Raman spectroscopy measurements of $NiFe_2O_4$ are not conclusive, therefore the results of these measurements are shown in this chapter.

A $BiVO_4$

A.1 Scanning electron microscopy

A.1.1 pH variation

Unlike for the rest of the samples, during the preparation of sample number 02 0.16 mL of 100% HNO_3 was added to the reaction mixture. The same product with the sample number 02 was put in the oven overnight at 120 °C. The as-prepared crystals possesses octahedron morphologies with sharp corners and well-defined edges in the µm range. The annealing in the oven at 120 °C had no effect on the morphology of this sample.

The sample with the number 03 was prepared by adding 0.16 mL of 60% HNO_3 (measured pH 0.88) to the reaction mixture. The crystal plane with the higher growth rate disappear while the crystal plane with the lower growth rate would increase in area, which is resulting from the slight decrease in pH value, compared to the morphology of sample 02.

Further increased pH was obtained at the preparation of sample 07 (meassured pH 1.076), whereat 0.13 mL of 60% HNO_3 was added to the reaction mixture. The as-produced powder has two types of morphologies, namely irregular polyhedron like morphology, and loose sphere like morphology which consists of smaller crystals.

The sample 05 was prepared by the measured pH of 1.4. On the SEM image of sample 05 irregular polyhedron and and capped octahedron morphologies are visible.

There were two samples prepared at the reduced precursor concentration of 0.05 $\frac{mol}{L}$ at different pH values with the number 08 (pH 0.88) and 10 (1.4), respectively. The sample 08 possess irregular shaped particles, lose spheres, which consists of smaller particles and polyhedron like morphology as well. The SEM image of the sample 10 shows irregular shaped crystals.

The SEM image of the powder which were prepared at the measured pH of -0.03 and labeled as sample 74 shows sphere like morphology which is a cluster of smaller crystals, and octahedron shaped morphology is recognisable as well.

The sample 75 possess a sphere like morphology in the µm range, which consists of smaller crystals.

The sample with the sample number 76, which was prepared at the measured pH of 0.08 shows polyhedron with highly exposed 010 facets and further cut edges.

The sample 77 was prepared at the measured pH of 0.125 and shows a morphology of a big cluster, which consists of smaller polyhedrons.

The sample 78 was prepared at a measured pH of 0.45. On the SEM picture of the as-prepared sample a capped octahedron like morphology is visible.

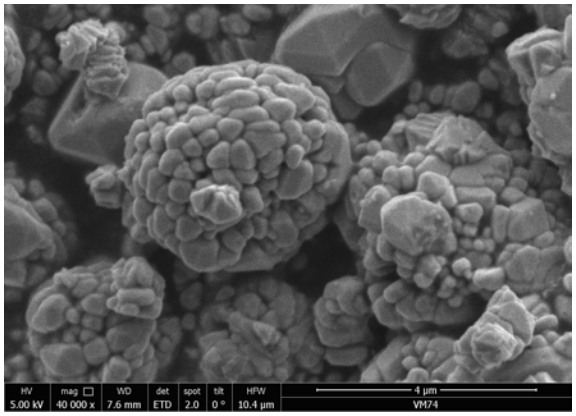

(a) 74-**-0.032**-1.25-40

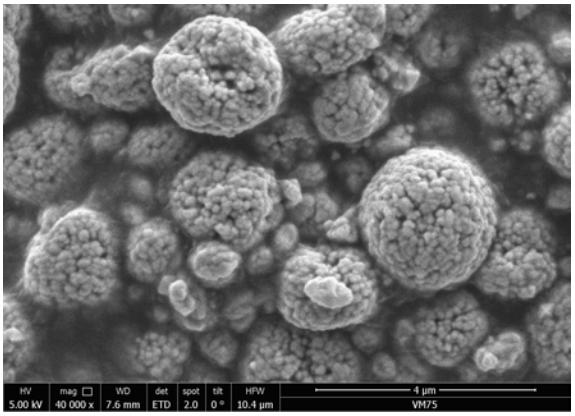

(b) 75-**0.011**-1.25-40

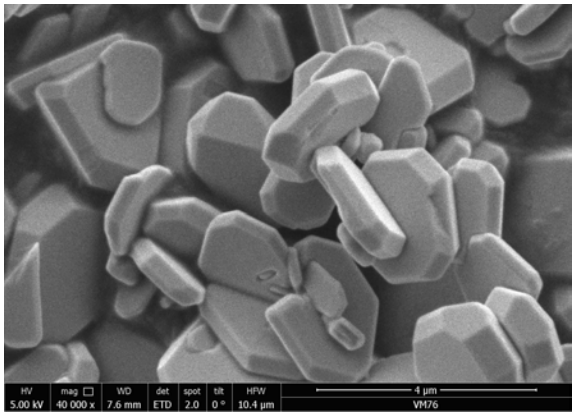

(c) 76-**0.08**-1.25-40

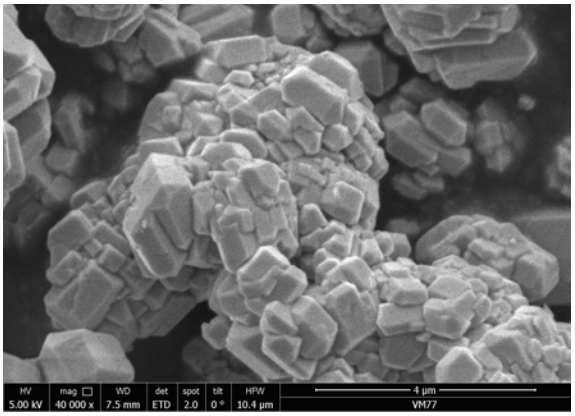

(d) 77-**0.125**-1.25-40

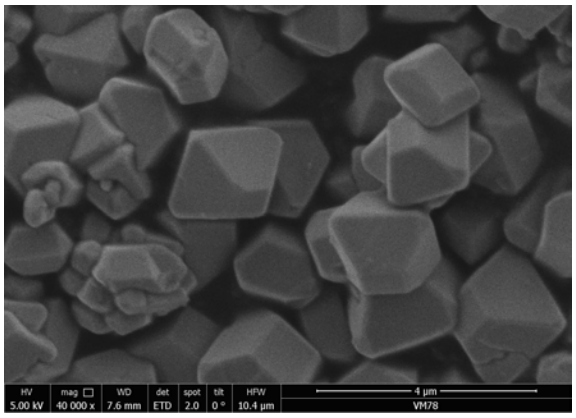

(e) 78-**0.45**-1.25-40

Figure 43: SEM images of $BiVO_4$ with the following notation: sample number-pH-precursor amount[mmol]-reaction time

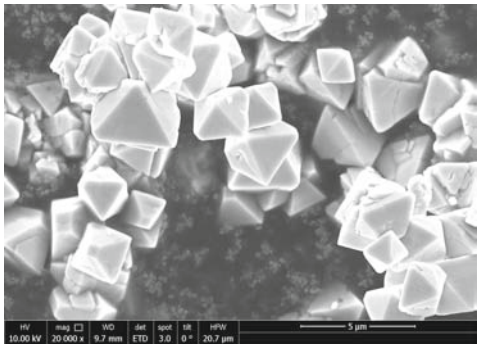

(a) 02-**0.88**-3.75

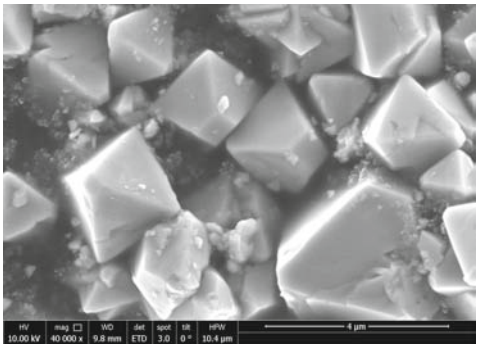

(b) 02-**0.88**-3.75-oven

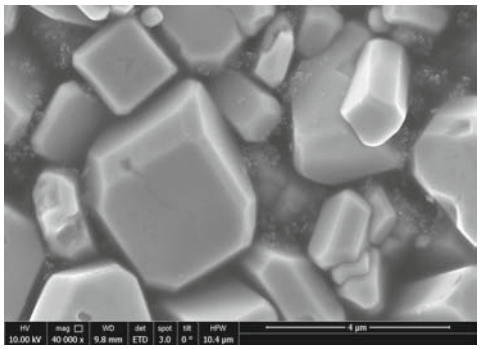

(c) 03-**0.88**-3.75

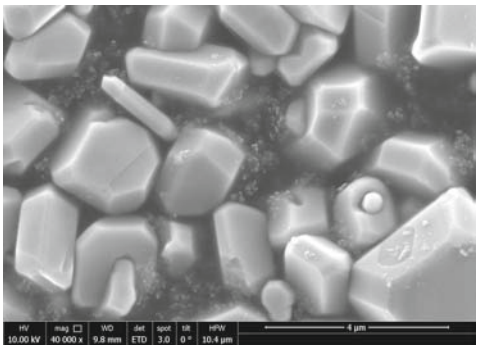

(d) 04-**0.88**-3.75

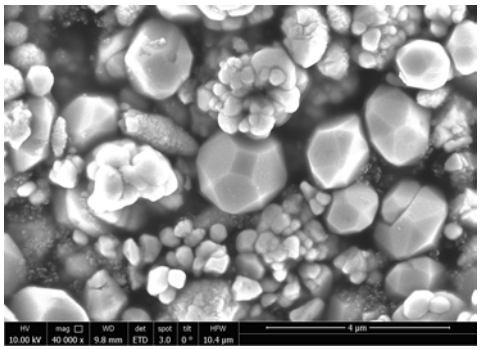

(e) 07-**1.076**-3.75

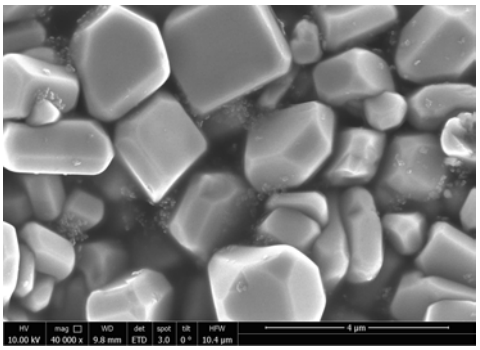

(f) 05-**1.4**-3.75

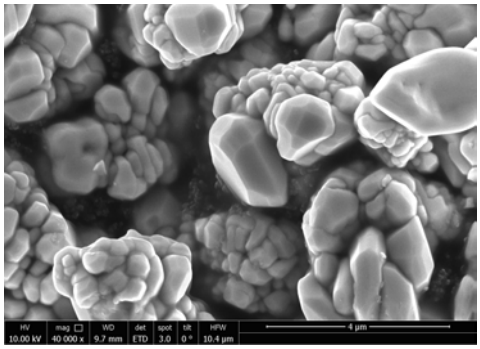

(g) 08-**0.88**-0.75

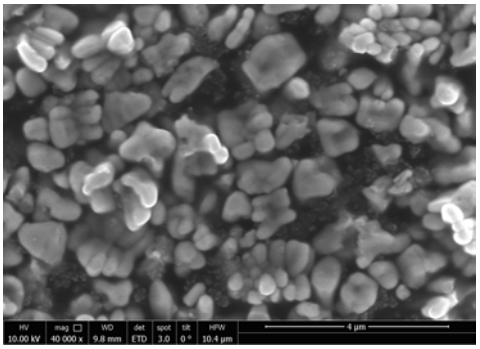

(h) 10-**1.4**-0.75

Figure 44: SEM images of $BiVO_4$ with the following notation: sample number-pH-precursor amount[mmol]

A.1.2 Optimization of the synthetic conditions

According to the results presented in section 3.1, sample 02 exhibited a well defined capped octahedron morphology, and this sample was chosen as 'reference material' for $BiVO_4$. The synthesis was repeated with the same conditions (precursor amount: 3.75 mmol; HNO_3: 0.16 mL; reaction time: 40 min; reaction temperature: 200 °C). Additionally another reference material was synthesised whereat the reaction volume and precursor concentration was $\frac{1}{3}$ of the samples mentioned above. Sample 29 and 30 shows a capped octahedron like morphology, with exposed 040 facet. However, the sample 29 possess a cluster like morphology, which consists of smaller octahedrons as well. The SEM image of the sample 38 shows, that the obtained powder is a cluster of smaller polyhedrons.

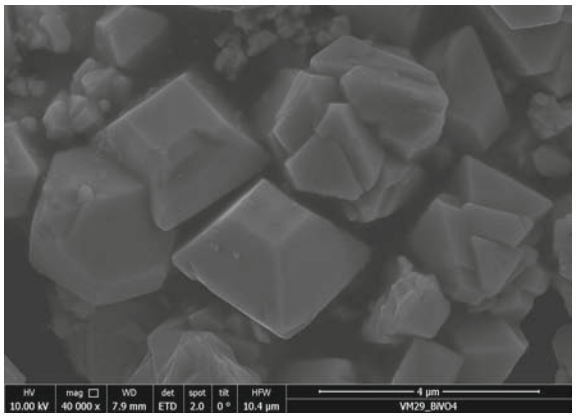

(a) 29-0.88-3.75-40

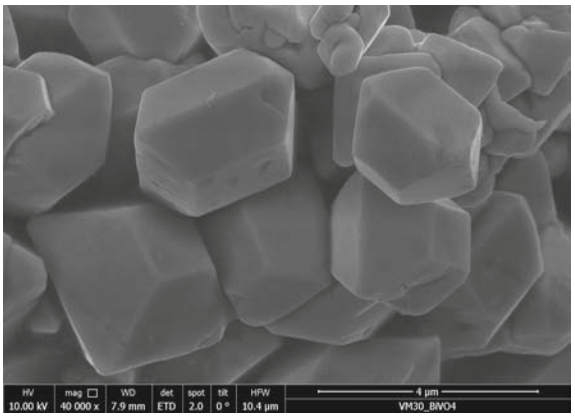

(b) 30-0.88-3.75-40

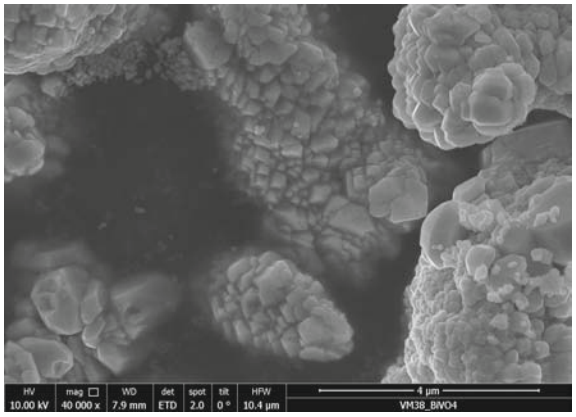

(c) 38-0.88-1.25-40

Figure 45: SEM images of $BiVO_4$ with the following notation: sample number-pH-precursor amount[mmol]-reaction time

A.1.3 Time variation

The synthesis of $BiVO_4$ with different microwave irradiation times was tried out. The synthesis details are shown in section 2.4.3. The samples with the sample number 43 and 44 were prepared at the microwave irradiation time of 2 minutes. Both of the samples resulted in capped octahedron morphology with well defined edges, of which the 040 facet is exposed. However, the SEM image of sample 44, reveal flat crystals with cut edges as well. The sample with the sample number 45, of which the microwave irradiation time was 4 minutes shows flat crystals with cut edges and polyhedron morphology as well. On the SEM image of the sample 69 and 71 octahedron shaped crystals, polyhedrons, as

well as a cluster of them are visible. The SEM image of the sample which was made at 10 minutes of microwave irradiation time shows capped octahedron morphology with exposed 040 facets. Sample 33 was prepared at 20 minutes of microwave irradiation time. On the SEM image of the as-prepared sample, a cluster of octahedrons is visible. The SEM image of the sample 32 which was prepared at 60 minutes of reaction time shows octahedron and polyhedron morphology.

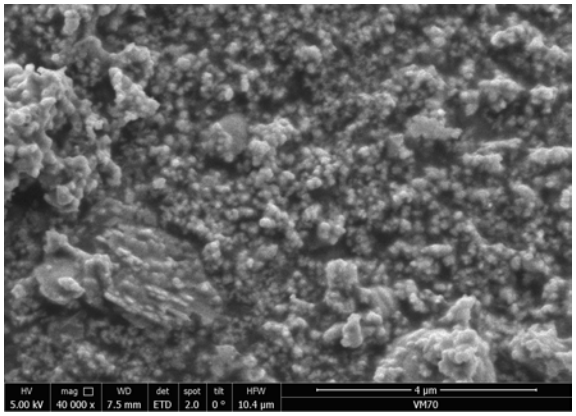

(a) 70-1.3-1.25-**0**

Figure 46: SEM images of the $BiVO_4$ obtained by coprecipitation of the precursors without microwave heating

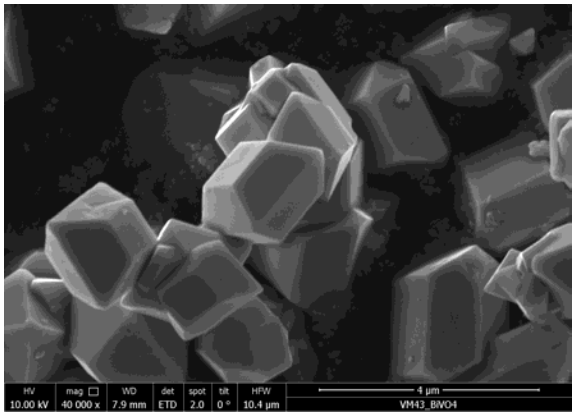

(a) 43-0.88-3.75-**2**

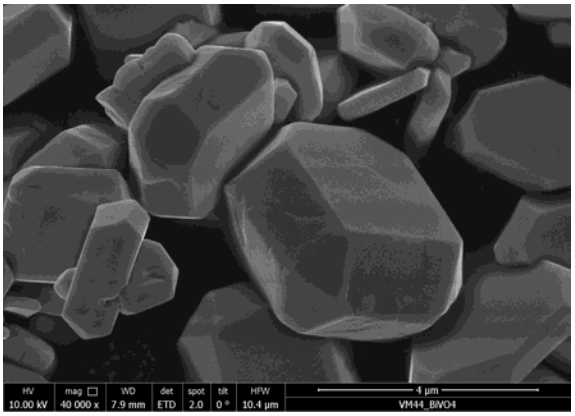

(b) 44-0.88-1.25-**2**

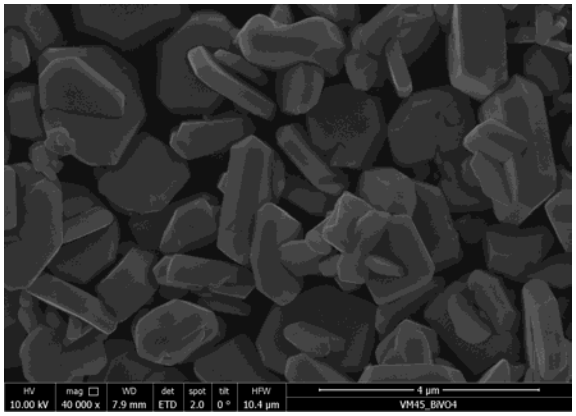

(c) 45-0.88-1.25-**4**

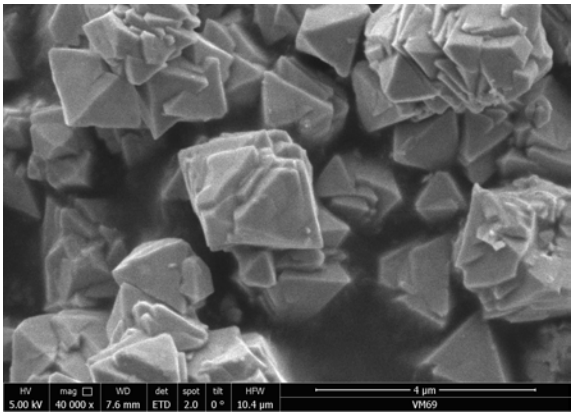

(d) 69-0.88-1.25-**6**

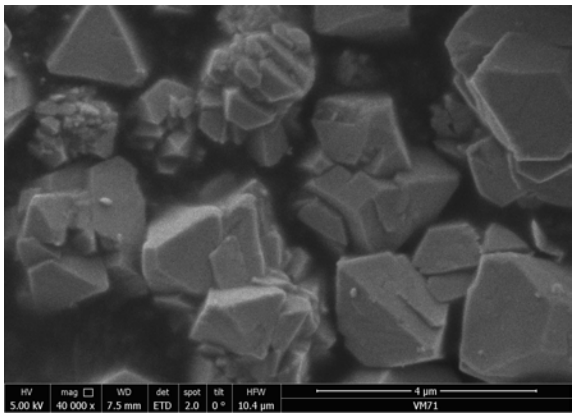

(e) 71-0.88-1.25-**8**

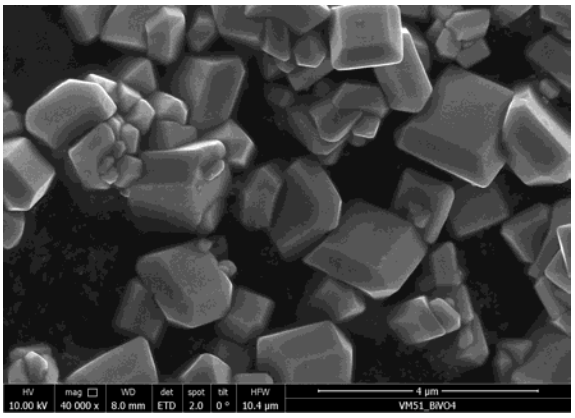

(f) 51-0.88-1.25-**10**

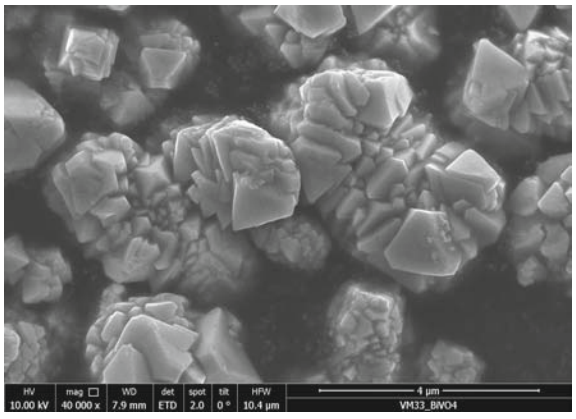

(g) 33-0.88-3.75-**20**

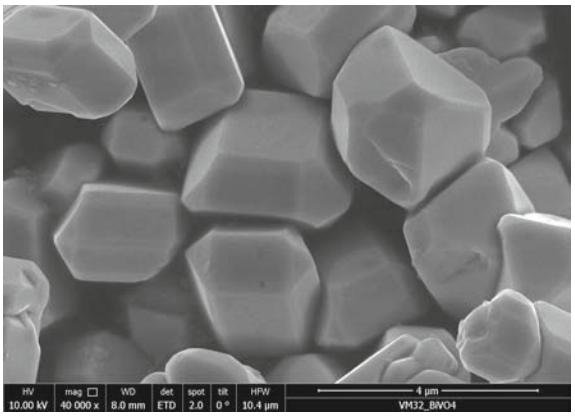

(h) 32-0.88-3.75-**60**

Figure 47: SEM images of $BiVO_4$ with the following notation: sample number-pH-precursor amount[mmol]-reaction time

A.1.4 Solvent variation

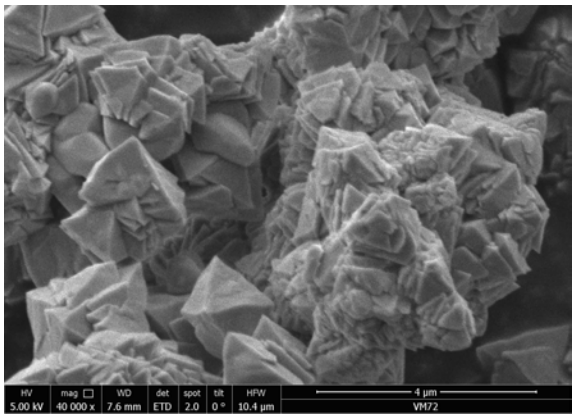

(a) 72-0.59-1.25-40-**0.01 EtOH**

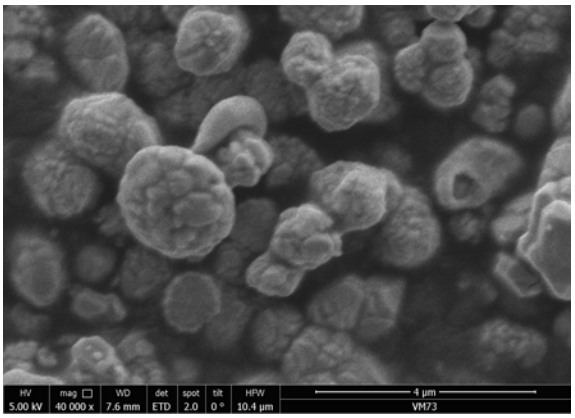

(b) 73-0.59-1.25-2-**0.05 EtOH**

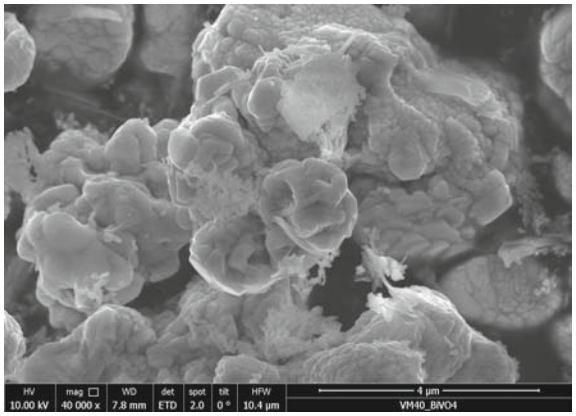

(c) 40-0.59-1.25-40-**0.25 EtOH**

(d) 41-0.59-1.25-40-**0.5 EtOH**

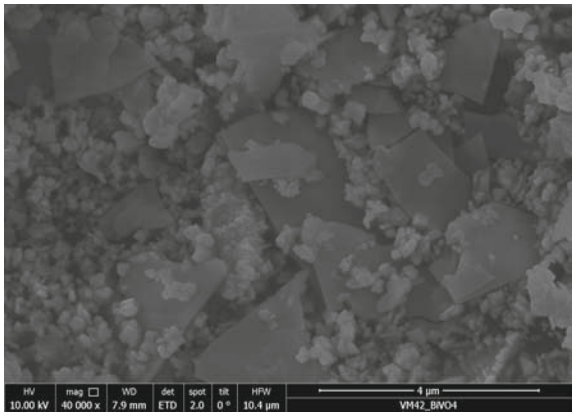

(e) 42-0.59-1.25-40-**0.75 EtOH**

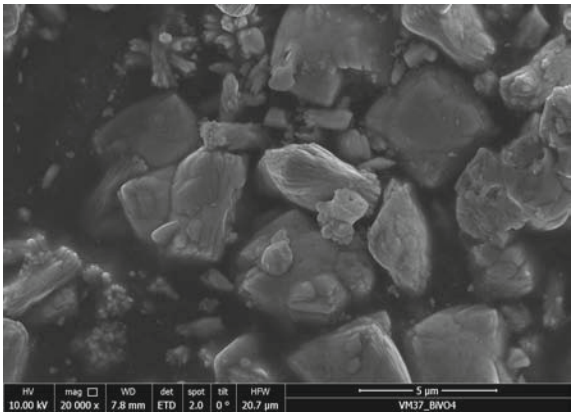

(f) 37-0.59-1.25-40-**1 EtOH**

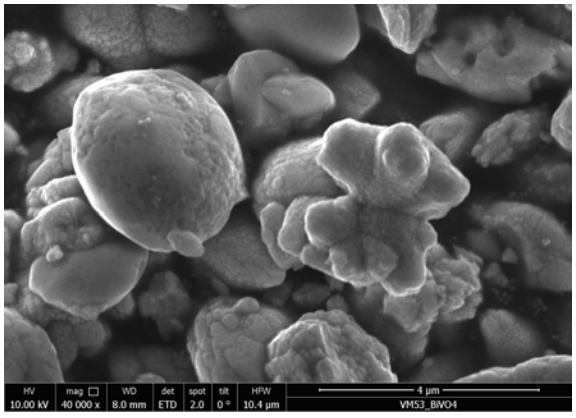

(g) 53-0.59-1.25-2-**0.25 EtOH**

Figure 48: SEM images of $BiVO_4$ with the following notation: sample number-pH-precursor amount[mmol]-reaction time- ethanol amount

A.1.5 Surfactant variation

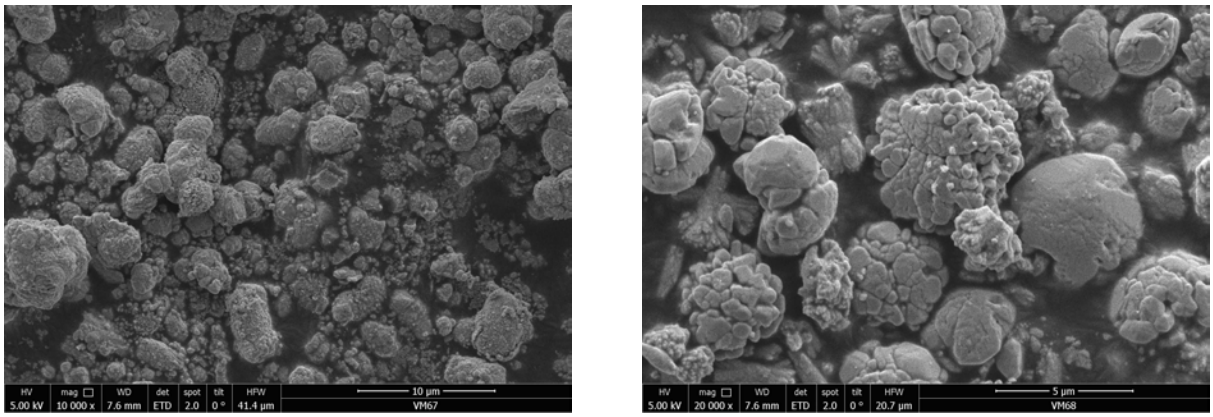

(a) 67-0.59-1.25-40-SDBS (b) 68-0.59-1.25-40-CTAB

Figure 49: Scanning electron microscopy of BiVO4, sample 67 shown in figure a) was prepared with the addition of SDBS, sample 68 shown in figure b) was prepared with the addition of CTAB

A.2 X-ray powder diffraction

A.2.1 Optimisation of the synthetic conditions

Figure 50 shows the X-ray powder diffractogram of the samples, which were prepared as reference material. The blask dashed line represents the peak positions of the reference diffractogram of monoclinic $BiVO_4$, whereat the red dashed line shows the peak positions of the reference diffractogram of tetragonal $BiVO_4$. In the diffractogram of sample 29 and 30 the peaks for monoclinic $BiVO_4$ are visible. However, the sample 31, which was prepared at the same conditions, resulted in tetragonal $BiVO_4$. Sample 38 was prepared by a $\frac{1}{3}$ reduced reaction volume and precursor amount compared to the samples mentioned above, which resulted in the same precursor concentration of 0.25 $\frac{\text{mol}}{\text{L}}$. At the synthesis of sample 38, monoclinic $BiVO_4$ was obtained. Sample 39 was synthesised with the same precursor concentration of 0.25 $\frac{\text{mol}}{\text{L}}$ but with a $\frac{1}{5}$ reduced volume and precursor amount compared to sample 29-31. The X-ray diffractogram of sample 39 show a mixed phase of monoclinic an tetragonal $BiVO_4$.

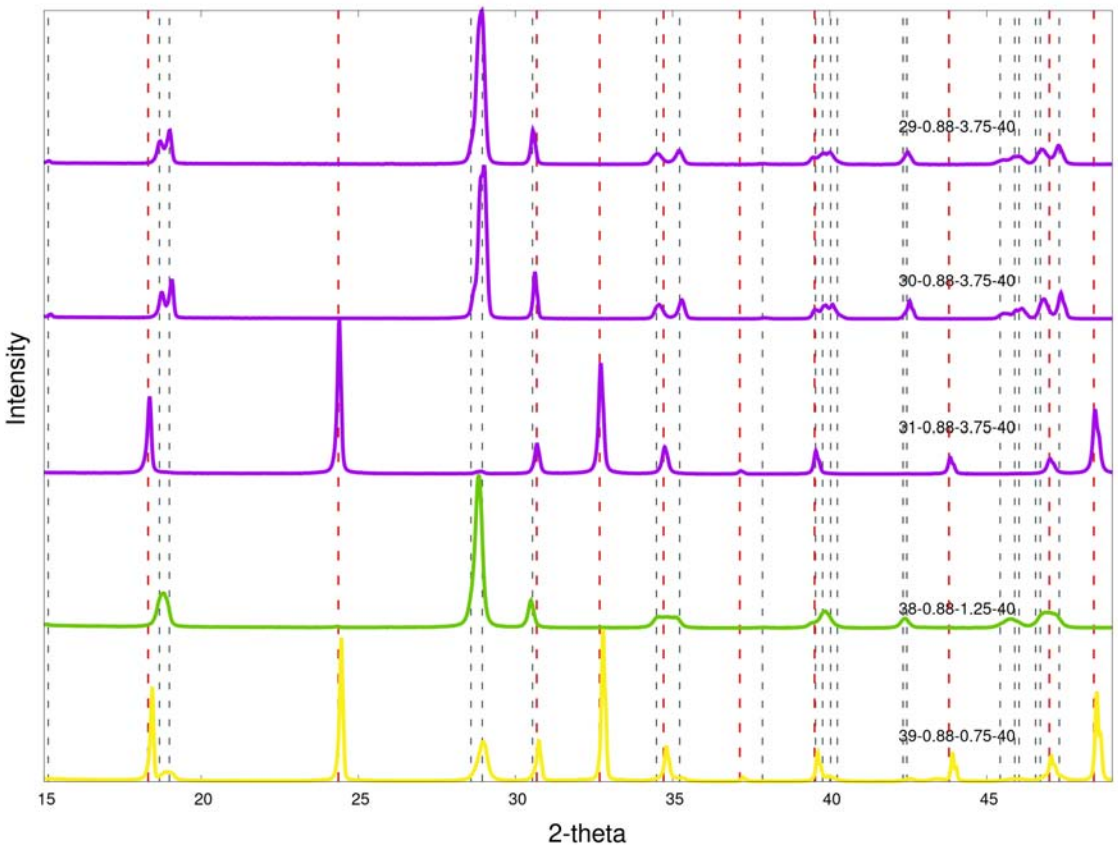

Figure 50: a) X-ray powder diffractogram of $BiVO_4$ with the following notation: sample number-pH-precursor amount [mmol]-reaction time [min]; black dashed line: m$BiVO_4$, red dashed line: zircon t$BiVO_4$

Table 25: Crystallite sizes calculated by the Sherrer equation using the highest intensity peak respectively

Sample number-reaction time	29-**40**	30-**40**	31-**40**	38-**40**	39-**40**
Crystallite size [nm]	58.95	50.41	61.26	29.46	25.21

A.2.2 Time variation

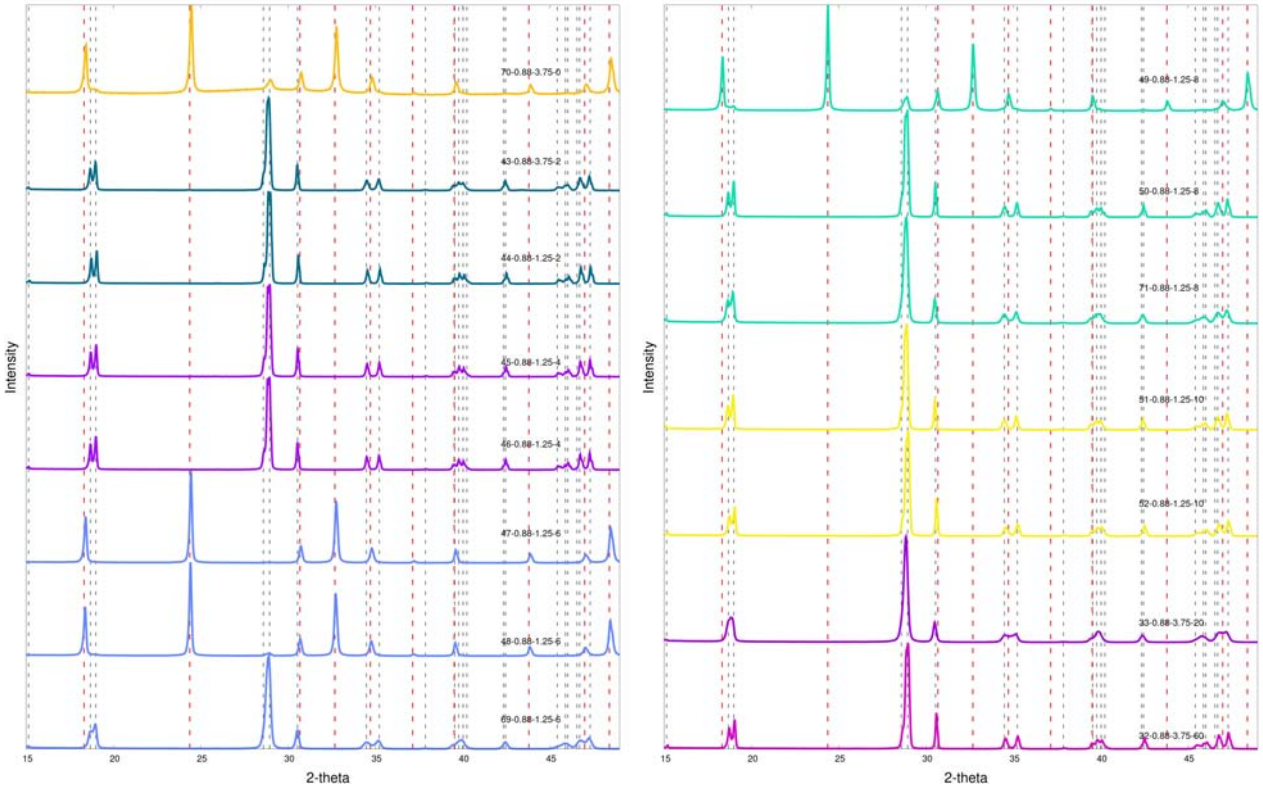

(a) (b)

Figure 51: a) X-ray powder diffractogram of $BiVO_4$ with the following notation: sample number-pH-precursor amount[mmol]-reaction time; black dashed line: $mBiVO_4$, red dashed line: zircon $tBiVO_4$

Table 26: Crystallite sizes calculated by the Sherrer equation using the highest intensity peak respectively

Sample number-reaction time	70-**0**	43-**2**	44-**2**	45-**4**	46-**4**	47-**6**	48-**6**	69-**6**
Crystallite size [nm]	25.84	62.93	125.93	65.87	94.41	73.86	63.28	25.84

Table 27: Crystallite sizes calculated by the Sherrer equation using the highest intensity peak respectively

Sample number-reaction time	49-**8**	50-**8**	71-**8**	51-**10**	52-**10**	33-**20**	32-**60**
Crystallite size [nm]	73.82	65.85	25.86	57.64	76.77	29.45	48.32

A.3 UV-Vis Diffuse reflectance spectroscopy

A.3.1 Optimization of the synthetic conditions

The UV-Vis diffuse reflectance spectra of the samples which were prepared at the same pH and same irradiation time were measured. The absorption spectra of the as-prepared samples with the sample

number 29, 30, 31, 38 and 39 are shown in figure 52. The samples with the sample number 29, 30 and 38 show absoprtion at 400-500 nm. The samples with the sample number 31 and 39 show a step like absorption in the region of 420-500 nm. According to the X-ray powder diffractogram of the samples 31 and 39, which is shown in section A.2.1, the UV-Vis diffuse reflectance spectra stands in correlation with the previous findings. Sample 31 was evaluated as tetragonal $BiVO_4$, sample 39 was evaluated as a mixed phase of monoclinic and tetragonal $BiVO_4$.

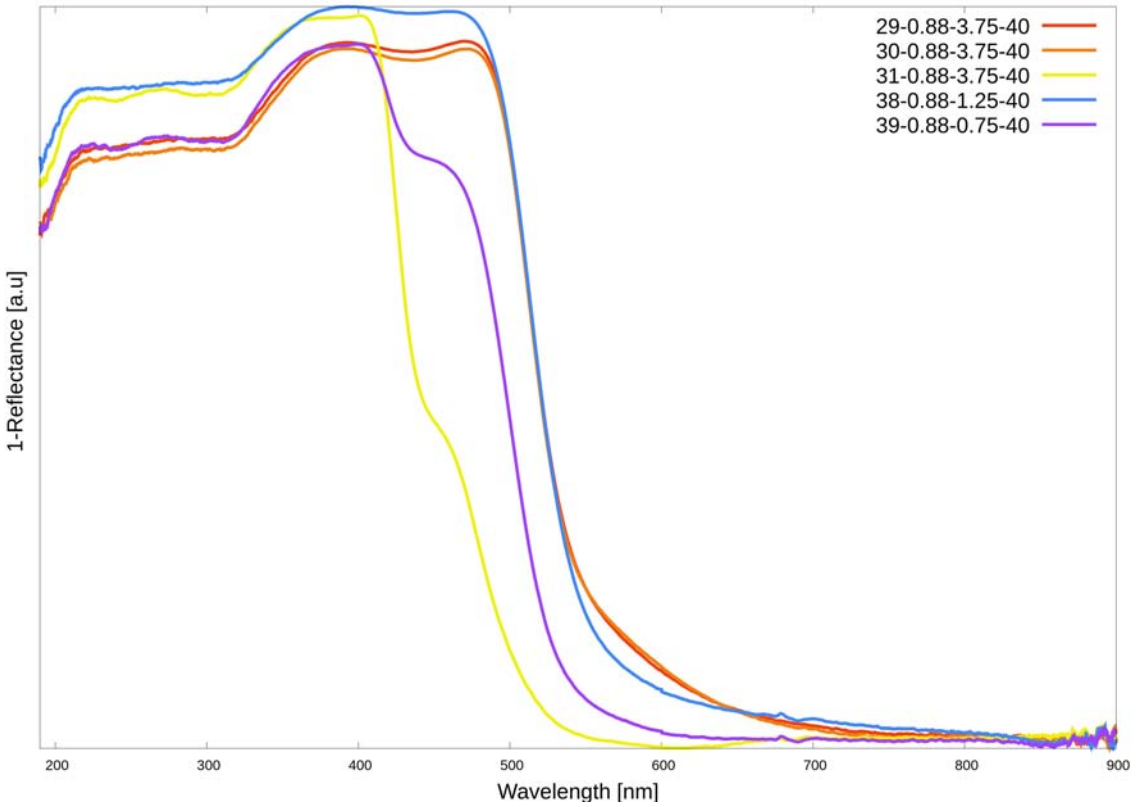

Figure 52: Diffuse reflectance spectra of $BiVO_4$ with the following notation: sample number-pH-precursor amount[mmol]-reaction time

Table 28: band gaps of the $BiVO_4$ samples estimated by the Tauc method

Sample number	**29**	**30**	**31**	**38**	**39**
band gap [eV]	2.39	2.39	2.514	2.41	2.43
			2.88		2.75

Table 29: Summary of the results discussed for the optimisation of the synthesis for the samples with the number 29-31, 38 and 39

Sample number	Morphology	Size [µm]	Polymorph	Crystallite size [nm]	Band gap [eV]	Oxygen evolution activity [µmol/h]
29	capped octahedron with exposed 040 facets + cluster of octahedron	3	m	58.95	2.39	0.305
30	capped octahedron with exposed 040 facets	3	m	50.41	2.39	0.234
31	-	-	t	114	2.514; 2.88	0.0205
38	cluster of smaller octahedrons	10	m	29.46	2.39	0.174
39			m+t	25.21	2.48; 2.86	0.09

A.3.2 Time variation

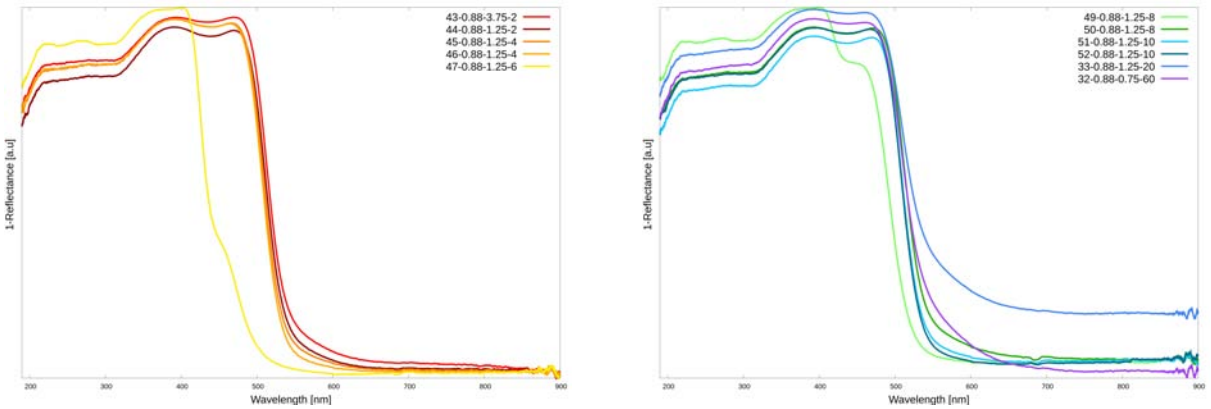

(a) (b)

Figure 53: Diffuse reflectance spectra of $BiVO_4$ with the following notation: sample number-pH-precursor amount[mmol]-reaction time

Table 30: Estimated band gaps of $BiVO_4$

Sample number	**70**	**43**	**44**	**45**	**46**	**47**	**48**	**69**
band gap [eV]	2.4	2.4	2.4	2.42	2.43	2.53 2.88	2.5 2.86	2.39

Table 31: Estimated band gaps of $BiVO_4$

Sample number	**49**	**50**	**71**	**51**	**52**	**33**	**32**
band gap [eV]	2.49 2.8	2.39	2.38	2.4	2.42	2.38	2.39

Table 32: Summary of the results discussed in section 3.2 for the samples for which different microwave irradiation times were tried out

Sample number	Morphology	Size [µm]	Polymorph	Crystallite size [nm]	Band gap [eV]	Oxygen evolution activity [µmol/h]
70	irregular shaped particles + clusters of particles	particles: few nm; clusters: 2 µm	m+t	25.84	2.4	0.53
43	capped octahedron with exposed 040 facets	2	m	62.93	2.4	0.817
44	capped octahedron with exposed 040 facets	3-4	m	125.93	2.4	1.638
45	flat crystals with cut edges + polyhedron	2	m	65.87	2.42	1.507
46	capped octahedron + cluster of smaller particles	2	m	94.41	2.43	0.9
47	sphere shaped cluster consisting of smaller particles	2-3	t	73.86	2.53; 2.88	0.263
48	-	-	t	63.28	2.5; 2.86	0.21
69	cluster of octahedron	2	m	25.84	2.39	
49	sphere shaped cluster consisting of smaller particles	3-4	m+t	73.82	2.49; 2.8	0.307
50	capped octahedron + cluster of smaller particles	3-4	m	65.85	2.39	0.753
71	cluster octahedron	2	m	25.86	2.38	
51	capped octahedron with exposed 040 facets	2	m	57.64	2.4	0.929
52	capped octahedron + irregular shaped particles	1-2	m	25.21	2.42	1.645
33	cluster of octahedron	4	m	29.45	2.38	0.213
32	octahedron + polyhedron	3-4	m	48.32	2.39	0.65

B $NiFe_2O_4$

B.1 Structure $NiFe_2O_4$ and electronic properties

Nickel ferrite ($NiFe_2O_4$) exhibits ferrimagnetic nature with a Curie temperature=858K. The nickel ferrites adopt an inverse spinel structure in which oxygen atoms forms a face centered cubic lattice. Half of the Fe^{3+} ions occupy tetrahedral(T_d) sites and the remaining ions occupy the octahedral(O_h) sites.[153] Thus, the compound can be represented by the formula $[Fe^{3+}]_A$ $[Ni^{2+}Fe^{3+}]_B$ $[O^{2-}]_4$, where A and B represent tetrahedral and octahedral sites, respectively.[154] The complete structure crystallizes in a cubic system Oh^7 space group 227; as shown in figure 56 a) oxygen atoms occupy the 32e positions, Fe(T_d) atoms occupy the 8a ones and the Ni(O_h) and Fe(O_h) atoms are distributed on the 16d position.[155] The arrangements of the magnetic moment are ↑ ↓ ↑ for Ni(O_h), Fe(T_h) and Fe(O_h) respectively. The iron atoms are antiparallel in the octahedral and tetrahedral sites, therefore the total magnetic moment of $NiFe_2O_4$ is mainly due to the nickel atoms.[156] The magnetic moment meas-

ured is between 1.5 and 2.4 μ_B.[157] Bouferrache et al. performed self-consistent calculations within the framework of DFT for the properties of the inverse spinel $NiFe_2O_4$ compound. The increase in the accuracy of the calculations was assured by implementing the DFT+U method, which includes the Hubbard parameter to account for the presence of 'd' orbitals of both Ni and Fe atoms.[156] The theoretical method proposed by Madsen[158] and Anisimov[159] allows the direct calculation of the Hubbard parameter U for both Ni and Fe atoms in both octahedral and tetrahedral sites. They found that U exhibits the following values: $U(Fe_{Tetra})$=6.569 eV, $U(Fe_{Octa})$=6.961 eV, $U(Ni_{Octa})$=5.469 eV, $U(Ni_{Tetra})$=5.107 eV.

The calculations of the total energies as a function of volume in antiferromagnetic, ferromagnetic, ferrimagnetic and paramagnetic states of the spinel $NiFe_2O_4$ in the inverse case calculated with GGA+U approximation reveals, that the ferrimagnetic compound is the most stable as shown in figure 54[156]

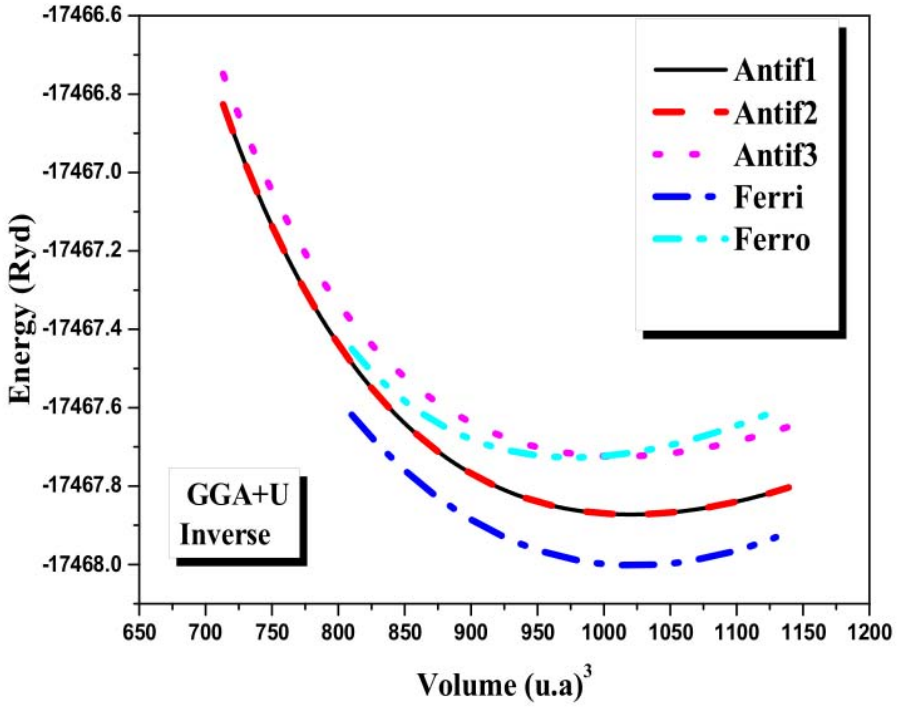

Figure 54: Calculations of the total energies as a function of volume in antiferromagnetic, ferromagnetic, ferrimagnetic and paramagnetic states of the inverse spinel $NiFe_2O_4$[156]

By implementing the mBJ+U approximation, the inverse spinel $NiFeO_4$ compound in the majority spins(↑) has a semiconductor character with the valence band maximum located along the direction Λ-Γ and the conduction band minimum situated along the direction W-L, while for the minority spins(↓) the compound also has a semiconductor character, with valence band maximum located at point Γ and conduction band minimum placed along the direction Λ-Γ as shown in figure 55.

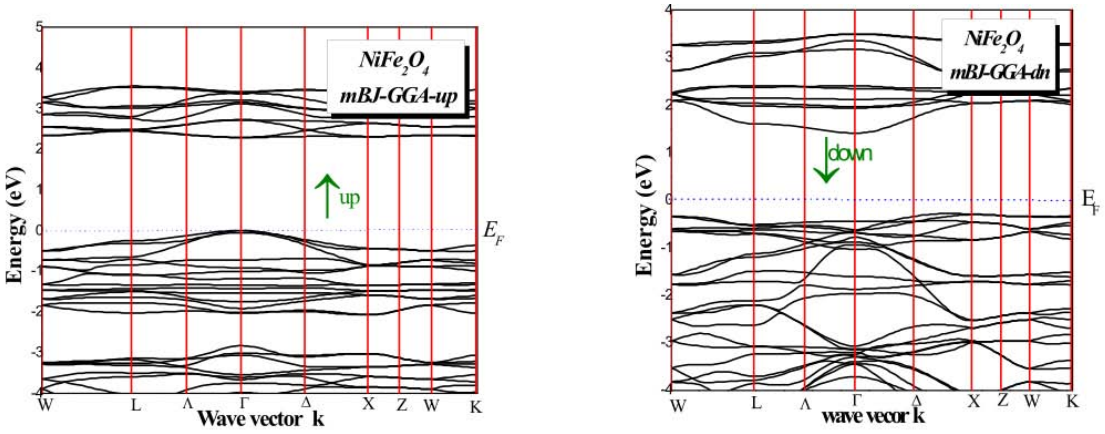

Figure 55: The band structure of the inverse spinel $NiFe_2O_4$ compound calculated with the mBJ+U approximation

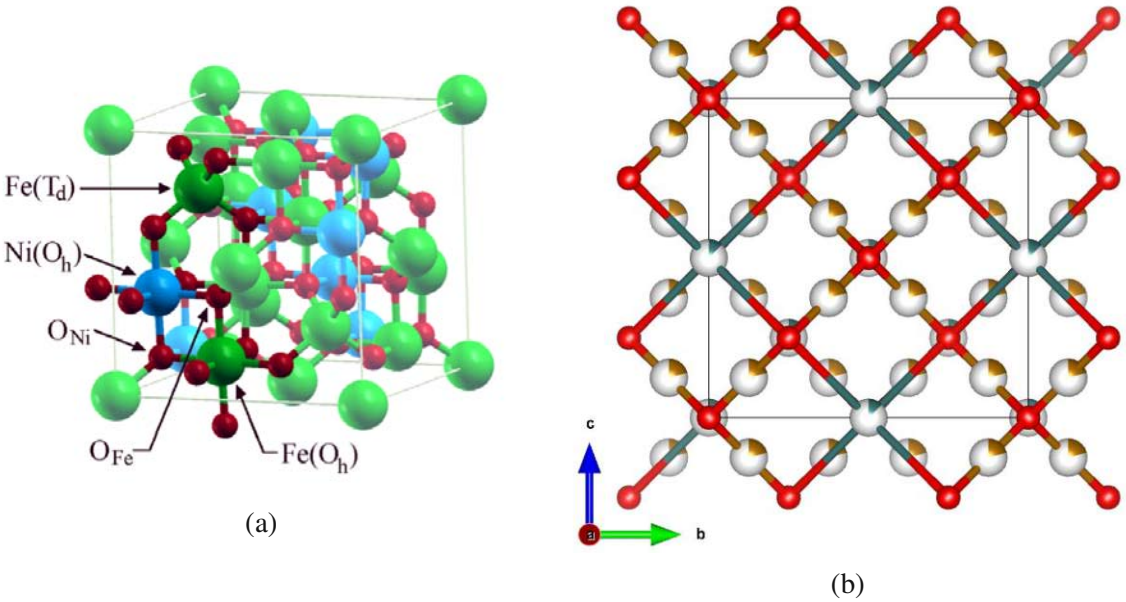

(a) (b)

Figure 56: a) Structure of $NiFe_2O_4$ Perron et al.[155]; VESTA visualisation of $NiFe_2O_4$

The structure, electronic properties, and energetics of the $NiFe_2O_4$ 001 surface and its interaction with water both in the absence and in the presence of surface oxygen vacancies have been studied using DFT+U.[160] It was shown that water adsorbs dissociatively on the surface oxygen vacancies leading to the formation of surface hydroxyls. Furthermore, it was found that at high temperature, water desorbs leaving a surface containing oxygen vacancies. The reactivity of the $NiFe_2O_4$ 111 surface has been studied using DFT+U.[161] Dissociation of water was found to be highly favorable on the $NiFe_2O_4$ 111 surfaces. The activation barrier for the dissociation of a single water molecule was dependent on the termination of the surface.[162] Adsorption energies of oxygen adatoms located on exposed cation sites were calculated on hybrid-DFT (B3LYP) level of theory. The computed energies vary proportionally to the number of oxygen atoms missing from the normal octahedral coordination of the cation adsorption sites. A theoretical investigation of bare and water terminated $NiFe_2O_4$ surfaces was carried out in 2014 using GGA+U.[163] It was found that surfaces that have

more metal cations exposed are more stable. The most stable surfaces are shown to be along the (111) planes. Water adsorption on the $NiFe_2O_4$ surfaces was found to be an exothermic process. In 2014, a DFT investigation of the $NiFe_2O_4$ 001 surface reported an overpotential of 0.42 V for the OER.[162]

B.2 Scanning electron microscopy

B.2.1 Time and temperature dependent synthesis

The synthesis of $NiFe_2O_4$ was carried out at pH 9.5 and pH 10 with different microwave irradiation times and temperatures. The synthesis details of these samples, with the sample number 54-66 are described in the section 2.5.2. The SEM image of the sample 65 is shown in figure 57 a). The sample 65 was prepared with the addition of iron and nickel chlorides instead of the nitrates. On the figure 57 it is visible, that sample 65 consists of smaller particles in the nm range and clusters of particles in the µm range. The sample 66 was prepared with the addition of the iron and nickel nitrates as a precursor. After the microwave synthesis, this sample was annealed in the oven at 600 °C for 1 hour. The SEM image of the as-prepared sample is shown in figure 57 b). The SEM image reveals a cluster of particles with the size of approximately 5 µm and smaller particles in the nanometer range is well.

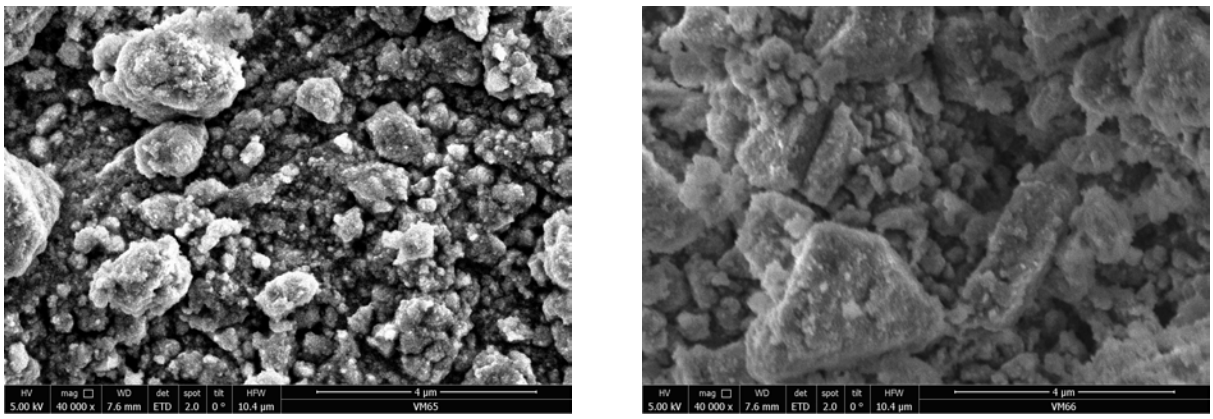

(a) 65-9.5-220-60; $FeCl_3$ precursor (b) 66-9.5-220-60

Figure 57: SEM images of NiFe2O4 with the following notation: sample number-pH-reaction temperature-reaction time

B.3 X-ray powder diffraction

B.3.1 pH dependent synthesis

The synthesis of $NiFe_2O_4$ at different pH values and the same microwave irradiation time and temperature of 180 °C was tried out. The synthesis details of these samples are described in section 2.5.1. The X-ray powder diffractograms of the as-prepared samples are shown in figure 58. The red dotted line represents the peak positions of the reference diffractogram of $NiFe_2O_4$, whereas the black dashed line represents the peak positions of Fe_2O_3. According to the X-ray powder diffractogram of the sample 18, 26-28, the peak positions of these samples are ambiguous, therefore an amorphous character is assumed. The peak at approximately 62.5 2Θ, which is at the reference position of Fe_2O_3 could be an indicator, that the synthesis of the samples 18, 26-28 resulted in Fe_2O_3 with an amorphous character. Compared to the above mentioned samples, the samples with the number 20-25 are more

crystalline. Furthermore their peak positions correlate with the positions of the reference $NiFe_2O_4$. That is why it is assumed, that the synthesis of $NiFe_2O_4$ was successful for the samples 20-25.

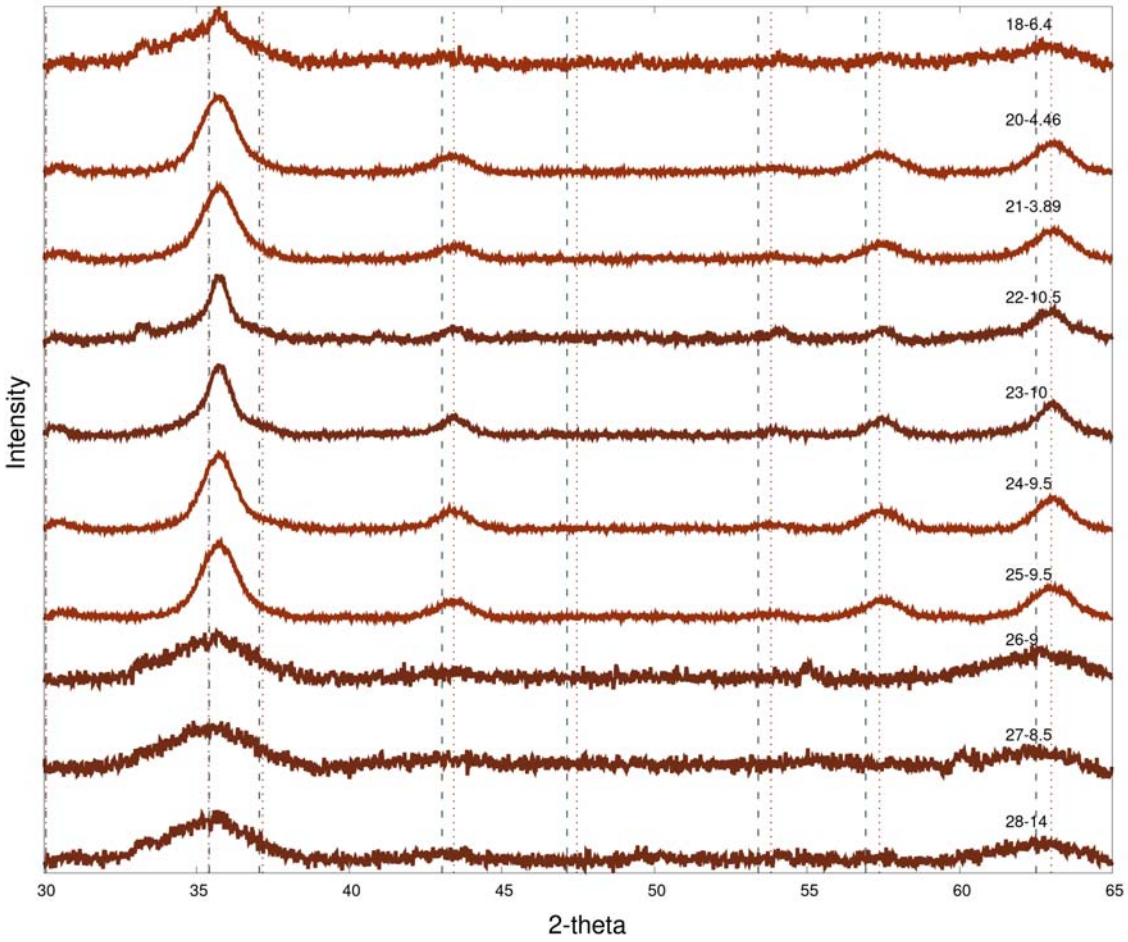

Figure 58: XRD diffractograms of $NiFe_2O_4$ which were synthesised under microwave irradiation at 180 °C 30 min. Notation: sample/,number-pH. Red dotted line: reference for $NiFe_2O_4$, black dashed line Fe_2O_3

B.3.2 Time and temperature dependent synthesis

The synthesis of $NiFe_2O_4$ at the pH value of 9.5 and 10 with different microwave irradiation times and temperatures were tried out. The synthesis details are shown in section 2.5.2. The X-ray powder diffractograms of the as-prepared samples are shown in figure 59. The red dotted line represents the peak positions of the reference X-ray powder diffractogram of $NiFe_2O_4$. The black dashed line represents the reference of Fe_2O_3. According to figure 59 the synthesis of the samples 64-66 were successful for $NiFe_2O_4$, because their peak positions are in the same position as the reference $NiFe_2O_4$. The other samples with the number 56-63 resulted in amorphous material with ambiguous peaks. The sample 54 and 55 was identified by means of their X-ray powder diffractogram via Highscore XRD analysis software and it could be assigned to $Fe_{1.987}O_3$ according to Mitra et al[164]. According to the matches of the Highscore X-ray analysis software the peaks of the diffractogram of sample 54 and 55 are identical with the peaks of $Fe_{1.83}O_{2.5}(OH)_{0.5}$ [165].

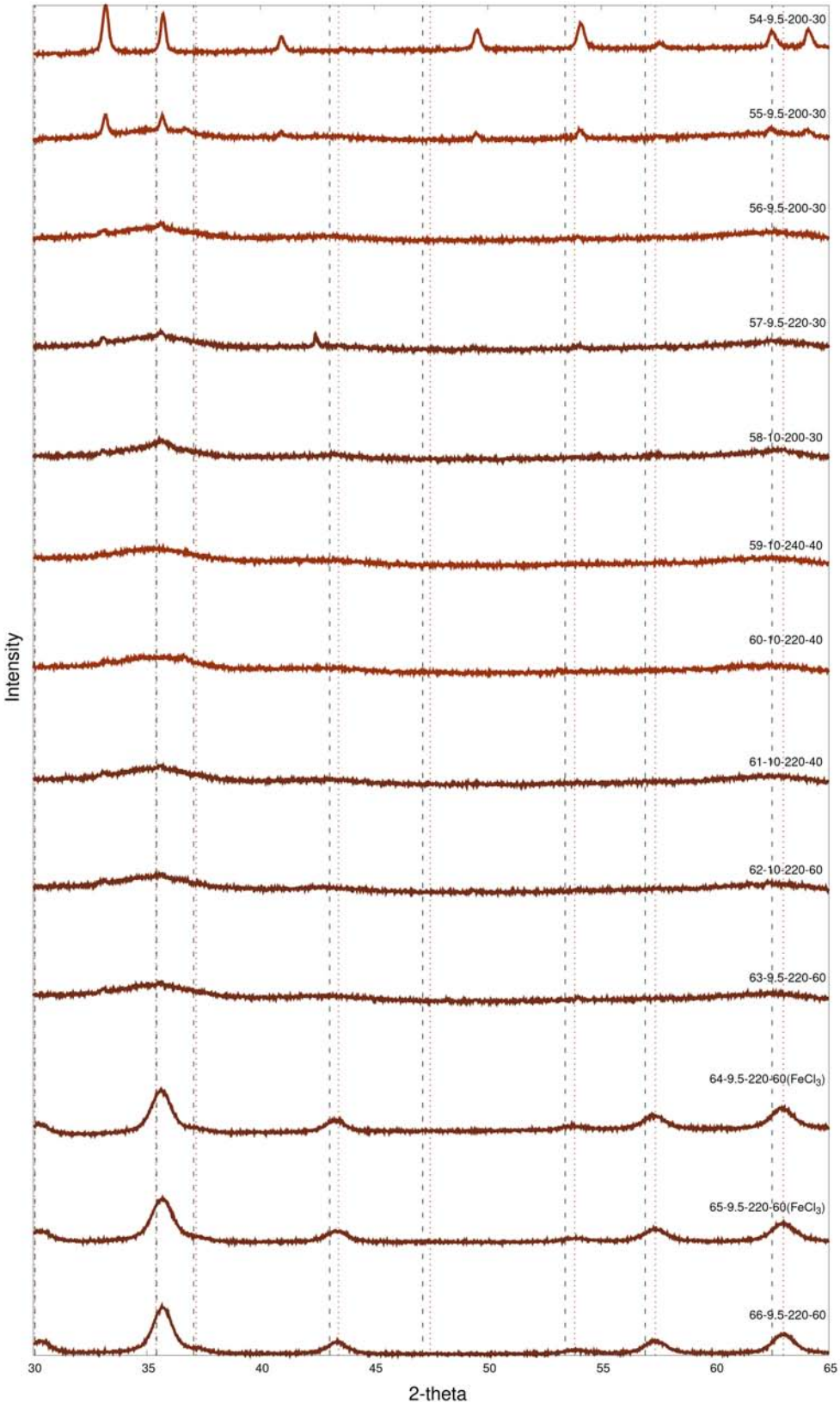

Figure 59: XRD diffractograms of $NiFe_2O_4$ which were. Notation: sample/,number-pH-reaction temperature-reaction time. Red dotted line: reference for $NiFe_2O_4$, black dashed line Fe_2O_3

The sample 66, which was prepared with the microwave irradiation time of 60 minutes and 220 °C was further annealed for 1 hour at 600 °C. The X-ray powder diffractogram of the unannealed and annealed sample 66 is shown in figure 60. There is no significant recognisable difference in the two diffractograms shown in figure 60.

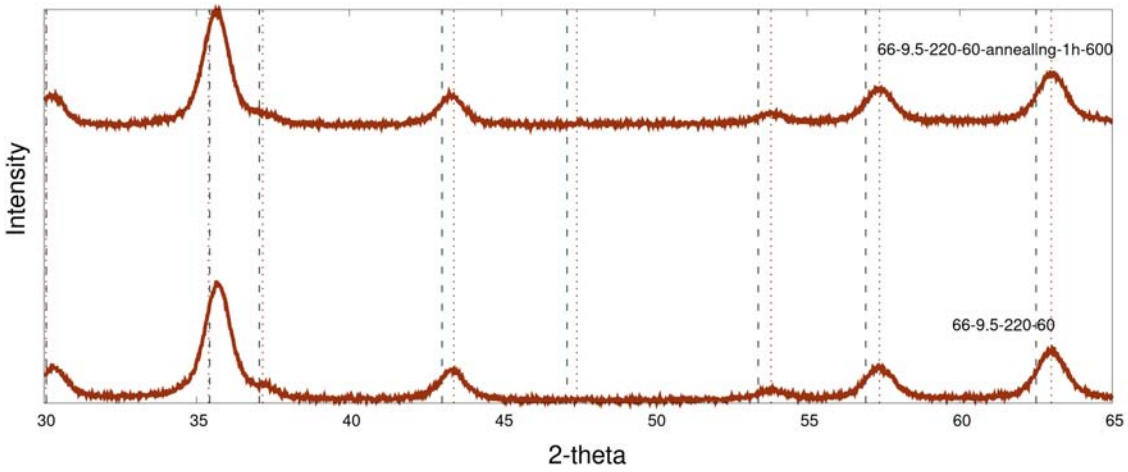

Figure 60: XRD diffractograms of $NiFe_2O_4$ which were. Notation: sample/,number-pH-reaction temperature-reaction time. Red dotted line: reference for $NiFe_2O_4$, black dashed line Fe_2O_3

B.4 UV-Vis Diffuse reflectance spectroscopy

B.4.1 pH dependent synthesis

The UV-Vis absorption spectra of the $NiFe_2O_4$ samples with the number 18, 20-28 was obtained, and is shown figure 61. These samples were prepared at different pH values and their exact synthesis details are described in section 2.5.1. The UV-Vis diffuse reflectance spectra of the samples 18, 21, 26-28 show a similar absorption curve, with a step like absorption in the range of approximately 720-780 nm. The samples which were evaluated as $NiFe_2O_4$ according to the X-ray powder diffractogram in section B are numbered with the sample number 20-25. On the UV-Vis diffuse reflectance spectra of the samples 20, 21, 23, 24 and 25 an absorption peak at approximately 750 nm is visible. According to previous findings of various research groups, namely Shetty et al.[153], Hong et al.[166] and Ortiz-Quinonez et al.[167], the absorption band at approximately 750 nm is characteristic for the crystalline spinel $NiFe_2O_4$.[166] The shoulder peak can be attributed to the d–d transition from Ni3d-t_{2g} to Ni3d-e_g.[128,168] It is well known that $NiFe_2O_4$ is characterized by a normal spinel structure in which Ni^{2+} and Fe^{3+} occupy the tetrahedral and octahedral sites of the cubic spinel lattice.[169] The energy band structures of $NiFe_2O_4$ are generally defined by considering the O2p orbital as the valence band and the hybridized Fe3d orbital as the conduction band.[156] The Fe-containing spinel oxides possess a high absorptivity in the range of 400–700 nm because of an intrinsic transition between valence band and conduction band.[170,171]

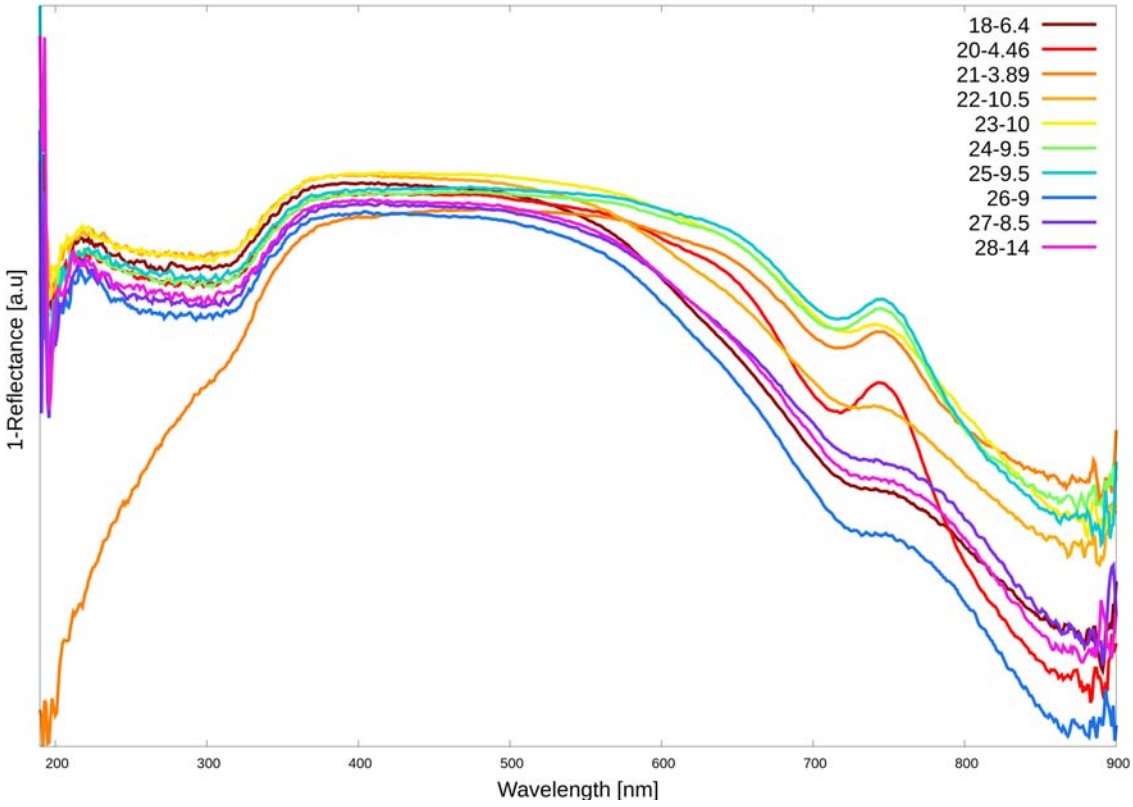

Figure 61: Uv-Vis Diffuse reflectance spectra of $NiFe_2O_4$ with the following notation: sample number-pH

The band gap of the $NiFe_2O_4$ was estimated by extrapolating the linear region of the Tauc-plot whereat the absorbance multiplied by the energy squared is plotted against the energy as seen in figure 62. The estimated band gap values are shown in table 33 Hussain et al. reported a band gap of 2.1 eV for Fe_2O_3 and 1.77 eV for $NiFe_2O_4$.[172] The evaluated band gaps of the samples 20, 21, 23, 24 and 25 are in the range of 1.67-1.72. Furthermore the Tauc-plot of the mentioned samples show a peak at approximately 1.65 eV as shown for sample 25 in figure 62. It is assumed, that the samples with the number 20, 21, 23, 24 and 25 are $NiFe_2O_4$. The band gapvalues of sample 18, 22, 26, 27 and 28 are greater than 1.84 eV, and in their Tauc-plot a smooth graph is visible as for sample 18 shown in figure 62. It is presumed, that the samples with the number 18, 22, 26, 27 and 28 is Fe_2O_3.

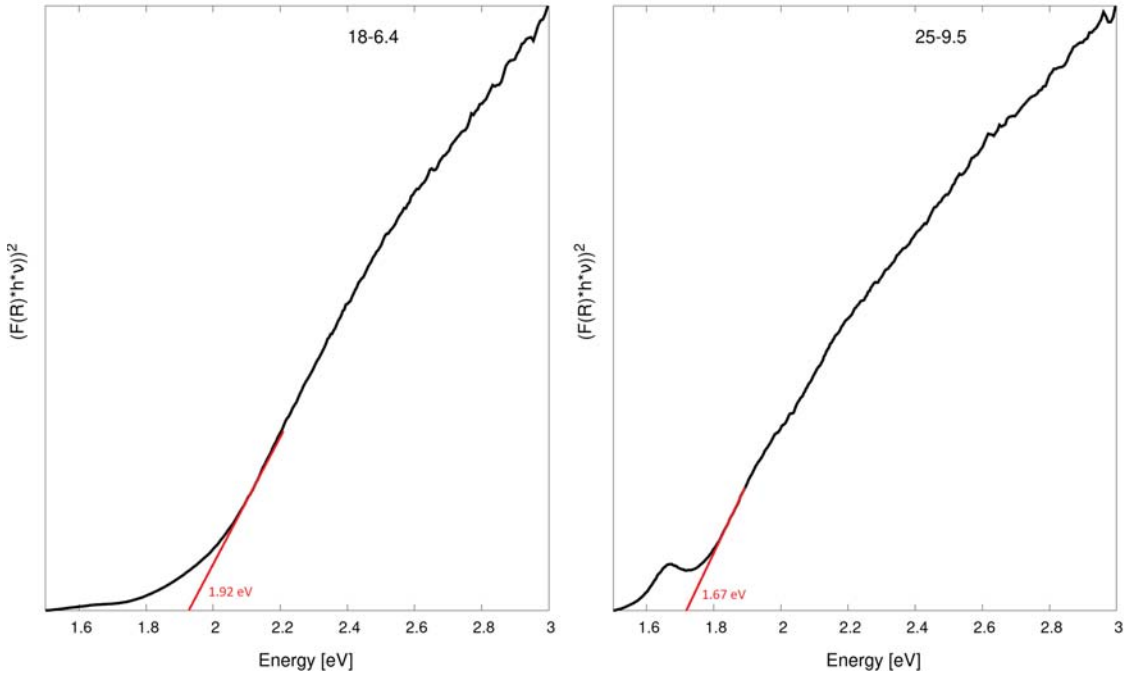

Figure 62: Tauc plot of $NiFe_20_4$ with the following notation: sample number-pH

Table 33: Estimated band gaps of $NiFe_2O_4$

Sample number	**18**	**20**	**21**	**22**	**23**	**24**	**25**	**26**	**27**	**28**
band gap [eV]	1.92	1.78	1.7	1.88	1.72	1.69	1.67	1.87	1.84	1.85

B.4.2 Time and temperature dependent synthesis

The synthesis of $NiFe_2O_4$ was carried out at different microwave irradiation times and temperatures. The synthesis details of these samples with the sample number 54-66 are described in the section 2.5.2. The UV-Vis diffuse reflectance spectra of the samples 55-66 was measured, and is shown in figure 63. The absorption curve of the samples 64-66 shows a pronounced absorption peak at approximately 750 nm. The sabsorption curve of sample 62 and 63 shows a slight absorption band at 750 nm, which is characteristic for the $NiFe_2O_4$, according to previous reports.[153,166,167] The absorption band at 750 nm is originating from the d–d transition from Ni3d-t_{2g} to Ni3d-e_g.[128,168]

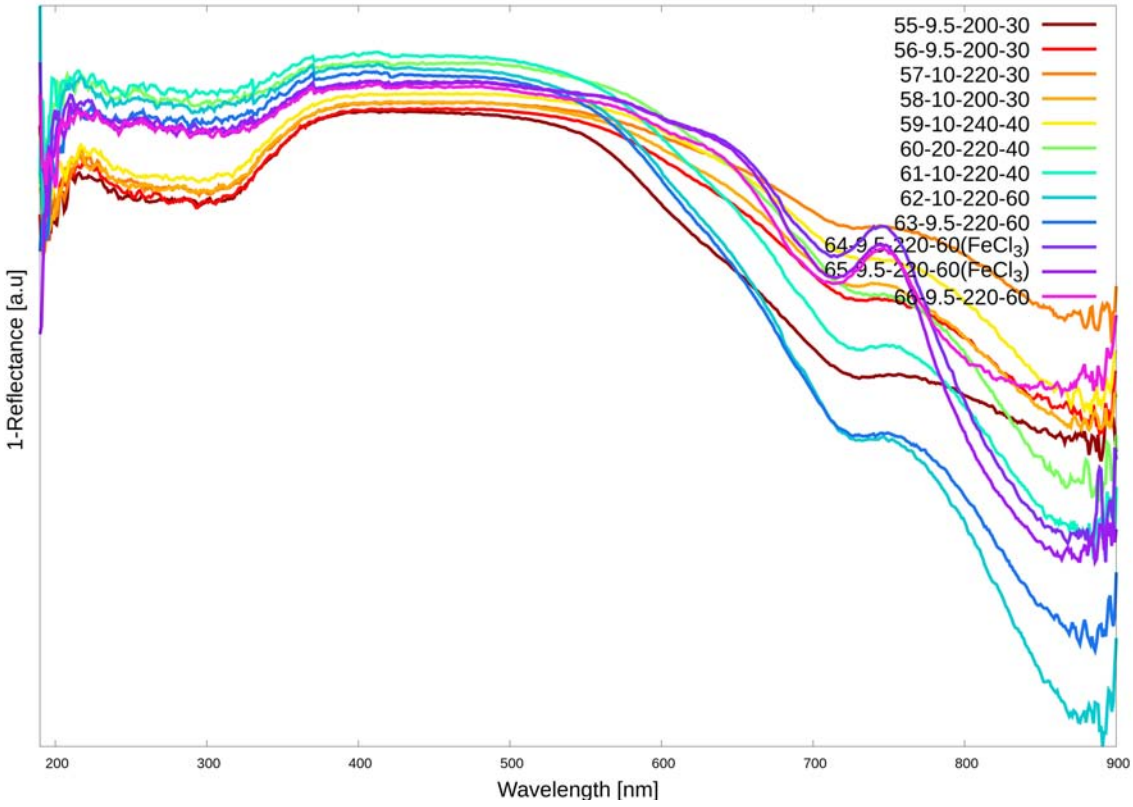

Figure 63: Diffuse reflectance spectra of $NiFe_2O_4$ with the following notation sample number-pH-reaction temperature-reaction time

The band gap of the $NiFe_2O_4$ was estimated by extrapolating the linear region of the Tauc-plot whereat the absorbance multiplied by the energy squared is plotted against the energy as seen in figure 64. The estimated band gap values are shown in table 34 Hussain et al. reported a band gap of 2.1 eV for Fe_2O_3 and 1.77 eV for $NiFe_2O_4$.[172] The evaluation of the band gap via the Tauc-plot for the samples with the number 55, 56, 58, 59, 60, 61 and 62 resulted in a value which is close to 2 eV and it is assumed, that for these samples the synthesis of $NiFe_2O_4$ was not successful. The samples with the number 57, 64, 65 and 66 possess an evaluated band gap value in the range of 1.75-1.79. However, in the absorption curve of sample 57, shown in figure 63, the peak at approximately 750 nm, which is characteristic for the absorption behaviour of $NiFe_2O_4$ is not visible. It is assumed, that the synthesis of sample 64, 65 and 66 resulted in $NiFe_2O_4$.

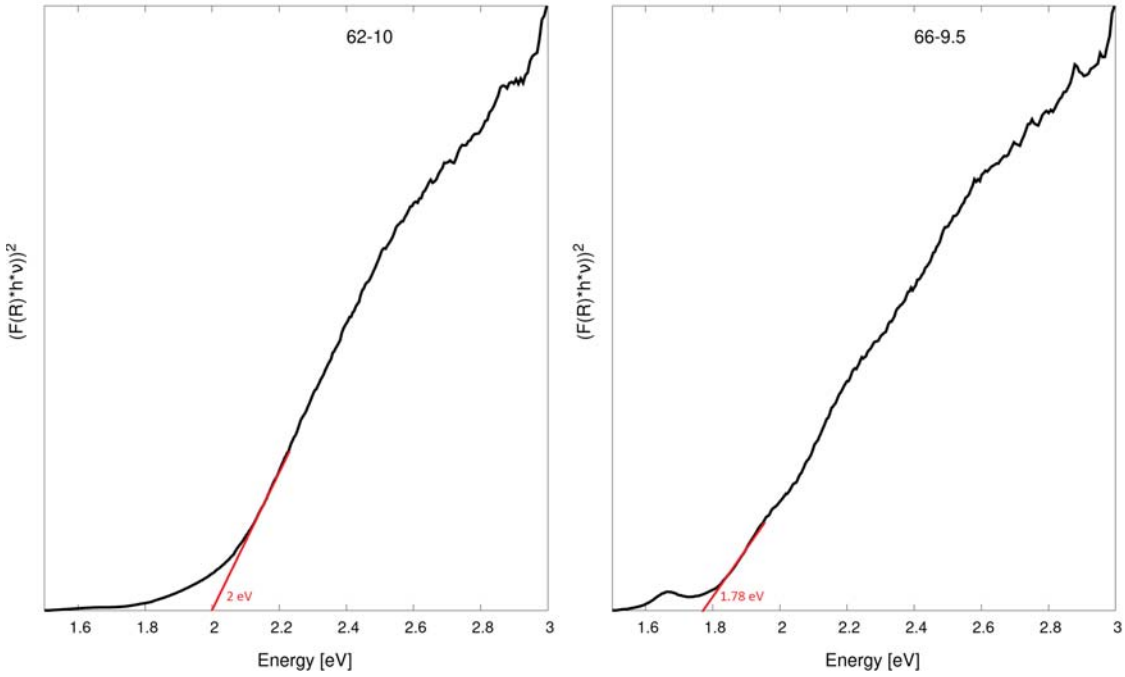

Figure 64: Tauc plot of $NiFe_20_4$ with the following notation: sample number-pH

Table 34: Estimated band gaps of $NiFe_2O_4$

Sample number	55	56	57	58	59	60	61	62	63	64	65	66
band gap [eV]	1.98	1.88	1.79	1.87	1.82	1.9	1.98	2	1.99	1.75	1.75	1.78

B.5 Fourier transformed infrared spectroscopy

B.5.1 pH dependent synthesis

For further characterisation, FT-IR spectra of the $NiFe_2O_4$ samples were measured and are shown in figure 65. The IR bands of solids are usually assigned to the vibration of ions in the crystal lattice.[173] The FT-IR spectrum has two absorption bands at approximately 400–600 cm^{-1}, which correspond to the octahedral and tetrahedral sites of positive ions of $NiFe_2O_4$, respectively.[174] The different values of absorption position for octahedral and tetrahedral complexes of $NiFe_2O_4$ crystals are due to the different values of Fe^{3+}–O^{2-} distance for octahedral and tetrahedral sites. In previous reports it was evaluated, that the higher absorption band at approximately 600 cm^{-1} corresponds to the intrinsic vibrations of tetrahedral complexes and the lower absorption band at approximately 400 cm^{-1} is attributed to the vibrations of octahedral complexes.[175,176] The peak around 1383 cm^{-1} is due to the stretching vibrations of the anti-symmetric NO^{3-} group.[177] The FT-IR spectra of the samples show a peak at 600 cm^{-1} with additionally two shoulders for sample 18, 22, 26, 27 and 28. The same peak with one shoulder is visible for sample 20, 21, 23, 24 and 25, and were assumed as $NiFe_2O_4$ according to theis DRS results, shown in figure 61. It can be assumed that the peak at 600 cm^{-1} of the FT-IR spectra with only one additional shoulder could be assigned to $NiFe_2O_4$.

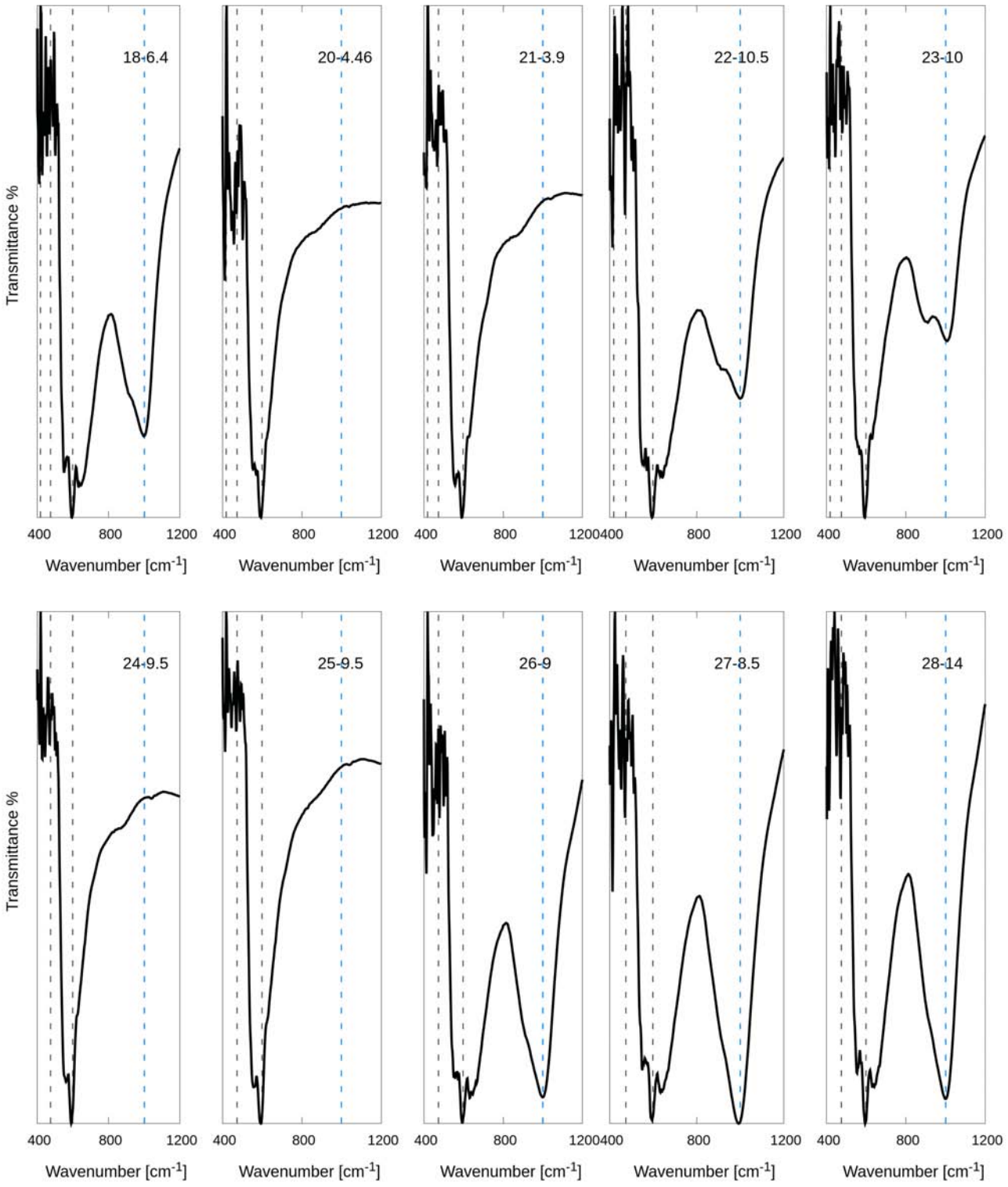

Figure 65: FT-IR spectra of $NiFe_2O_4$ with the following notation: sample number-pH, reference band positions taken from Srivastava et al.[176] and Sivakumar et al.[177]

B.5.2 Time dependent synthesis

For further characterisation, FT-IR spectra of the $NiFe_2O_4$ samples were measured and are shown in figure 66. The IR bands of solids are usually assigned to the vibration of ions in the crystal lattice.[173] The FT-IR spectrum has two absorption bands at approximately 400–600 cm^{-1}, which correspond to the octahedral and tetrahedral sites of positive ions of $NiFe_2O_4$, respectively.[174] The different values of absorption position for octahedral and tetrahedral complexes of $NiFe_2O_4$ crystals are due to the different values of Fe^{3+}–O^{2-} distance for octahedral and tetrahedral sites. In previous reports it was evaluated, that the higher absorption band at approximately 600 cm^{-1} corresponds to the intrinsic vibrations of tetrahedral complexes and the lower absorption band at approximately 400 cm^{-1} is attributed to the vibrations of octahedral complexes.[175,176] The peak around 1383 cm^{-1} is due to the stretching vibrations of the anti-symmetric NO^{3-} group.[177] On the FT-IR spectrum of the samples 64, 65 and 66 show a peak at 600 cm^{-1} with one shoulder compared to all the other samples, which have a peak at the same position with two additional shoulders. The samples 64 65 and 66 show a step like absoprtion spectrum in figure 63, which is an indicator for the successful synthesis of $NiFe_2O_4$, and its in correlation with the one shouldered peak at 600 $^{-1}$ presented in figure 66.

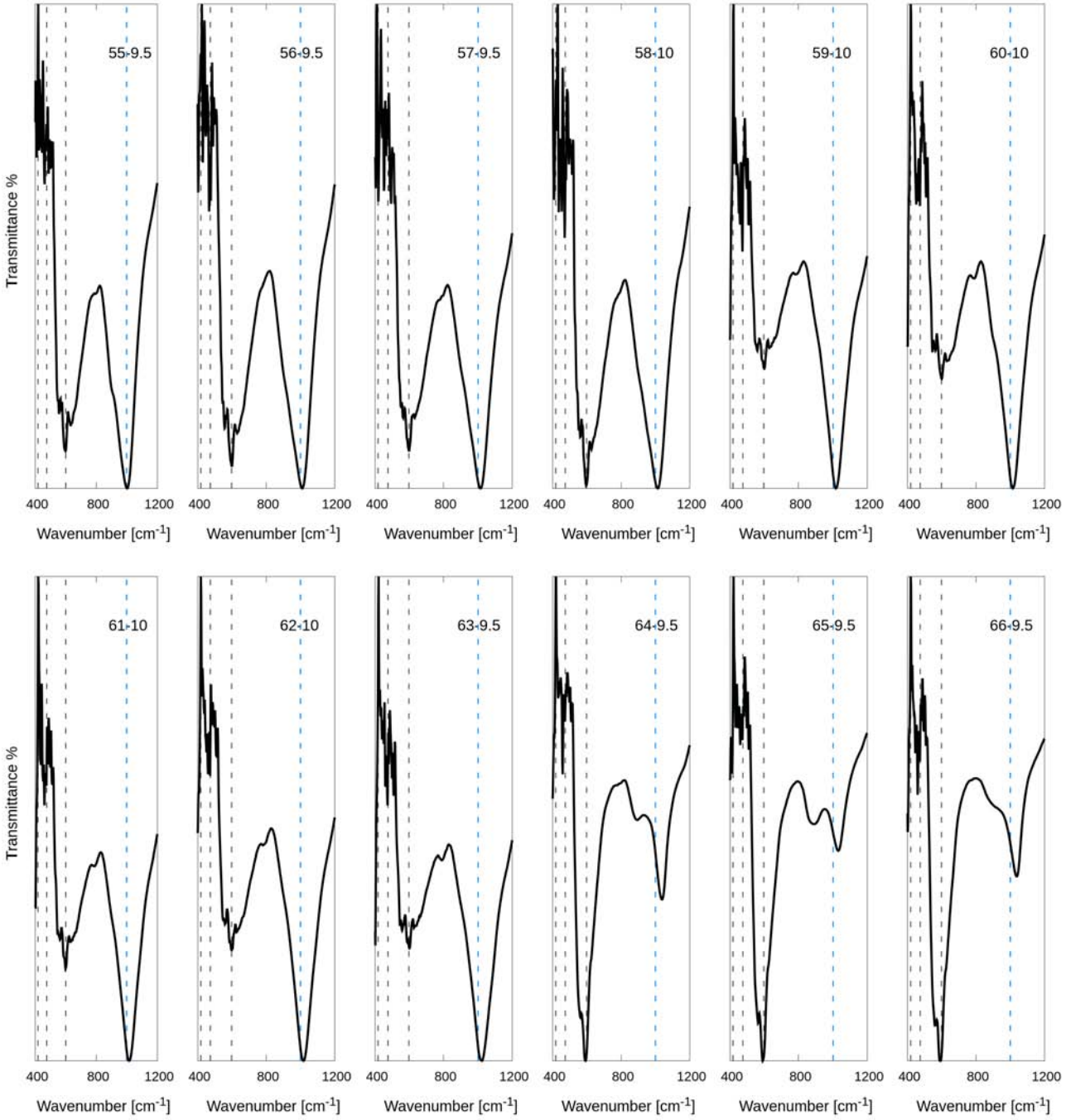

Figure 66: FT-IR spectra of $NiFe_2O_4$ with the following notation: sample number-pH, reference band positions taken from Srivastava et al.[176] and Sivakumar et al.[177]

B.6 Raman spectroscopy

B.6.1 Time and temperature dependent synthesis

Nickel ferrite has inverse spinel structure, prototype symmetry O_h^7 and space group of Fd3m. Based on group theory, spinel type of ferrites has five Raman active modes[178,179]:

$$A_{1g} + E_g + 3F_{2g}$$

The Raman spectrum of $NiFe_2O_4$ sample reported by Ortiz-Quinonez et al. revealed eight dispersion bands located around 211, 335, 450, 487, 567, 596, 659, and 703 cm^{-1}, which are marked with a black dashed line in figure 67. The band at 703 cm^{-1} corresponds to the symmetric stretching of oxygen atom with respect to metal-ion in tetrahedral void of the spinel $NiFe_2O_4$ lattice. The bands at 211, 335, 487, and 596 cm^{-1} are due to the symmetric and antisymmetric bending of oxygen atom in M-O bond at octahedral voids. Finally, the bands appeared around 450, 567, and 659 cm^{-1} as the shoulders of the intense 487 and 703 Raman bands appeared due to the differences in charge and ionic radii of Ni and Fe ions, producing larger Ni^{2+}-O bonds in comparison to Fe^{3+}-O bond, and consequently changing the energy of their bending and stretching vibrations.[167,180]

Hematite belongs to the D^6_{3d} crystal space group and seven phonon lines are expected in the Raman spectrum, namely two A_{1g} modes at 225 and 498 cm^{-1} and five E_g modes 247, 293, 299, 412 and 613 cm^{-1}. However, the modes at 293 and 299 cm^{-1} were reportedly only visible during the measurements at 100 K or less.[181]

The Raman spectra of the samples 25, 62, 63, 65 and 66 are shown in figure 67. The X-ray diffractograms of these samples, shown in section B for sample 25 and section B.3.2 for 62, 63, 65 and 66. According to the X-ray powder diffractograms, these samples show poor crystallinity, therefore their Raman bands presented in figure 67 are slightly pronounced. The peaks in the Raman spectra of the sample 65 and 66 are in correlation with the reference peak positions of $NiFe_2O_4$, which are marked with a black dashed line. This finding is in correlation with the XRD and the DRS results of sample 65 and 66, which were shown in section B.3.2 and section B.4.2 It is assumed that the synthesis of $NiFe_2O_4$ was successful for sample 65 and 66. The Raman spectra of sample 25 show a similar pattern than the spectra of sample 65 and 66, but it is slightly shifted to lower Raman shift values. The X-ray powder diffractogram of sample 25, which is shown in section B revealed the same peak positions of sample 25 as of the reference diffractogram of $NiFe_2O_4$

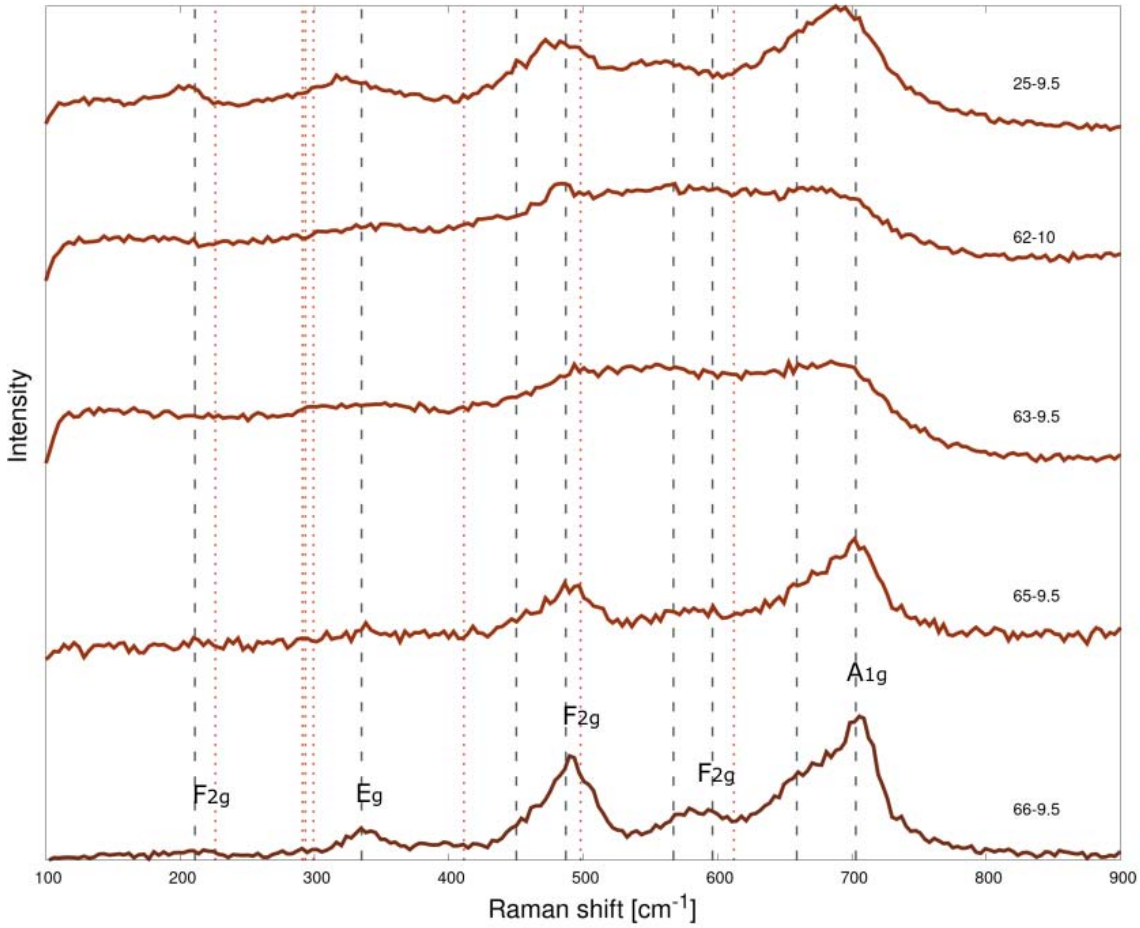

Figure 67: Raman spectra of $NiFe_2O_4$ with the following notation: sample number-pH; Black dashed line: reference of $NiFe_2O_4$ [167]; Red dotted line: reference of Fe_2O_3 [181] [182]

The peak at 1322 cm^{-1}, assigned to the hematite two-magnon scattering, is not a feature expected in a magnetite spectrum, reinforcing the assumption that hematite is present as a contaminant. [181] Figure 68 shows the Raman spectrum of 62 and 63, where a small peak at 1322 cm_{-1} is visible.

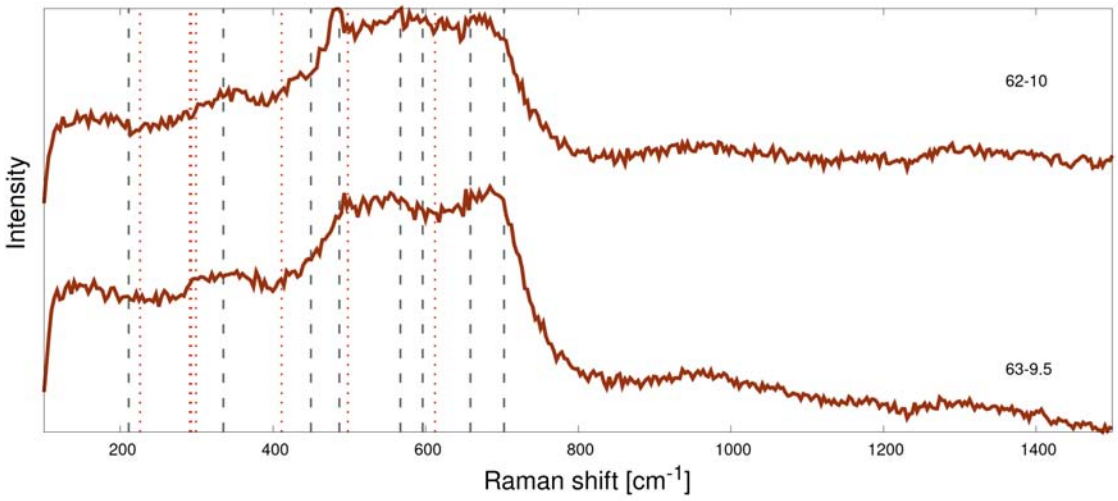

Figure 68: Raman spectra of $NiFe_2O_4$ with the following notation: sample number-pH; Black dashed line: reference of $NiFe_2O_4$ [167]; Red dotted line: reference of Fe_2O_3 [181] [182]

References

[1] E. I. A. (US), *Annual Energy Outlook 2012: With Projections to 2035*. Government Printing Office, 2012.

[2] J. Barber, "Photosynthetic energy conversion: natural and artificial," *Chemical Society Reviews*, vol. 38, no. 1, pp. 185–196, 2009.

[3] M. Grätzel, "Molecular photovoltaics that mimic photosynthesis," *Pure and Applied Chemistry*, vol. 73, no. 3, pp. 459–467, 2001.

[4] W. Wang, M. O. Tadé, and Z. Shao, "Nitrogen-doped simple and complex oxides for photocatalysis: a review," *Progress in Materials Science*, vol. 92, pp. 33–63, 2018.

[5] Z. Wang, C. Li, and K. Domen, "Recent developments in heterogeneous photocatalysts for solar-driven overall water splitting," *Chemical Society Reviews*, vol. 48, no. 7, pp. 2109–2125, 2019.

[6] N. S. Lewis, "Toward cost-effective solar energy use," *science*, vol. 315, no. 5813, pp. 798–801, 2007.

[7] K. Afroz, M. Moniruddin, N. Bakranov, S. Kudaibergenov, and N. Nuraje, "A heterojunction strategy to improve the visible light sensitive water splitting performance of photocatalytic materials," *Journal of Materials Chemistry A*, vol. 6, no. 44, pp. 21696–21718, 2018.

[8] X. Chen, S. Shen, L. Guo, and S. S. Mao, "Semiconductor-based photocatalytic hydrogen generation," *Chemical reviews*, vol. 110, no. 11, pp. 6503–6570, 2010.

[9] M. R. Gholipour, C.-T. Dinh, F. Béland, and T.-O. Do, "Nanocomposite heterojunctions as sunlight-driven photocatalysts for hydrogen production from water splitting," *Nanoscale*, vol. 7, no. 18, pp. 8187–8208, 2015.

[10] E. S. Kim, N. Nishimura, G. Magesh, J. Y. Kim, J.-W. Jang, H. Jun, J. Kubota, K. Domen, and J. S. Lee, "Fabrication of cafe2o4/taon heterojunction photoanode for photoelectrochemical water oxidation," *Journal of the american chemical society*, vol. 135, no. 14, pp. 5375–5383, 2013.

[11] S. Martha, P. C. Sahoo, and K. Parida, "An overview on visible light responsive metal oxide based photocatalysts for hydrogen energy production," *Rsc Advances*, vol. 5, no. 76, pp. 61535–61553, 2015.

[12] D. Liu, L. Li, Y. Gao, C. Wang, J. Jiang, and Y. Xiong, "The nature of photocatalytic "water splitting" on silicon nanowires," *Angewandte Chemie International Edition*, vol. 54, no. 10, pp. 2980–2985, 2015.

[13] R. Abe, "Recent progress on photocatalytic and photoelectrochemical water splitting under visible light irradiation," *Journal of Photochemistry and Photobiology C: Photochemistry Reviews*, vol. 11, no. 4, pp. 179–209, 2010.

[14] K. Maeda, "Photocatalytic water splitting using semiconductor particles: history and recent developments," *Journal of Photochemistry and Photobiology C: Photochemistry Reviews*, vol. 12, no. 4, pp. 237–268, 2011.

[15] X. Chen, C. Li, M. Grätzel, R. Kostecki, and S. S. Mao, "Nanomaterials for renewable energy production and storage," *Chemical Society Reviews*, vol. 41, no. 23, pp. 7909–7937, 2012.

[16] Y. Tachibana, L. Vayssieres, and J. R. Durrant, "Artificial photosynthesis for solar water-splitting," *Nature Photonics*, vol. 6, no. 8, p. 511, 2012.

[17] A. Fujishima and K. Honda, "Electrochemical photolysis of water at a semiconductor electrode," *nature*, vol. 238, no. 5358, pp. 37–38, 1972.

[18] K. Domen, J. N. Kondo, M. Hara, and T. Takata, "Photo-and mechano-catalytic overall water splitting reactions to form hydrogen and oxygen on heterogeneous catalysts," *Bulletin of the Chemical Society of Japan*, vol. 73, no. 6, pp. 1307–1331, 2000.

[19] A. Kudo and Y. Miseki, "Heterogeneous photocatalyst materials for water splitting," *Chemical Society Reviews*, vol. 38, no. 1, pp. 253–278, 2009.

[20] M. Kitano and M. Hara, "Heterogeneous photocatalytic cleavage of water," *Journal of Materials Chemistry*, vol. 20, no. 4, pp. 627–641, 2010.

[21] J. Li, H. Li, G. Zhan, and L. Zhang, "Solar water splitting and nitrogen fixation with layered bismuth oxyhalides," *Accounts of chemical research*, vol. 50, no. 1, pp. 112–121, 2017.

[22] J. Nowotny, C. Sorrell, T. Bak, and L. Sheppard, "Solar-hydrogen: Unresolved problems in solid-state science," *Solar Energy*, vol. 78, no. 5, pp. 593–602, 2005.

[23] Z. Zou, J. Ye, K. Sayama, and H. Arakawa, "Direct splitting of water under visible light irradiation with an oxide semiconductor photocatalyst," in *Materials For Sustainable Energy: A Collection of Peer-Reviewed Research and Review Articles from Nature Publishing Group*, pp. 293–295, World Scientific, 2011.

[24] P. Dong, X. Xi, and G. Hou, "Typical non-tio2-based visible-light photocatalysts," *Semiconductor Photocatalysis-Materials, Mechanisms and Applications*, 2016.

[25] S. Sun, W. Wang, D. Li, L. Zhang, and D. Jiang, "Solar light driven pure water splitting on quantum sized bivo4 without any cocatalyst," *ACS Catalysis*, vol. 4, no. 10, pp. 3498–3503, 2014.

[26] D. K. Zhong, S. Choi, and D. R. Gamelin, "Near-complete suppression of surface recombination in solar photoelectrolysis by "co-pi" catalyst-modified w: Bivo4," *Journal of the American Chemical Society*, vol. 133, no. 45, pp. 18370–18377, 2011.

[27] S. Martha, P. C. Sahoo, and K. Parida, "An overview on visible light responsive metal oxide based photocatalysts for hydrogen energy production," *Rsc Advances*, vol. 5, no. 76, pp. 61535–61553, 2015.

[28] J. S. Jang, H. G. Kim, and J. S. Lee, "Heterojunction semiconductors: a strategy to develop efficient photocatalytic materials for visible light water splitting," *Catalysis today*, vol. 185, no. 1, pp. 270–277, 2012.

[29] R. Marschall, "Semiconductor composites: strategies for enhancing charge carrier separation to improve photocatalytic activity," *Advanced Functional Materials*, vol. 24, no. 17, pp. 2421–2440, 2014.

[30] G. A. Somorjai, F. Tao, and J. Y. Park, "The nanoscience revolution: merging of colloid science, catalysis and nanoelectronics," *Topics in Catalysis*, vol. 47, no. 1-2, pp. 1–14, 2008.

[31] B. Ren, Y. Huang, C. Han, M. N. Nadagouda, and D. D. Dionysiou, "Ferrites as photocatalysts for water splitting and degradation of contaminants," in *Ferrites and Ferrates: Chemistry and Applications in Sustainable Energy and Environmental Remediation*, pp. 79–112, ACS Publications, 2016.

[32] B. A. Pinaud, J. D. Benck, L. C. Seitz, A. J. Forman, Z. Chen, T. G. Deutsch, B. D. James, K. N. Baum, G. N. Baum, S. Ardo, *et al.*, "Technical and economic feasibility of centralized facilities for solar hydrogen production via photocatalysis and photoelectrochemistry," *Energy & Environmental Science*, vol. 6, no. 7, pp. 1983–2002, 2013.

[33] D. M. Fabian, S. Hu, N. Singh, F. A. Houle, T. Hisatomi, K. Domen, F. E. Osterloh, and S. Ardo, "Particle suspension reactors and materials for solar-driven water splitting," *Energy & Environmental Science*, vol. 8, no. 10, pp. 2825–2850, 2015.

[34] Y. Goto, T. Hisatomi, Q. Wang, T. Higashi, K. Ishikiriyama, T. Maeda, Y. Sakata, S. Okunaka, H. Tokudome, M. Katayama, *et al.*, "A particulate photocatalyst water-splitting panel for large-scale solar hydrogen generation," *Joule*, vol. 2, no. 3, pp. 509–520, 2018.

[35] C. X. Kronawitter, L. Vayssieres, S. Shen, L. Guo, D. A. Wheeler, J. Z. Zhang, B. R. Antoun, and S. S. Mao, "A perspective on solar-driven water splitting with all-oxide hetero-nanostructures," *Energy & Environmental Science*, vol. 4, no. 10, pp. 3889–3899, 2011.

[36] E. Casbeer, V. K. Sharma, and X.-Z. Li, "Synthesis and photocatalytic activity of ferrites under visible light: a review," *Separation and Purification Technology*, vol. 87, pp. 1–14, 2012.

[37] N. Serpone, G. Sauvé, R. Koch, H. Tahiri, P. Pichat, P. Piccinini, E. Pelizzetti, and H. Hidaka, "Standardization protocol of process efficiencies and activation parameters in heterogeneous photocatalysis: relative photonic efficiencies ζr," *Journal of photochemistry and photobiology A: Chemistry*, vol. 94, no. 2-3, pp. 191–203, 1996.

[38] X. Zong, G. Wu, H. Yan, G. Ma, J. Shi, F. Wen, L. Wang, and C. Li, "Photocatalytic h2 evolution on mos2/cds catalysts under visible light irradiation," *The Journal of Physical Chemistry C*, vol. 114, no. 4, pp. 1963–1968, 2010.

[39] S. Khan and S. Majumder, "Optimization of p-silicon surface by etching and electrodeposition of pt and ni for photosplitting of water," *International journal of hydrogen energy*, vol. 14, no. 9, pp. 653–660, 1989.

[40] J. Akikusa and S. U. Khan, "Photoelectrolysis of water to hydrogen in p-sic/pt and p-sic/n-tio2 cells," *International journal of hydrogen energy*, vol. 27, no. 9, pp. 863–870, 2002.

[41] J. S. Jang, S. H. Choi, H. G. Kim, and J. S. Lee, "Location and state of pt in platinized cds/tio2 photocatalysts for hydrogen production from water under visible light," *The Journal of Physical Chemistry C*, vol. 112, no. 44, pp. 17200–17205, 2008.

[42] K. Maeda, K. Teramura, D. Lu, N. Saito, Y. Inoue, and K. Domen, "Noble-metal/cr2o3 core/shell nanoparticles as a cocatalyst for photocatalytic overall water splitting," *Angewandte Chemie International Edition*, vol. 45, no. 46, pp. 7806–7809, 2006.

[43] K. Domen, S. Naito, T. Onishi, and K. Tamaru, "Photocatalytic decomposition of liquid water on a nio2 srtio3 catalyst," *Chemical Physics Letters*, vol. 92, no. 4, pp. 433–434, 1982.

[44] A. Iwase, H. Kato, and A. Kudo, "Nanosized au particles as an efficient cocatalyst for photocatalytic overall water splitting," *Catalysis letters*, vol. 108, no. 1-2, pp. 7–10, 2006.

[45] J. Lehn, J. Sauvage, R. Zlessel, and L. Hilaire, "Water photolysis by uv irradiation of rhodium loaded strontium titanate catalysts. relation between catalytic activity and nature of the deposit from combined photolysis and esca studies," *Israel Journal of Chemistry*, vol. 22, no. 2, pp. 168–172, 1982.

[46] K. Maeda, K. Teramura, and K. Domen, "Effect of post-calcination on photocatalytic activity of (ga1- xznx)(n1- xox) solid solution for overall water splitting under visible light," *Journal of catalysis*, vol. 254, no. 2, pp. 198–204, 2008.

[47] A. J. Esswein and D. G. Nocera, "Hydrogen production by molecular photocatalysis," *Chemical reviews*, vol. 107, no. 10, pp. 4022–4047, 2007.

[48] A. Galińska and J. Walendziewski, "Photocatalytic water splitting over pt- tio2 in the presence of sacrificial reagents," *Energy & Fuels*, vol. 19, no. 3, pp. 1143–1147, 2005.

[49] J. Wang, P. Yang, B. Cao, J. Zhao, and Z. Zhu, "Photocatalytic carbon–carbon bond formation with concurrent hydrogen evolution on the pt/tio2 nanotube," *Applied Surface Science*, vol. 325, pp. 86–90, 2015.

[50] T. Kawai and T. Sakata, "Production of h 2 and co from liquid water and carbon using solar energy," *Journal of the Chemical Society, Chemical Communications*, no. 23, pp. 1047–1048, 1979.

[51] T. Kawai and T. Sakata, "Photocatalytic hydrogen production from liquid methanol and water," *Journal of the Chemical Society, Chemical Communications*, no. 15, pp. 694–695, 1980.

[52] H. Tong, S. Ouyang, Y. Bi, N. Umezawa, M. Oshikiri, and J. Ye, "Nano-photocatalytic materials: possibilities and challenges," *Advanced materials*, vol. 24, no. 2, pp. 229–251, 2012.

[53] T. Umebayashi, T. Yamaki, H. Itoh, and K. Asai, "Analysis of electronic structures of 3d transition metal-doped tio2 based on band calculations," *Journal of Physics and Chemistry of Solids*, vol. 63, no. 10, pp. 1909–1920, 2002.

[54] T. Nishikawa, Y. Shinohara, T. Nakajima, M. Fujita, and S. Mishima, "Prospect of activating a photocatalyst by sunlight-a quantum chemical study of isomorphically substituted titania," *Chemistry letters*, vol. 28, no. 11, pp. 1133–1134, 1999.

[55] S. Ouyang, H. Zhang, D. Li, T. Yu, J. Ye, and Z. Zou, "Electronic structure and photocatalytic characterization of a novel photocatalyst agalo2," *The Journal of Physical Chemistry B*, vol. 110, no. 24, pp. 11677–11682, 2006.

[56] H. Kato, H. Kobayashi, and A. Kudo, "Role of ag+ in the band structures and photocatalytic properties of agmo3 (m: Ta and nb) with the perovskite structure," *The Journal of Physical Chemistry B*, vol. 106, no. 48, pp. 12441–12447, 2002.

[57] T. Kako and J. Ye, "Comparison of photocatalytic activities of two kinds of lead magnesium niobate for decomposition of organic compounds under visible-light irradiation," *Journal of Materials Research*, vol. 22, no. 9, pp. 2590–2597, 2007.

[58] J. Tang, Z. Zou, and J. Ye, "Photocatalytic decomposition of organic contaminants by bi 2 wo 6 under visible light irradiation," *Catalysis Letters*, vol. 92, no. 1-2, pp. 53–56, 2004.

[59] A. Kudo, K. Omori, and H. Kato, "A novel aqueous process for preparation of crystal form-controlled and highly crystalline bivo4 powder from layered vanadates at room temperature and its photocatalytic and photophysical properties," *Journal of the American Chemical Society*, vol. 121, no. 49, pp. 11459–11467, 1999.

[60] H. G. Kim, D. W. Hwang, and J. S. Lee, "An undoped, single-phase oxide photocatalyst working under visible light," *Journal of the American Chemical Society*, vol. 126, no. 29, pp. 8912–8913, 2004.

[61] J. Yin, Z. Zou, and J. Ye, "A novel series of the new visible-light-driven photocatalysts mco1/3nb2/3o3 (m= ca, sr, and ba) with special electronic structures," *The Journal of Physical Chemistry B*, vol. 107, no. 21, pp. 4936–4941, 2003.

[62] J. Sato, H. Kobayashi, N. Saito, H. Nishiyama, and Y. Inoue, "Photocatalytic activities for water decomposition of ruo2-loaded aino2 (a= li, na) with d10 configuration," *Journal of Photochemistry and Photobiology A: Chemistry*, vol. 158, no. 2-3, pp. 139–144, 2003.

[63] W. Zhang, J. Tang, and J. Ye, "Structural, photocatalytic, and photophysical properties of perovskite msno 3 (m= ca, sr, and ba) photocatalysts," *Journal of materials research*, vol. 22, no. 7, pp. 1859–1871, 2007.

[64] R. Asahi, T. Morikawa, T. Ohwaki, K. Aoki, and Y. Taga, "Visible-light photocatalysis in nitrogen-doped titanium oxides," *science*, vol. 293, no. 5528, pp. 269–271, 2001.

[65] S. Sakthivel and H. Kisch, "Daylight photocatalysis by carbon-modified titanium dioxide," *Angewandte Chemie International Edition*, vol. 42, no. 40, pp. 4908–4911, 2003.

[66] W. Zhao, W. Ma, C. Chen, J. Zhao, and Z. Shuai, "Efficient degradation of toxic organic pollutants with ni2o3/tio2-x b x under visible irradiation," *Journal of the American Chemical Society*, vol. 126, no. 15, pp. 4782–4783, 2004.

[67] X. Chen and C. Burda, "The electronic origin of the visible-light absorption properties of c-, n-and s-doped tio2 nanomaterials," *Journal of the American Chemical Society*, vol. 130, no. 15, pp. 5018–5019, 2008.

[68] G. Hitoki, T. Takata, J. N. Kondo, M. Hara, H. Kobayashi, and K. Domen, "An oxynitride, taon, as an efficient water oxidation photocatalyst under visible light irradiation ($\lambda \leq$ 500 nm)," *Chemical Communications*, no. 16, pp. 1698–1699, 2002.

[69] A. Kasahara, K. Nukumizu, T. Takata, J. N. Kondo, M. Hara, H. Kobayashi, and K. Domen, "Latio2n as a visible-light ($\leq$ 600 nm)-driven photocatalyst (2)," *The Journal of Physical Chemistry B*, vol. 107, no. 3, pp. 791–797, 2003.

[70] A. Ishikawa, T. Takata, T. Matsumura, J. N. Kondo, M. Hara, H. Kobayashi, and K. Domen, "Oxysulfides ln2ti2s2o5 as stable photocatalysts for water oxidation and reduction under visible-light irradiation," *The Journal of Physical Chemistry B*, vol. 108, no. 8, pp. 2637–2642, 2004.

[71] K. Ogisu, A. Ishikawa, Y. Shimodaira, T. Takata, H. Kobayashi, and K. Domen, "Electronic band structures and photochemical properties of la- ga-based oxysulfides," *The Journal of Physical Chemistry C*, vol. 112, no. 31, pp. 11978–11984, 2008.

[72] K. Parida, K. Reddy, S. Martha, D. Das, and N. Biswal, "Fabrication of nanocrystalline lafeo3: an efficient sol–gel auto-combustion assisted visible light responsive photocatalyst for water decomposition," *International journal of hydrogen energy*, vol. 35, no. 22, pp. 12161–12168, 2010.

[73] J. Yin, Z. Zou, and J. Ye, "Photophysical and photocatalytic properties of new photocatalysts mcro4 (m= sr, ba)," *Chemical physics letters*, vol. 378, no. 1-2, pp. 24–28, 2003.

[74] J. Ye, Z. Zou, and A. Matsushita, "A novel series of water splitting photocatalysts nim2o6 (m= nb, ta) active under visible light," *International journal of hydrogen energy*, vol. 28, no. 6, pp. 651–655, 2003.

[75] J. Ye, Z. Zou, M. Oshikiri, A. Matsushita, M. Shimoda, M. Imai, and T. Shishido, "A novel hydrogen-evolving photocatalyst invo4 active under visible light irradiation," *Chemical Physics Letters*, vol. 356, no. 3-4, pp. 221–226, 2002.

[76] G. Carraro, C. Maccato, A. Gasparotto, T. Montini, S. Turner, O. I. Lebedev, V. Gombac, G. Adami, G. Van Tendeloo, D. Barreca, *et al.*, "Enhanced hydrogen production by photoreforming of renewable oxygenates through nanostructured fe2o3 polymorphs," *Advanced Functional Materials*, vol. 24, no. 3, pp. 372–378, 2014.

[77] S. Chen, T. Takata, and K. Domen, "Particulate photocatalysts for overall water splitting," *Nature Reviews Materials*, vol. 2, no. 10, pp. 1–17, 2017.

[78] S. J. Moniz, S. A. Shevlin, D. J. Martin, Z.-X. Guo, and J. Tang, "Visible-light driven heterojunction photocatalysts for water splitting–a critical review," *Energy & Environmental Science*, vol. 8, no. 3, pp. 731–759, 2015.

[79] Y.-P. Yuan, L.-W. Ruan, J. Barber, S. C. J. Loo, and C. Xue, "Hetero-nanostructured suspended photocatalysts for solar-to-fuel conversion," *Energy & Environmental Science*, vol. 7, no. 12, pp. 3934–3951, 2014.

[80] A. B. Djurišić, Y. He, and A. M. Ng, "Visible-light photocatalysts: Prospects and challenges," *APL Materials*, vol. 8, no. 3, p. 030903, 2020.

[81] A. Behera, D. Kandi, S. Martha, and K. Parida, "Constructive interfacial charge carrier separation of a p-cafe2o4@ n-znfe2o4 heterojunction architect photocatalyst toward photodegradation of antibiotics," *Inorganic chemistry*, vol. 58, no. 24, pp. 16592–16608, 2019.

[82] M. T. Uddin, Y. Nicolas, C. Olivier, W. Jaegermann, N. Rockstroh, H. Junge, and T. Toupance, "Band alignment investigations of heterostructure nio/tio 2 nanomaterials used as efficient heterojunction earth-abundant metal oxide photocatalysts for hydrogen production," *Physical Chemistry Chemical Physics*, vol. 19, no. 29, pp. 19279–19288, 2017.

[83] J. Low, B. Cheng, and J. Yu, "Surface modification and enhanced photocatalytic co2 reduction performance of tio2: a review," *Applied Surface Science*, vol. 392, pp. 658–686, 2017.

[84] P. Zhou, J. Yu, and M. Jaroniec, "All-solid-state z-scheme photocatalytic systems," *Advanced Materials*, vol. 26, no. 29, pp. 4920–4935, 2014.

[85] K. Maeda, "Z-scheme water splitting using two different semiconductor photocatalysts," *Acs Catalysis*, vol. 3, no. 7, pp. 1486–1503, 2013.

[86] K. Sayama, K. Mukasa, R. Abe, Y. Abe, and H. Arakawa, "A new photocatalytic water splitting system under visible light irradiation mimicking a z-scheme mechanism in photosynthesis," *Journal of Photochemistry and Photobiology A: Chemistry*, vol. 148, no. 1-3, pp. 71–77, 2002.

[87] D. Ke, T. Peng, L. Ma, P. Cai, and P. Jiang, "Photocatalytic water splitting for o2 production under visible-light irradiation on bivo4 nanoparticles in different sacrificial reagent solutions," *Applied Catalysis A: General*, vol. 350, no. 1, pp. 111–117, 2008.

[88] Y. Lin, C. Lu, and C. Wei, "Microstructure and photocatalytic performance of bivo4 prepared by hydrothermal method," *Journal of Alloys and Compounds*, vol. 781, pp. 56–63, 2019.

[89] T. Das, X. Rocquefelte, R. Laskowski, L. Lajaunie, S. Jobic, P. Blaha, and K. Schwarz, "Investigation of the optical and excitonic properties of the visible light-driven photocatalytic bivo4 material," *Chemistry of Materials*, vol. 29, no. 8, pp. 3380–3386, 2017.

[90] G. Tan, L. Zhang, H. Ren, J. Huang, W. Yang, and A. Xia, "Microwave hydrothermal synthesis of n-doped bivo4 nanoplates with exposed (040) facets and enhanced visible-light photocatalytic properties," *Ceramics International*, vol. 40, no. 7, pp. 9541–9547, 2014.

[91] M. Xu, J. Yang, C. Sun, L. Liu, Y. Cui, and B. Liang, "Performance enhancement strategies of bi-based photocatalysts: A review on recent progress," *Chemical Engineering Journal*, p. 124402, 2020.

[92] C. M. Suarez, S. Hernández, and N. Russo, "Bivo4 as photocatalyst for solar fuels production through water splitting: a short review," *Applied Catalysis A: General*, vol. 504, pp. 158–170, 2015.

[93] M. Smirnov, A. Mirgorodsky, V. Y. Kazimirov, and R. Guinebretière, "Bond-switching mechanism for the zircon-scheelite phase transition," *Physical Review B*, vol. 78, no. 9, p. 094109, 2008.

[94] S. Tokunaga, H. Kato, and A. Kudo, "Selective preparation of monoclinic and tetragonal bivo4 with scheelite structure and their photocatalytic properties," *Chemistry of Materials*, vol. 13, no. 12, pp. 4624–4628, 2001.

[95] Z. Zhao, Z. Li, and Z. Zou, "Electronic structure and optical properties of monoclinic clinobisvanite bivo 4," *Physical Chemistry Chemical Physics*, vol. 13, no. 10, pp. 4746–4753, 2011.

[96] H. Nishiyama, H. Kobayashi, and Y. Inoue, "Effects of distortion of metal–oxygen octahedra on photocatalytic water-splitting performance of ruo2-loaded niobium and tantalum phosphate bronzes," *ChemSusChem*, vol. 4, no. 2, pp. 208–215, 2011.

[97] J. Yang, D. Wang, X. Zhou, and C. Li, "A theoretical study on the mechanism of photocatalytic oxygen evolution on bivo4 in aqueous solution," *Chemistry–A European Journal*, vol. 19, no. 4, pp. 1320–1326, 2013.

[98] D. Payne, R. Egdell, A. Walsh, G. Watson, J. Guo, P.-A. Glans, T. Learmonth, and K. Smith, "Electronic origins of structural distortions in post-transition metal oxides: experimental and theoretical evidence for a revision of the lone pair model," *Physical review letters*, vol. 96, no. 15, p. 157403, 2006.

[99] J. K. Cooper, S. Gul, F. M. Toma, L. Chen, P.-A. Glans, J. Guo, J. W. Ager, J. Yano, and I. D. Sharp, "Electronic structure of monoclinic bivo4," *Chemistry of Materials*, vol. 26, no. 18, pp. 5365–5373, 2014.

[100] A. Walsh, Y. Yan, M. N. Huda, M. M. Al-Jassim, and S.-H. Wei, "Band edge electronic structure of bivo4: elucidating the role of the bi s and v d orbitals," *Chemistry of Materials*, vol. 21, no. 3, pp. 547–551, 2009.

[101] A. J. Rettie, H. C. Lee, L. G. Marshall, J.-F. Lin, C. Capan, J. Lindemuth, J. S. McCloy, J. Zhou, A. J. Bard, and C. B. Mullins, "Combined charge carrier transport and photoelectrochemical characterization of bivo4 single crystals: intrinsic behavior of a complex metal oxide," *Journal of the American Chemical Society*, vol. 135, no. 30, pp. 11389–11396, 2013.

[102] J. Hu, X. Zhao, W. Chen, H. Su, and Z. Chen, "Theoretical insight into the mechanism of photoelectrochemical oxygen evolution reaction on bivo4 anode with oxygen vacancy," *The Journal of Physical Chemistry C*, vol. 121, no. 34, pp. 18702–18709, 2017.

[103] D. Wang, H. Jiang, X. Zong, Q. Xu, Y. Ma, G. Li, and C. Li, "Crystal facet dependence of water oxidation on bivo4 sheets under visible light irradiation," *Chemistry–A European Journal*, vol. 17, no. 4, pp. 1275–1282, 2011.

[104] A. Bhattacharya, K. Mallick, and A. Hartridge, "Phase transition in bivo4," *Materials Letters*, vol. 30, no. 1, pp. 7–13, 1997.

[105] S. M. Thalluri, C. Martinez Suarez, M. Hussain, S. Hernandez, A. Virga, G. Saracco, and N. Russo, "Evaluation of the parameters affecting the visible-light-induced photocatalytic activity of monoclinic bivo4 for water oxidation," *Industrial & Engineering Chemistry Research*, vol. 52, no. 49, pp. 17414–17418, 2013.

[106] B. Zhou, J. Qu, X. Zhao, and H. Liu, "Fabrication and photoelectrocatalytic properties of nanocrystalline monoclinic bivo4 thin-film electrode," *Journal of Environmental Sciences*, vol. 23, no. 1, pp. 151–159, 2011.

[107] A. Kudo, K. Ueda, H. Kato, and I. Mikami, "Photocatalytic o 2 evolution under visible light irradiation on bivo 4 in aqueous agno 3 solution," *Catalysis Letters*, vol. 53, no. 3-4, pp. 229–230, 1998.

[108] G. Xi and J. Ye, "Synthesis of bismuth vanadate nanoplates with exposed {001} facets and enhanced visible-light photocatalytic properties," *Chemical Communications*, vol. 46, no. 11, pp. 1893–1895, 2010.

[109] A. Zhang, J. Zhang, N. Cui, X. Tie, Y. An, and L. Li, "Effects of ph on hydrothermal synthesis and characterization of visible-light-driven bivo4 photocatalyst," *Journal of Molecular Catalysis A: Chemical*, vol. 304, no. 1-2, pp. 28–32, 2009.

[110] R. Li, F. Zhang, D. Wang, J. Yang, M. Li, J. Zhu, X. Zhou, H. Han, and C. Li, "Spatial separation of photogenerated electrons and holes among {010} and {110} crystal facets of bivo 4," *Nature communications*, vol. 4, no. 1, pp. 1–7, 2013.

[111] S. Praneetha and A. V. Murugan, "Development of sustainable rapid microwave assisted process for extracting nanoporous si from earth abundant agricultural residues and their carbon-based nanohybrids for lithium energy storage," *ACS Sustainable Chemistry & Engineering*, vol. 3, no. 2, pp. 224–236, 2015.

[112] S. S. Chetty, S. Praneetha, S. Basu, C. Sachidanandan, and A. V. Murugan, "Sustainable, rapid synthesis of bright-luminescent cuins 2-zns alloyed nanocrystals: Multistage nano-xenotoxicity assessment and intravital fluorescence bioimaging in zebrafish-embryos," *Scientific reports*, vol. 6, p. 26078, 2016.

[113] R. Krishnapriya, S. Praneetha, A. M. Rabel, and A. V. Murugan, "Energy efficient, one-step microwave-solvothermal synthesis of a highly electro-catalytic thiospinel nico 2 s 4/graphene nanohybrid as a novel sustainable counter electrode material for pt-free dye-sensitized solar cells," *Journal of Materials Chemistry C*, vol. 5, no. 12, pp. 3146–3155, 2017.

[114] A. V. Murugan, T. Muraliganth, and A. Manthiram, "Rapid, facile microwave-solvothermal synthesis of graphene nanosheets and their polyaniline nanocomposites for energy strorage," *Chemistry of Materials*, vol. 21, no. 21, pp. 5004–5006, 2009.

[115] S. J. Hong, S. Lee, J. S. Jang, and J. S. Lee, "Heterojunction bivo 4/wo 3 electrodes for enhanced photoactivity of water oxidation," *Energy & Environmental Science*, vol. 4, no. 5, pp. 1781–1787, 2011.

[116] W. Yao, H. Iwai, and J. Ye, "Effects of molybdenum substitution on the photocatalytic behavior of bivo 4," *Dalton Transactions*, no. 11, pp. 1426–1430, 2008.

[117] H. Fan, T. Jiang, H. Li, D. Wang, L. Wang, J. Zhai, D. He, P. Wang, and T. Xie, "Effect of bivo4 crystalline phases on the photoinduced carriers behavior and photocatalytic activity," *The Journal of Physical Chemistry C*, vol. 116, no. 3, pp. 2425–2430, 2012.

[118] G. Tan, L. Zhang, H. Ren, S. Wei, J. Huang, and A. Xia, "Effects of ph on the hierarchical structures and photocatalytic performance of bivo4 powders prepared via the microwave hydrothermal method," *ACS applied materials & interfaces*, vol. 5, no. 11, pp. 5186–5193, 2013.

[119] S. Usai, S. Obregon, A. I. Becerro, and G. Colon, "Monoclinic-tetragonal heterostructured bivo4 by yttrium doping with improved photocatalytic activity," *The Journal of Physical Chemistry C*, vol. 117, no. 46, pp. 24479–24484, 2013.

[120] M. Yan, Y. Yan, Y. Wu, W. Shi, and Y. Hua, "Microwave-assisted synthesis of monoclinic–tetragonal bivo 4 heterojunctions with enhanced visible-light-driven photocatalytic degradation of tetracycline," *RSC advances*, vol. 5, no. 110, pp. 90255–90264, 2015.

[121] H. M. Zhang, J. B. Liu, H. Wang, W. X. Zhang, and H. Yan, "Rapid microwave-assisted synthesis of phase controlled bivo 4 nanocrystals and research on photocatalytic properties under visible light irradiation," *Journal of Nanoparticle Research*, vol. 10, no. 5, pp. 767–774, 2008.

[122] T. S. Dabodiya, P. Selvarasu, and A. V. Murugan, "Tetragonal to monoclinic crystalline phases change of bivo4 via microwave-hydrothermal reaction: in correlation with visible-light-driven photocatalytic performance," *Inorganic chemistry*, vol. 58, no. 8, pp. 5096–5110, 2019.

[123] K. Pingmuang, A. Nattestad, W. Kangwansupamonkon, G. G. Wallace, S. Phanichphant, and J. Chen, "Phase-controlled microwave synthesis of pure monoclinic bivo4 nanoparticles for photocatalytic dye degradation," *Applied Materials Today*, vol. 1, no. 2, pp. 67–73, 2015.

[124] W. Shi, Y. Yan, and X. Yan, "Microwave-assisted synthesis of nano-scale bivo4 photocatalysts and their excellent visible-light-driven photocatalytic activity for the degradation of ciprofloxacin," *Chemical Engineering Journal*, vol. 215, pp. 740–746, 2013.

[125] Y. Zhang, G. Li, X. Yang, H. Yang, Z. Lu, and R. Chen, "Monoclinic bivo4 micro-/nanostructures: microwave and ultrasonic wave combined synthesis and their visible-light photocatalytic activities," *Journal of alloys and compounds*, vol. 551, pp. 544–550, 2013.

[126] B. S. Rodrigues, C. M. Branco, P. Corio, and J. S. Souza, "Controlling bismuth vanadate morphology and crystalline structure through optimization of microwave-assisted synthesis conditions," *Crystal Growth & Design*, vol. 20, no. 6, pp. 3673–3685, 2020.

[127] D. M. Ginosar, H. W. Rollins, L. M. Petkovic, K. C. Burch, and M. J. Rush, "High-temperature sulfuric acid decomposition over complex metal oxide catalysts," *International journal of hydrogen energy*, vol. 34, no. 9, pp. 4065–4073, 2009.

[128] T. Peng, X. Zhang, H. Lv, and L. Zan, "Preparation of nife2o4 nanoparticles and its visible-light-driven photoactivity for hydrogen production," *Catalysis Communications*, vol. 28, pp. 116–119, 2012.

[129] J. Wang, F. Ren, B. Jia, and X. Liu, "Solvothermal synthesis and characterization of nife2o4 nanospheres with adjustable sizes," *Solid State Communications*, vol. 150, no. 25-26, pp. 1141–1144, 2010.

[130] M. Shen, L. Fu, J. Tang, M. Liu, Y. Song, F. Tian, Z. Zhao, Z. Zhang, and D. D. Dionysiou, "Microwave hydrothermal-assisted preparation of novel spinel-nife2o4/natural mineral composites as microwave catalysts for degradation of aquatic organic pollutants," *Journal of hazardous materials*, vol. 350, pp. 1–9, 2018.

[131] J.-H. Lee, C.-K. Kim, S. Katoh, and R. Murakami, "Microwave-hydrothermal versus conventional hydrothermal preparation of ni-and zn-ferrite powders," *Journal of Alloys and Compounds*, vol. 325, no. 1-2, pp. 276–280, 2001.

[132] A. Baykal, N. Kasapoğlu, Y. Köseoğlu, M. S. Toprak, and H. Bayrakdar, "Ctab-assisted hydrothermal synthesis of nife2o4 and its magnetic characterization," *Journal of Alloys and Compounds*, vol. 464, no. 1-2, pp. 514–518, 2008.

[133] A. Baykal and M. Toprak, "Synthesis and characterization of nife 2 o 4 nano-octahedrons by edta-assisted hydrothermal," *Turk. J. Chem*, vol. 31, pp. 659–666, 2007.

[134] D. K. Dinkar, B. Das, R. Gopalan, and B. S. Dehiya, "Effects of surfactant on the structural and magnetic properties of hydrothermally synthesized nife2o4 nanoparticles," *Materials Chemistry and Physics*, vol. 218, pp. 70–76, 2018.

[135] C. Xiangfeng, J. Dongli, and Z. Chenmou, "The preparation and gas-sensing properties of nife2o4 nanocubes and nanorods," *Sensors and Actuators B: Chemical*, vol. 123, no. 2, pp. 793–797, 2007.

[136] T. Saison, N. Chemin, C. Chaneac, O. Durupthy, L. Mariey, F. Mauge, V. Brezova, and J.-P. Jolivet, "New insights into bivo4 properties as visible light photocatalyst," *The Journal of Physical Chemistry C*, vol. 119, no. 23, pp. 12967–12977, 2015.

[137] L. S. Kumari, P. P. Rao, A. N. P. Radhakrishnan, V. James, S. Sameera, and P. Koshy, "Brilliant yellow color and enhanced nir reflectance of monoclinic bivo4 through distortion in vo43-tetrahedra," *Solar energy materials and solar cells*, vol. 112, pp. 134–143, 2013.

[138] P. Millán, J. Rojo, L. Pardo, J. Ricote, and A. Castro, "Thermal and electrical behavior of γ-bi2vo5. 5 and f-bi2vo5 oxides obtained from mechanochemically activated precursors," *Materials research bulletin*, vol. 36, no. 7-8, pp. 1277–1286, 2001.

[139] Y. Zhang, T. Yamamoto, M. A. Green, H. Kageyama, and Y. Ueda, "Interlayer communication in aurivillius vanadate to enable defect structures and charge ordering," *Inorganic chemistry*, vol. 54, no. 22, pp. 10925–10933, 2015.

[140] S. Sun, W. Wang, L. Zhou, and H. Xu, "Efficient methylene blue removal over hydrothermally synthesized starlike bivo4," *Industrial & engineering chemistry research*, vol. 48, no. 4, pp. 1735–1739, 2009.

[141] H. Jiang, X. Meng, H. Dai, J. Deng, Y. Liu, L. Zhang, Z. Zhao, and R. Zhang, "High-performance porous spherical or octapod-like single-crystalline bivo4 photocatalysts for the removal of phenol and methylene blue under visible-light illumination," *Journal of hazardous materials*, vol. 217, pp. 92–99, 2012.

[142] D. Ke, T. Peng, L. Ma, P. Cai, and K. Dai, "Effects of hydrothermal temperature on the microstructures of bivo4 and its photocatalytic o2 evolution activity under visible light," *Inorganic Chemistry*, vol. 48, no. 11, pp. 4685–4691, 2009.

[143] M. Oshikiri, M. Boero, J. Ye, Z. Zou, and G. Kido, "Electronic structures of promising photocatalysts inmo 4 (m= v, nb, ta) and bivo 4 for water decomposition in the visible wavelength region," *The Journal of chemical physics*, vol. 117, no. 15, pp. 7313–7318, 2002.

[144] P. Schaufelberger, H. Merx, and M. Contre, "Structure cristalline du bismuth v," *High Temp. Pressure*, vol. 5, pp. 221–230, 1973.

[145] S. B. Hendricks, E. Posnjak, and F. Kracek, "Molecular rotation in the solid state. the variation of the crystal structure of ammonium nitrate with temperature," *Journal of the American Chemical Society*, vol. 54, no. 7, pp. 2766–2786, 1932.

[146] S. Radaev and V. Simonov, "Structures of sillenites and atomic mechanisms of their isomorphic substitutions," *Soviet physics. Crystallography*, vol. 37, no. 4, pp. 484–499, 1992.

[147] A. Tayyebi, T. Soltani, H. Hong, and B.-K. Lee, "Improved photocatalytic and photoelectrochemical performance of monoclinic bismuth vanadate by surface defect states (bi1-xvo4)," *Journal of colloid and interface science*, vol. 514, pp. 565–575, 2018.

[148] Y. Sun, Y. Xie, C. Wu, and R. Long, "First experimental identification of bivo4· 0.4 h2o and its evolution mechanism to final monoclinic bivo4," *Crystal growth & design*, vol. 10, no. 2, pp. 602–607, 2010.

[149] G. Zhao, W. Liu, M. Dong, W. Li, and L. Chang, "Synthesis of monoclinic sheet-like bivo4 with preferentially exposed (040) facets as a new yellow-green pigment," *Dyes and Pigments*, vol. 134, pp. 91–98, 2016.

[150] J. Liu, H. Wang, S. Wang, and H. Yan, "Hydrothermal preparation of bivo4 powders," *Materials Science and Engineering: B*, vol. 104, no. 1-2, pp. 36–39, 2003.

[151] M. Gotić, S. Musić, M. Ivanda, M. Šoufek, and S. Popović, "Synthesis and characterisation of bismuth (iii) vanadate," *Journal of Molecular Structure*, vol. 744, pp. 535–540, 2005.

[152] X. Lin, L. Yu, L. Yan, H. Li, Y. Yan, C. Liu, and H. Zhai, "Visible light photocatalytic activity of bivo4 particles with different morphologies," *Solid state sciences*, vol. 32, pp. 61–66, 2014.

[153] K. Shetty, L. Renuka, H. Nagaswarupa, H. Nagabhushana, K. Anantharaju, D. Rangappa, S. Prashantha, and K. Ashwini, "A comparative study on cufe2o4, znfe2o4 and nife2o4: Morphology, impedance and photocatalytic studies," *Materials Today: Proceedings*, vol. 4, no. 11, pp. 11806–11815, 2017.

[154] A. Goldman, *Modern ferrite technology*. Springer Science & Business Media, 2006.

[155] H. Perron, T. Mellier, C. Domain, J. Roques, E. Simoni, R. Drot, and H. Catalette, "Structural investigation and electronic properties of the nickel ferrite nife2o4: a periodic density functional theory approach," *Journal of Physics: Condensed Matter*, vol. 19, no. 34, p. 346219, 2007.

[156] K. Bouferrache, Z. Charifi, H. Baaziz, A. Alsaad, and A. Telfah, "Electronic structure, magnetic and optic properties of spinel compound nife2o4," *Semiconductor Science and Technology*, 2020.

[157] A. Bhosale and B. Chougule, "X-ray, infrared and magnetic studies of al-substituted ni ferrites," *Materials Chemistry and Physics*, vol. 97, no. 2-3, pp. 273–276, 2006.

[158] G. K. H. Madsen and P. Novák, "Charge order in magnetite. an lda+ u study," *EPL (Europhysics Letters)*, vol. 69, no. 5, p. 777, 2005.

[159] V. Anisimov and O. Gunnarsson, "Density-functional calculation of effective coulomb interactions in metals," *Physical Review B*, vol. 43, no. 10, p. 7570, 1991.

[160] X. Shi, Y.-F. Li, S. L. Bernasek, and A. Selloni, "Structure of the nife2o4 (001) surface in contact with gaseous o2 and water vapor," *Surface Science*, vol. 640, pp. 73–79, 2015.

[161] P. V. Kumar, M. P. Short, S. Yip, B. Yildiz, and J. C. Grossman, "High surface reactivity and water adsorption on nife2o4 (111) surfaces," *The Journal of Physical Chemistry C*, vol. 117, no. 11, pp. 5678–5683, 2013.

[162] D. H. Taffa, R. Dillert, A. C. Ulpe, K. C. Bauerfeind, T. Bredow, D. W. Bahnemann, and M. Wark, "Photoelectrochemical and theoretical investigations of spinel type ferrites (m x fe 3- x o 4) for water splitting: a mini-review," *Journal of Photonics for Energy*, vol. 7, no. 1, p. 012009, 2016.

[163] C. J. O'Brien, Z. Rak, and D. W. Brenner, "Calculated stability and structure of nickel ferrite crystal surfaces in hydrothermal environments," *The Journal of Physical Chemistry C*, vol. 118, no. 10, pp. 5414–5423, 2014.

[164] S. Mitra, S. Das, S. Basu, P. Sahu, and K. Mandal, "Shape-and field-dependent morin transitions in structured α-fe2o3," *Journal of magnetism and magnetic materials*, vol. 321, no. 18, pp. 2925–2931, 2009.

[165] E. Wolska *et al.*, "The structure of hydrohematite," *Zeitschrift für Kristallographie*, vol. 154, no. 1-2, pp. 69–75, 1981.

[166] D. Hong, Y. Yamada, M. Sheehan, S. Shikano, C.-H. Kuo, M. Tian, C.-K. Tsung, and S. Fukuzumi, "Mesoporous nickel ferrites with spinel structure prepared by an aerosol spray pyrolysis method for photocatalytic hydrogen evolution," *ACS Sustainable Chemistry & Engineering*, vol. 2, no. 11, pp. 2588–2594, 2014.

[167] J.-L. Ortiz-Quinonez, U. Pal, and M. S. Villanueva, "Structural, magnetic, and catalytic evaluation of spinel co, ni, and co–ni ferrite nanoparticles fabricated by low-temperature solution combustion process," *ACS omega*, vol. 3, no. 11, pp. 14986–15001, 2018.

[168] R. J. Deeth, A. Anastasi, C. Diedrich, and K. Randell, "Molecular modelling for transition metal complexes: Dealing with d-electron effects," *Coordination Chemistry Reviews*, vol. 253, no. 5-6, pp. 795–816, 2009.

[169] A. Ceylan, S. Ozcan, C. Ni, and S. I. Shah, "Solid state reaction synthesis of nife2o4 nanoparticles," *Journal of Magnetism and Magnetic Materials*, vol. 320, no. 6, pp. 857–863, 2008.

[170] R. Dom, R. Subasri, K. Radha, and P. H. Borse, "Synthesis of solar active nanocrystalline ferrite, mfe2o4 (m: Ca, zn, mg) photocatalyst by microwave irradiation," *Solid State Communications*, vol. 151, no. 6, pp. 470–473, 2011.

[171] H. G. Kim, P. H. Borse, J. S. Jang, E. D. Jeong, O.-S. Jung, Y. J. Suh, and J. S. Lee, "Fabrication of cafe 2 o 4/mgfe 2 o 4 bulk heterojunction for enhanced visible light photocatalysis," *Chemical Communications*, no. 39, pp. 5889–5891, 2009.

[172] S. Hussain, M. M. Tavakoli, A. Waleed, U. S. Virk, S. Yang, A. Waseem, Z. Fan, and M. A. Nadeem, "Nanotextured spikes of α-fe2o3/nife2o4 composite for efficient photoelectrochemical oxidation of water," *Langmuir*, vol. 34, no. 12, pp. 3555–3564, 2018.

[173] V. Brabers, "Infrared spectra of cubic and tetragonal manganese ferrites," *physica status solidi (b)*, vol. 33, no. 2, pp. 563–572, 1969.

[174] M. Gotic, I. Czako-Nagy, S. Popovic, and S. Music, "Formation of nanocrystalline nife2o4," *Philosophical magazine letters*, vol. 78, no. 3, pp. 193–201, 1998.

[175] R. Waldron, "Infrared spectra of ferrites," *Physical review*, vol. 99, no. 6, p. 1727, 1955.

[176] M. Srivastava, A. K. Ojha, S. Chaubey, and A. Materny, "Synthesis and optical characterization of nanocrystalline nife2o4 structures," *Journal of Alloys and Compounds*, vol. 481, no. 1-2, pp. 515–519, 2009.

[177] P. Sivakumar, R. Ramesh, A. Ramanand, S. Ponnusamy, and C. Muthamizhchelvan, "Synthesis and characterization of nife2o4 nanoparticles and nanorods," *Journal of Alloys and Compounds*, vol. 563, pp. 6–11, 2013.

[178] G. Dixit, J. Singh, R. Srivastava, H. Agrawal, and R. Chaudhary, "Structural, magnetic and optical studies of nickel ferrite thin films," *Adv. Mater. Lett*, vol. 3, no. 1, pp. 21–26, 2012.

[179] P. Graves, C. Johnston, and J. Campaniello, "Raman scattering in spinel structure ferrites," *Materials Research Bulletin*, vol. 23, no. 11, pp. 1651–1660, 1988.

[180] Ç. E. Demirci, P. Manna, Y. Wroczynskyj, S. Aktürk, and J. van Lierop, "A comparison of the magnetism of cobalt-, manganese-, and nickel-ferrite nanoparticles," *Journal of Physics D: Applied Physics*, vol. 51, no. 2, p. 025003, 2017.

[181] D. De Faria, S. Venâncio Silva, and M. De Oliveira, "Raman microspectroscopy of some iron oxides and oxyhydroxides," *Journal of Raman spectroscopy*, vol. 28, no. 11, pp. 873–878, 1997.

[182] B. D. Hosterman, "Raman spectroscopic study of solid solution spinel oxides," 2011.